

NUMERICAL INVESTIGATION OF RADAR SCATTERING  
FROM ROUGH LAND SURFACES

By

JAMES MICHAEL STURM

Bachelor of Science  
Oklahoma State University  
Stillwater, Oklahoma  
1991

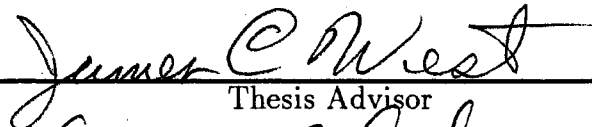
Master of Science  
Oklahoma State University  
Stillwater, Oklahoma

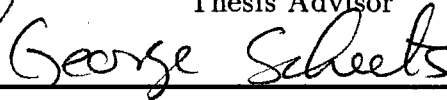
1993

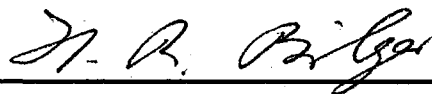
Submitted to the Faculty of the  
Graduate College of the  
Oklahoma State University  
in partial fulfillment of  
the requirements for  
the Degree of  
DOCTOR OF PHILOSOPHY  
December, 1996

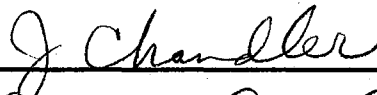
NUMERICAL INVESTIGATION OF RADAR SCATTERING  
FROM ROUGH LAND SURFACES

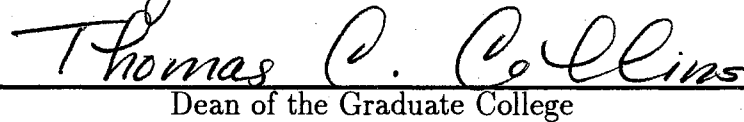
Thesis Approved:

  
\_\_\_\_\_  
Thesis Advisor

  
\_\_\_\_\_

  
\_\_\_\_\_

  
\_\_\_\_\_

  
\_\_\_\_\_  
Dean of the Graduate College

# ACKNOWLEDGMENTS

I extend my sincere thanks and appreciation to the many people who have made this dissertation possible. My thesis advisor Dr. James C. West has been invaluable in his guidance, helpful suggestions, encouragement, and expertise. His confidence in me has motivated me to pursue and complete this endeavor. I would also like to thank my committee members, Dr. George Scheets, Dr. Hans Bilger, and Dr. John Chandler for their helpful suggestions and support during this effort. My dissertation is dedicated to my wife Cindy and my parents Gene and Phyllis Sturm. Through their unfailing love, encouragement, and patience, they have inspired me to reach this goal. This work was supported in part by the Office of Naval Research under grant N00014-92-J-1206 and by the Air Force Office of Scientific Research Graduate Student Research Program and Summer Research Extension Program.

# TABLE OF CONTENTS

<b>1</b>	<b>INTRODUCTION</b>	<b>1</b>
<b>2</b>	<b>BACKGROUND</b>	<b>6</b>
2.1	Scattering Geometry . . . . .	6
2.2	Generation of Random Surface Models . . . . .	8
2.3	Electromagnetic Analysis . . . . .	13
<b>3</b>	<b>REVIEW OF TRADITIONAL SCATTERING THEORIES</b>	<b>16</b>
3.1	Kirchhoff Approximation . . . . .	16
3.2	Small Perturbation Model . . . . .	18
3.3	Two-Scale Model . . . . .	20
3.4	Limitations . . . . .	21
<b>4</b>	<b>REVIEW OF THE MOMENT METHOD</b>	<b>24</b>
4.1	Description . . . . .	25
4.2	Perfectly Conducting Surfaces . . . . .	28
4.3	High Dielectric-Constant, High-Loss Surfaces . . . . .	31
4.4	Low-Loss Dielectric Surfaces . . . . .	34
4.5	Scattering by a Circular Cylinder . . . . .	38
4.6	Limitations . . . . .	45
<b>5</b>	<b>HYBRID MM/GTD TECHNIQUE</b>	<b>49</b>
5.1	Perfectly Conducting Surfaces . . . . .	50
5.2	High Dielectric-Constant, High-Loss Surfaces . . . . .	53
5.3	Low-loss Dielectric Surfaces . . . . .	55
5.4	Implementation Considerations . . . . .	56
5.4.1	Evaluation of the Linear System . . . . .	57
5.4.2	Far-field Scattering Calculations . . . . .	63
5.5	Evaluation of the Hybrid MM/GTD Technique . . . . .	65

<b>6 APPLICATION</b>	<b>70</b>
6.1 Description . . . . .	70
6.2 Backscattering Calculations . . . . .	76
6.2.1 Perfectly Conducting Reference Surfaces . . . . .	77
6.2.2 Moist Clay Surface ( $\epsilon_r = 35 - j5$ ) . . . . .	80
6.2.3 Average Soil Surface ( $\epsilon_r = 10 - j2$ ) . . . . .	83
6.2.4 Dry Sand Surface ( $\epsilon_r = 3 - j0$ ) . . . . .	86
6.3 Surface Current Magnitudes . . . . .	88
6.4 Discussion . . . . .	94
<b>7 SUMMARY AND CONCLUSIONS</b>	<b>97</b>
<b>BIBLIOGRAPHY</b>	<b>100</b>

# LIST OF TABLES

4.1	Average Magnitude Errors (dB) for Circular Cylinder Scattering. . . .	45
4.2	Average Angular Placement Errors ( $^{\circ}$ ) for Circular Cylinder Scattering.	45
5.1	Reductions in the rounded wedge backscatter, vertical polarization. . .	68
5.2	Reductions in the rounded wedge backscatter, horizontal polarization.	69

# LIST OF FIGURES

1.1	Surface self-shadowing and multipath scatter. . . . .	3
2.1	Rough surface scattering geometry, horizontal polarization. . . . .	7
2.2	Rough surface scattering geometry, vertical polarization. . . . .	7
2.3	A typical power law surface. . . . .	10
2.4	Normalized autocorrelation function for a power law surface. . . . .	11
2.5	A typical Gaussian surface. . . . .	12
2.6	Normalized autocorrelation function for a Gaussian surface. . . . .	12
2.7	Physical equivalent model for a perfectly conducting surface. . . . .	14
3.1	Geometry for magnetic field integral equation. . . . .	17
3.2	Bragg-resonant scattering. . . . .	19
4.1	Current approximation using pulse basis functions. . . . .	27
4.2	Equivalent problem to be solved with high loss dielectric scatterer. . .	31
4.3	Snell's law of refraction for a dielectric surface. . . . .	32
4.4	External and internal equivalent problems. . . . .	35
4.5	Scattering geometry for lossy dielectric cylinder. . . . .	39
4.6	Scattering from a perfectly conducting cylinder, vertical polarization. .	40
4.7	Scattering from a dielectric cylinder $\epsilon_r = 3 - j0$ , vertical polarization.	41
4.8	Scattering from a dielectric cylinder $\epsilon_r = 10 - j2$ , vertical polarization.	41
4.9	Scattering from a dielectric cylinder $\epsilon_r = 35 - j5$ , vertical polarization.	42

4.10	Scattering from a perfectly conducting cylinder, horizontal polarization. . . . .	42
4.11	Scattering from a dielectric cylinder $\epsilon_r = 3 - j0$ , horizontal polarization. . . . .	43
4.12	Scattering from a dielectric cylinder $\epsilon_r = 10 - j2$ , horizontal polarization. . . . .	43
4.13	Scattering from a dielectric cylinder $\epsilon_r = 35 - j5$ , horizontal polarization. . . . .	44
4.14	Effects of illumination angle on the Thorsos weighting function. . . . .	46
4.15	Rounded wedge scattering geometry. . . . .	47
4.16	Effects of illumination weighting function, vertical polarization. . . . .	47
4.17	Effects of illumination weighting function, horizontal polarization. . . . .	48
5.1	Arbitrary scattering surface. . . . .	50
5.2	Diffracted field in the vicinity of the extensions. . . . .	51
5.3	Vertical scattering from perfectly conducting rounded wedge. . . . .	66
5.4	Horizontal scattering from perfectly conducting rounded wedge. . . . .	67
5.5	Scattering from rounded-apex wedge: vertical polarization. . . . .	67
5.6	Scattering from rounded-apex wedge: horizontal polarization. . . . .	68
6.1	Large-scale displacement for full Stokes wave with sharp crests. . . . .	71
6.2	Large-scale displacement for full Stokes wave with rounded crests. . . . .	72
6.3	Large-scale displacement for half Stokes wave with rounded crests. . . . .	72
6.4	“Rough-in-shadow” geometry for weak-shadowing surface. . . . .	73
6.5	“Rough-in-shadow” geometry for deep-shadowing surface. . . . .	74
6.6	“Smooth-in-shadow” geometry for weak-shadowing surface, $\theta_g = 10^\circ$ . . . . .	75
6.7	“Smooth-in-shadow” geometry for deep-shadowing surface, $\theta_g = 10^\circ$ . . . . .	75
6.8	Backscattering for perfectly conducting weak-shadowing surface. . . . .	78
6.9	Backscattering for perfectly conducting deep-shadowing surface. . . . .	79
6.10	Backscattering for “moist-clay” weak-shadowing surface. . . . .	81
6.11	Backscattering for “moist-clay” deep-shadowing surface. . . . .	81
6.12	Backscattering for a “typical-soil” weak-shadowing surface. . . . .	84



6.13 Backscattering for a “typical-soil” deep-shadowing surface. . . . .	84
6.14 Backscattering for a “dry-sand” weak-shadowing surface. . . . .	86
6.15 Backscattering for a “dry-sand” deep-shadowing surface. . . . .	87
6.16 Current magnitudes for $\theta_g = 10^\circ$ , perfect conductor, deep-shadowing surface. . . . .	89
6.17 Current magnitudes for $\theta_g = 10^\circ$ , $\epsilon_r = 35 - j5$ , deep-shadowing surface.	90
6.18 Current magnitudes for $\theta_g = 10^\circ$ , $\epsilon_r = 10 - j2$ , deep-shadowing surface.	90
6.19 Current magnitudes for $\theta_g = 10^\circ$ , $\epsilon_r = 3 - j0$ , deep-shadowing surface.	91
6.20 Current magnitudes for $\theta_g = 0^\circ$ , perfect conductor, deep-shadowing surface. . . . .	92
6.21 Current magnitudes for $\theta_g = 0^\circ$ , $\epsilon_r = 35 - j5$ , deep-shadowing surface.	92
6.22 Current magnitudes for $\theta_g = 0^\circ$ , $\epsilon_r = 10 - j2$ , deep-shadowing surface.	93
6.23 Current magnitudes for $\theta_g = 0^\circ$ , $\epsilon_r = 3 - j0$ , deep-shadowing surface.	93

# NOMENCLATURE

dB	decibels
$\epsilon$	permittivity
$\epsilon_r$	relative permittivity or dielectric constant
$\eta_0$	free space intrinsic impedance
$E^i, E^i$	incident electric field
$E^s, E^s$	scattered electric field
EFIE	electric field integral equation
$F$	arbitrary field quantity $E$ or $H$
GO	geometrical optics
GTD	geometrical theory of diffraction
$H_n^{(2)}$	$n$ -th order Hankel function of second type
$H^i, H^i$	incident magnetic field
$H^s, H^s$	scattered magnetic field
HH	horizontal polarization
$j$	$\sqrt{-1}$
$J, J$	electric surface current density
$k$	wave number
$K$	Bragg-resonant surface wave number
KA	Kirchhoff approximation

$l, l'$	arc length along surface at observation, source
$L$	correlation length
$L[]$	linear operator
$\lambda$	illuminating field wavelength
$\Lambda$	surface wavelength
$\mathbf{M}, M$	magnetic surface current density
MFIE	magnetic field integral equation
MM	moment method
$\mu$	permeability
$\mu_0$	permeability of free space
$\mu_r$	relative permeability
$\hat{\mathbf{n}}, \hat{\mathbf{n}}'$	unit vector normal to surface at observation, source
$\mathbf{r}, \mathbf{r}'$	position vector of observation, source point
$\rho$	surface radius of curvature
PO	physical optics
S	surface
$\sigma_{HH}, \sigma_{VV}$	backscattering coefficients
$\sigma^2$	variance of surface height
SPM	small perturbation method
$\theta_g$	grazing angle of illuminating field (referenced to horizontal)
$\theta_i$	incident angle of illuminating field (referenced to vertical)
$\theta_s$	angle of scattered field, referenced to vertical
TSM	two-scale model
VV	vertical polarization
$W(K)$	surface power spectral density function
$(x, y)$	coordinates of a point on the scattering surface

# Chapter 1

## INTRODUCTION

Electromagnetic scattering from rough land surfaces is an important research topic for both military and scientific radar applications. Military applications include the suppression of ground clutter that can hide low-flying targets such as aircraft or cruise missiles. Similarly, scientists applying synthetic aperture radar (SAR) to study environmental changes on the Earth's surface also need a better understanding of the scattering mechanisms in order to improve the analysis of the radar data. Of particular interest is the scattering from a rough terrain when illuminated by the radar at small grazing angles. Under these conditions, the geographical features cast shadows that greatly complicate the scattering problem. Unfortunately, analytical solutions to Maxwell's equations are not possible for such problems due to the random nature of the scattering surface, and approximate analytical solutions are not valid for small grazing angles of illumination. Numerical techniques may provide an accurate alternative to analytical models, but finite computer resources severely limit the size of the surfaces that can be modeled.

Approximate analytical solutions to rough surface scattering problems include the Kirchhoff approximation (KA), the small-perturbation model (SPM), and the two scale model (TSM). The Kirchhoff approximation of Beckmann and Spizzichino [1] uses the physical optics (PO) current on planes tangent to a slightly rough scattering surface to approximate the true induced current. The Kirchhoff approximation only gives a

good estimate of the locally specular reflection from the surface, and fails for small grazing angles of incidence where surface self-shadowing is significant. It is valid for “gently undulating” surfaces with large radii of curvature compared to the wavelength of the illuminating field and at moderate incidence angles [2].

In the small perturbation model (SPM) of Rice [3], the induced current and scattered fields are found first for a smooth surface and then perturbed to account for a superimposed small-scale roughness that is assumed to be smaller than the incident wavelength. SPM accurately predicts the Bragg-resonant scattering thought to be the dominant scattering mechanism on many types of rough surfaces, but is limited in applicability to surfaces with electrically small features and at only moderate grazing illumination angles.

The two-scale model (TSM) [4] [5] attempts to combine the benefits of the Kirchhoff and small perturbation theories into a single model. A small-scale roughness that follows the small-perturbation model is superimposed upon large-scale features that follow the Kirchhoff approximation. Although the TSM has been used successfully to predict the scattering from more realistic surfaces than either the KA or SPM, its validity conditions follow directly from KA and SPM. Hence it is unsuitable for predicting scatter when the illumination grazes the surface at a small angle.

Approximate scattering theories fail under these extreme illumination conditions in part because they neglect surface self-shadowing and multipath scatter. As shown in Figure 1.1, the surface can be directly illuminated by the incident field or indirectly illuminated by diffracted and multipath scattered fields. Diffracted fields appear to emanate from illuminated edges on the shadowing obstacle and can propagate into the shadowed region [6]. Another form of diffraction is “creeping diffraction” in which a surface wave propagates over a curved obstacle and detaches [6]. Multipath scatter occurs when the illuminating field induces surface currents that radiate and illuminate

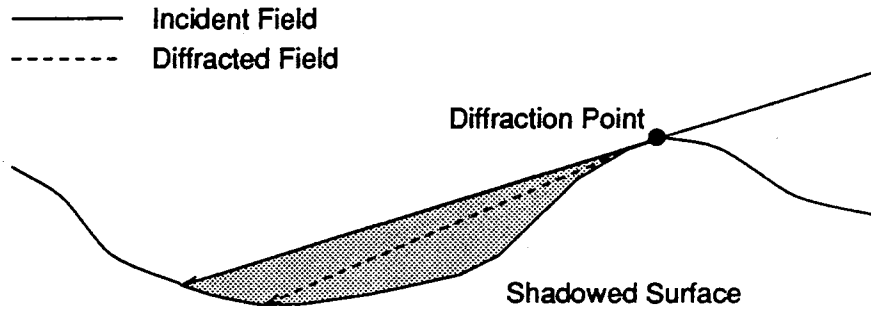


Figure 1.1: Surface self-shadowing and multipath scatter.

other portions of the surface [7].

Corrections to the approximate scattering models can be made to attempt to account for shadowing. Typically, the shadowed regions of the surface are determined using geometrical optics (GO), and the currents in these regions are set to zero so that they do not contribute to the radiated field. This simple correction yields acceptable results at the onset of shadowing since the dominant scatter is from the directly illuminated surface features. However, for small illumination grazing angles much of the surface is shadowed, and the relative contributions of the nonzero currents in the shadowed regions may become more important. Recent studies have suggested that small scale roughness features in shadowed regions of perfectly conducting surfaces can significantly contribute to the total scattered field [8] [9] [10].

While the shadowing corrections to the traditional scattering models do not account for diffracted fields or multipath scatter in the shadowed regions, an analysis based upon the moment method (MM) [11] accurately predicts the induced surface current on every part of the scattering surface. In this numerical technique, the unknown surface current density is represented in an integro-differential equation in terms of the known electric or magnetic fields. The scattering surface is divided into segments, and the boundary conditions set by the integral equation are satisfied only on discrete points of the surface. The resulting system of linear equations then must be solved for the unknown current density on the surface segments, and finally the far-field scatter

is found by radiating the current using Maxwell's equations.

Since the order of the system of linear equations is dependent upon the square of the number of surface segments, a moment method analysis of scattering from a large surface can be computationally expensive. A reduction in the number of computations can be made by artificially truncating the modeled surface, which unfortunately introduces nonexistent edge diffraction into the scatter. The moment method treats the artificial edge as a real edge that diffracts the illuminating field, causing unrealistic diffracted fields to propagate to the far-field and to incorrectly illuminate other parts of the modeled surface. One way to alleviate this problem is to taper the illuminating field to a small magnitude at the edges of the modeled surface. Electromagnetically valid beams give very unrealistic illumination for small grazing angles unless a very large surface is used. Thus, applying the moment method at small grazing angles is computationally prohibitive.

A hybrid moment-method/geometrical-theory-of-diffraction (MM/GTD) technique has been developed and implemented to overcome many of the inadequacies of the traditional techniques for the analysis of scatter from rough surfaces by grazing illumination [12] [10]. In this numerical method, the currents on large portions of the scattering surface are represented using simple basis functions that are derived from the GTD fields at the surface. West [10] used the technique to examine the relative contributions of small-scale roughness on shadowed portions of perfectly conducting surfaces representing near-breaking ocean waves.

The purpose of this work is to investigate the relative contributions to the scattered field of shadowed roughness on lossy and low-loss dielectric surfaces representative of moist and dry soil, respectively. First, a detailed review of the scattering problem will be given, followed by reviews of the approximate theories and numerical techniques that can be used to solve for the scattered fields. The hybrid MM/GTD technique will

be reviewed, and an extension of the technique for low-loss dielectric boundaries will be presented. Next, the accuracy of the hybrid technique will be evaluated against theory and other numerical techniques for scattering from simple surfaces. Finally, the hybrid technique will be used to find the scatter from surfaces representative of rough land surfaces. Of particular interest is the relative contributions of small scale roughness features in the shadow of large scale features.



# Chapter 2

## BACKGROUND

The purpose of this chapter is to introduce the scattering problem geometry, to define the surface roughness and electrical properties, and to review the pertinent electromagnetic scattering theory.

### 2.1 Scattering Geometry

The problem of scattering from a three-dimensional rough surface is beyond the scope of this work due to the tremendous computational requirements for such a problem. Instead, it is useful for the purpose of discussion and analysis to define a two-dimensional scattering problem in which the surface has roughness features in only one dimension, as illustrated in Figures 2.1 and 2.2 for horizontal and vertical polarizations, respectively.

For the purposes of this investigation, the surface is assumed to be in the far-field of both the illuminating and receiving antennas. Hence, the illumination and scattered fields are approximated by uniform plane waves [13]. When both the incident (transmitted) and scattered (received) electric fields are parallel to the scattering surface, as shown in Figure 2.1, the scatter is said to be *horizontally polarized* (HH). Likewise, when the incident and scattered magnetic fields are parallel to the surface, as shown in Figure 2.2, the scatter is *vertically polarized* (VV). In the figures, the positive

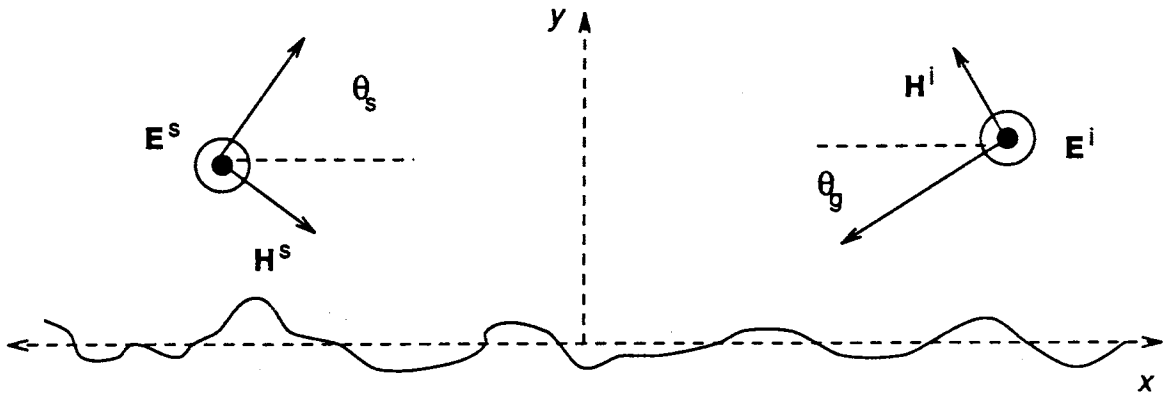


Figure 2.1: Rough surface scattering geometry, horizontal polarization.

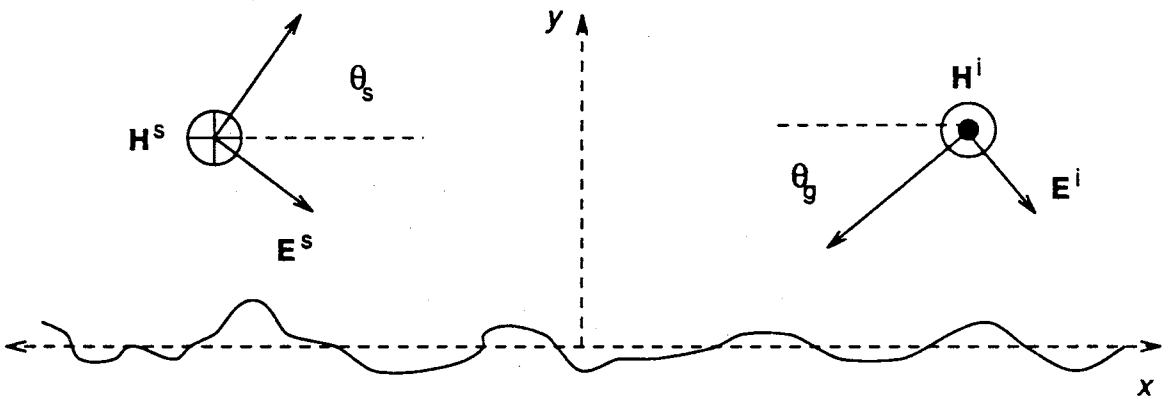


Figure 2.2: Rough surface scattering geometry, vertical polarization.

$z$  direction (out of the page) is denoted by  $\odot$ , and the negative  $z$  direction (into the page) is denoted by  $\oplus$ . All plots in this paper will use grazing angles (referenced to horizontal) for the illumination angle  $\theta_g$  and observation angle  $\theta_s$ . However, some equations will use an incident angle  $\theta_i$  referenced to vertical where  $\theta_i = \pi/2 - \theta_g$ .

## 2.2 Generation of Random Surface Models

It is impractical to model a large land or ocean surface using most numerical techniques, even in only one-dimension of roughness, because such an analysis would surpass the finite memory capacity of even the most sophisticated supercomputer. Instead, it is necessary to study relatively small surface models that are perhaps only one hundred wavelengths or less in length but include the roughness characteristics of actual surfaces.

Although ocean and land surfaces may have many scales of roughness, only large and small-scale roughness features are included on the representative surfaces in this investigation. The scattering from such two-scale surfaces has been investigated extensively and is well understood for large grazing illumination angles. The scale of roughness is determined by comparing its mean radius of curvature with the illuminating field wavelength. The height  $y$  at any position along the modeled surface is given by  $y(x) = l(x) + s(x)$ , where  $l(x)$  and  $s(x)$  are functions characteristic of the large- and small-scale roughness, respectively. In this study, the large-scale roughness will be represented by a deterministic function approximating the large-scale displacements found on land surfaces. Small-scale roughness features will be represented with a random function. Note that the rough surface models shown in Figures 2.1 and 2.2 have only a small-scale roughness component.

A review of the spectral technique used to generate randomly rough surfaces is given in [14] and summarized here. For a given surface, the normalized surface auto-

correlation function [15]

$$R(\tau) = E[y(x)y(x - \tau)], \quad (2.1)$$

where  $E[\ ]$  is the expected value operator, gives an indication of the similarity between the surface heights at points  $x$  and  $x - \tau$  along the surface. The correlation length  $L$  of the surface is often defined to be the distance between points on the surface that gives  $R(L) = 1/e$  [15]. Taking the Fourier transform of equation (2.1) yields the surface power spectral density function [16]

$$\begin{aligned} W(K) &= \frac{1}{2\pi} \int_{-\infty}^{\infty} R(\tau)e^{-jK\tau} d\tau \\ &= E\{F[y(x)y(x - \tau)]\} \\ &= E\{|Y(K)|^2\} \end{aligned} \quad (2.2)$$

where  $K$  is surface wave number, and  $Y(K)$  is the amplitude spectrum found by taking the Fourier transform of a sample surface.

The goal of the spectral surface-generation technique is to generate a sample surface with the desired statistical roughness defined by the power spectral density function. It can be shown that if the amplitude spectrum is chosen to be

$$Y(K) = N(K)\sqrt{W(K)}, \quad (2.3)$$

where  $N(K)$  is the Fourier transform of a real, white noise process  $n(x)$ , then a sample surface can be generated using the inverse Fourier transform [14]

$$y(x) = F^{-1} \left[ N(K)\sqrt{W(K)} \right], \quad (2.4)$$

where  $W(K)$  is now the *desired* power spectral density function.

Natural surfaces often have power spectral density functions that follow power law functions [17]. One such power-spectral density function is the saturated region of the one-dimensional Pierson-Moskowitz ocean wind-wave spectrum given by [18] [19]

$$W(K) = \begin{cases} 0 & \text{if } |K| < K_0 \\ \alpha/4|K|^3 & \text{otherwise} \end{cases} \quad (2.5)$$

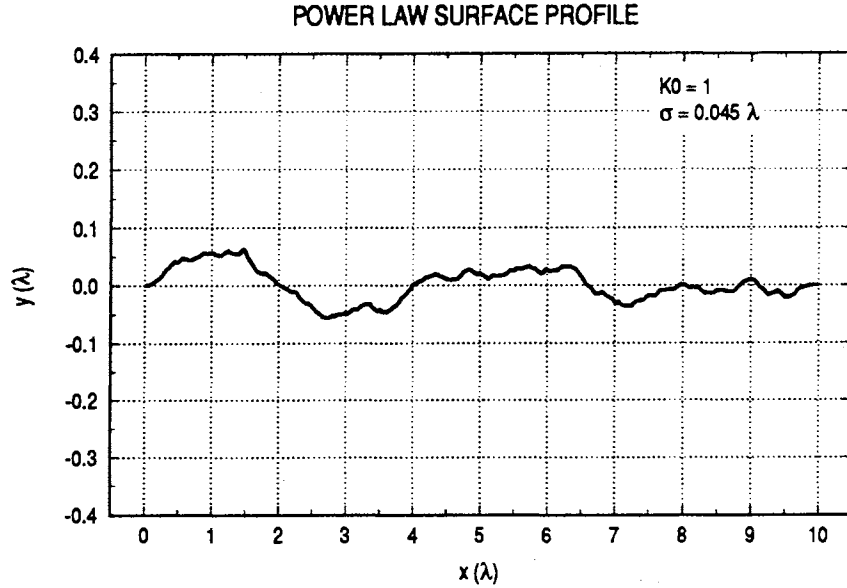


Figure 2.3: A typical power law surface.

where  $\alpha = 0.0081$ ,  $K_0$  is an arbitrary threshold value, and  $K$  is the surface-wave spatial wave number. The surface height variance

$$\sigma^2 = \int_{-\infty}^{\infty} W(K) dK = \frac{\alpha}{2K_0^2} \quad (2.6)$$

can be adjusted with the  $K_0$  threshold. Although this spectrum is not suitable for modeling rough land surfaces, it is believed that an inverse power law spectrum  $W(K) \propto |K|^{-2.5}$  can be applied to geological features [20] [17]. An example of a zero-mean power law surface is shown in Figure 2.3. Figure 2.4 compares the average normalized autocorrelation function for 500 independent power law surfaces to the theoretical normalized autocorrelation found by numerically evaluating the inverse Fourier transform integral of the power spectral density function in equation (2.5).

Numerous rough-surface scattering studies have used not a power-law spectrum but a Gaussian spectrum to describe the power spectral density of a surface height distribution. The autocorrelation and power spectral density functions of a Gaussian

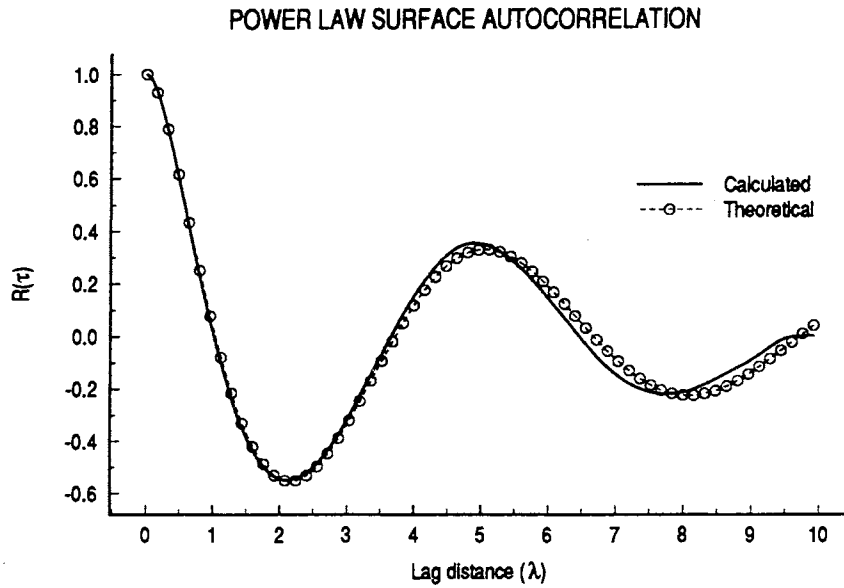


Figure 2.4: Normalized autocorrelation function for a power law surface.

surface are given by

$$R(\tau) = \sigma^2 \exp[-(\tau/L)^2], \quad (2.7)$$

and

$$W(K) = \frac{\sigma^2 L}{2\sqrt{\pi}} \exp\left(-\frac{L^2 K^2}{4}\right), \quad (2.8)$$

respectively, where  $\sigma$  is the surface displacement standard deviation and  $L$  is the correlation length. An example of a zero-mean Gaussian surface is illustrated in Figure 2.5. The average normalized autocorrelation function for 300 independent Gaussian surfaces is compared to the theoretical autocorrelation function from equation (2.7) in Figure 2.6.

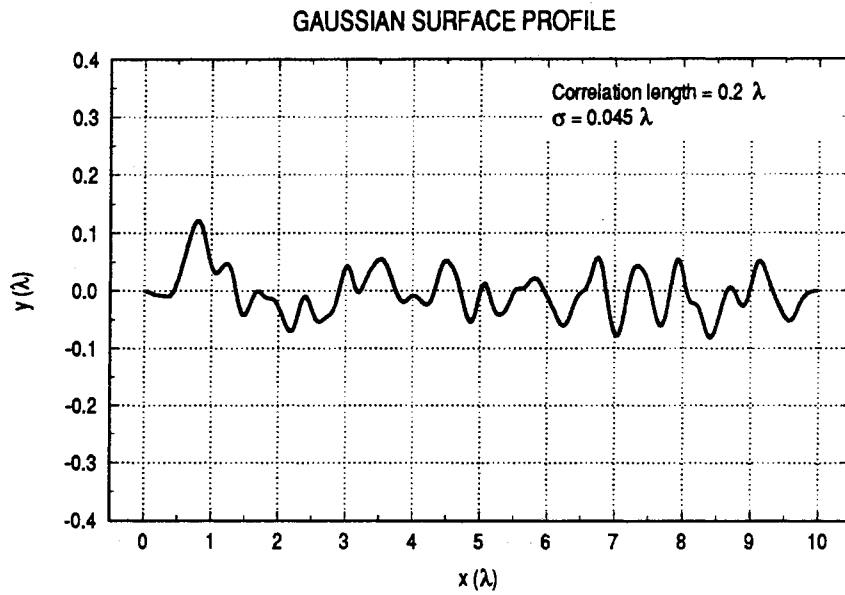


Figure 2.5: A typical Gaussian surface.

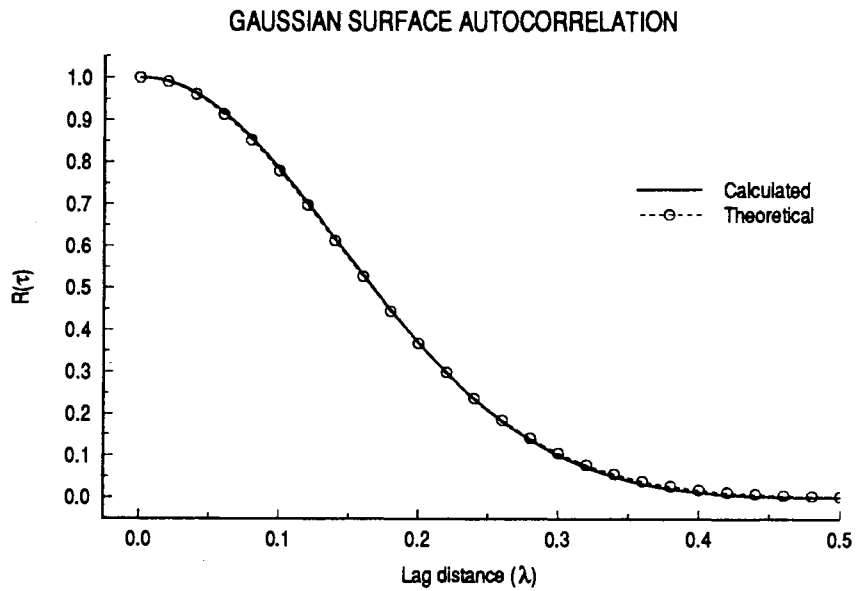


Figure 2.6: Normalized autocorrelation function for a Gaussian surface.

## 2.3 Electromagnetic Analysis

A discussion of the electromagnetic analysis of scattering should begin with Maxwell's equations. Any solution for the time-harmonic electric and magnetic scattered fields in a homogeneous medium must satisfy [7]

$$\begin{aligned}\nabla \times \mathbf{E} &= -\mathbf{M} - j\omega\mu\mathbf{H} \\ \nabla \times \mathbf{H} &= \mathbf{J} + j\omega\epsilon\mathbf{E} \\ \nabla \cdot \mathbf{E} &= \frac{q_{ve}}{\epsilon} \\ \nabla \cdot \mathbf{H} &= \frac{q_{vm}}{\mu},\end{aligned}\tag{2.9}$$

where  $\omega$  is the radial frequency,  $\mathbf{E}$  and  $\mathbf{H}$  are the electric and magnetic field intensities,  $\mathbf{J}$  and  $\mathbf{M}$  are the electric and magnetic current densities, and  $q_{ve}$  and  $q_{vm}$  are the electric and magnetic charge densities, respectively. Although the magnetic current density  $\mathbf{M}$  and the magnetic charge densities  $q_{vm}$  do not represent actual quantities, hypothetical equivalent magnetic currents and/or charges often simplify the treatment of the scattering problem. The permittivity and permeability of the material are given by

$$\begin{aligned}\epsilon &= \epsilon_r\epsilon_0 \\ \mu &= \mu_r\mu_0,\end{aligned}\tag{2.10}$$

respectively, where  $\epsilon_0 \cong 8.854 \times 10^{-12}$  farads per meter is the permittivity of free space,  $\mu_0 \cong 4\pi \times 10^{-7}$  henry per meter is the permeability of free space,  $\epsilon_r$  is the complex relative permittivity (dielectric constant), and  $\mu_r$  is the relative permeability.

In an actual scattering problem, the incident (or direct) fields induce currents on or within the scattering material. Surface current densities are induced upon perfectly conducting scatterers, while volume current densities are induced upon dielectric scatterers. The scattered field is produced by the radiation of these currents, and the total



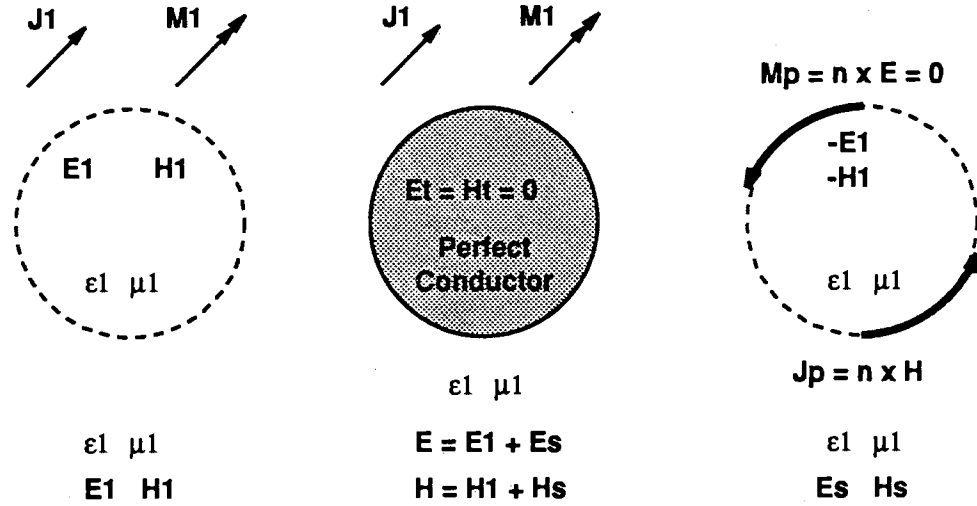


Figure 2.7: Physical equivalent model for a perfectly conducting surface.

field outside of the scattering material is the superposition of the incident and scattered fields. Commonly, the differential forms of Maxwell's equations in (2.9) are manipulated to integral equations that can be solved numerically for the unknown current densities, and then the scattered field is found by evaluating radiation integrals.

Often it is convenient to solve for not the actual induced currents but for equivalent currents that, when reradiated, give the actual scattered field. An example of this technique is illustrated in Figure 2.7 (adapted from [7]), which shows a scattering problem for a perfectly conducting surface and its physical equivalent. In the absence of a scattering surface (shown in the left picture), the external sources  $\mathbf{J}_1$  and  $\mathbf{M}_1$  radiate an electric field,  $\mathbf{E}_1$ , and magnetic field,  $\mathbf{H}_1$ , which are known everywhere. In the middle picture, the introduction of the scattering surface gives rise to external fields  $\mathbf{E} = \mathbf{E}_1 + \mathbf{E}^s$  and  $\mathbf{H} = \mathbf{H}_1 + \mathbf{H}^s$ . The physical equivalent model is shown on the right in which the surface is removed and equivalent sources  $\mathbf{J}_p$  and  $\mathbf{M}_p$  are placed on the boundary. The magnetic current density  $\mathbf{M}_p$  is zero in the equivalent model because the tangential electric fields are zero on a perfectly conducting boundary. The electric current source  $\mathbf{J}_p$  radiates *in an unbounded medium* and gives valid scattered fields in the region *external to the boundary only*. The physical equivalent model is

used extensively in the moment method numerical technique. Other equivalent models can be used for analysis of scatter from dielectric materials.

Once the scattered fields are found, it is useful to find the surface *radar cross section* (RCS), which is defined to be [13],

the area intercepting the amount of power that, when scattered isotropically, produces at the receiver a density that is equal to the density scattered by the actual target.

For two-dimensional targets of interest in this study, the *scattering width*, [7]

$$\sigma = \lim_{\rho \rightarrow \infty} \left[ 2\pi\rho \left| \frac{F^s}{F^i} \right|^2 \right], \quad (2.11)$$

represents the radar cross section per unit length, where  $\rho$  is the distance from the target to the observation point and  $F^i$  and  $F^s$  are the incident and scattered fields (electric or magnetic), respectively. In *monostatic* scattering (or backscattering), the illumination and observation angles are the same,  $\theta_g = \theta_s$ . In all other cases, the scattering is *bistatic*.

The power scattered from a random rough surface follows a chi-square distribution, so it is necessary to average the scattering width for many different surface realizations. A Monte Carlo simulation is used to incoherently add the scattered field magnitudes for  $N_s$  independent surfaces. The *ensemble average scattering width* is then given by [21]

$$\bar{\sigma} = \lim_{\rho \rightarrow \infty} \frac{2\pi\rho}{N_s} \left[ \sum_{k=1}^{N_s} \left| \frac{F_k^s}{F_k^i} \right|^2 - \frac{1}{N_s} \left| \sum_{k=1}^{N_s} \frac{F_k^s}{F_k^i} \right|^2 \right], \quad (2.12)$$

where  $F_k^i$  and  $F_k^s$  are the incident and scattered fields for the  $k$ -th independent surface realization. The standard deviation of the estimated scattering width  $\bar{\sigma}$  for  $N_s$  samples is then given by [15]

$$S.D. = 1/\sqrt{N_s}. \quad (2.13)$$

# Chapter 3

## REVIEW OF TRADITIONAL SCATTERING THEORIES

This chapter will review three fundamental theories which describe electromagnetic scattering — the Kirchhoff Approximation (KA), the Small Perturbation Model (SPM), and the Two-Scale Model (TSM). A section at the end of this chapter will discuss the limitations of each theory.

### 3.1 Kirchhoff Approximation

The primary assumption in the Kirchhoff approximation is that the induced surface current can be approximated by the physical optics (PO) currents [7]

$$\mathbf{J}_{\text{PO}} = 2\hat{\mathbf{n}} \times \mathbf{H}^i, \quad (3.1)$$

on planes tangent to the surface, where  $\mathbf{J}_{\text{PO}}$  is the induced surface current density,  $\hat{\mathbf{n}}$  is the unit vector normal to the surface, and  $\mathbf{H}^i$  is the incident magnetic field intensity. Equation (3.1) is valid for perfectly conducting surfaces with a radius of curvature much larger than the incident field wavelength, in the absence of shadowing, and at large grazing incidence [7].

For vertical polarization, the scattered far-field magnetic field intensity is found

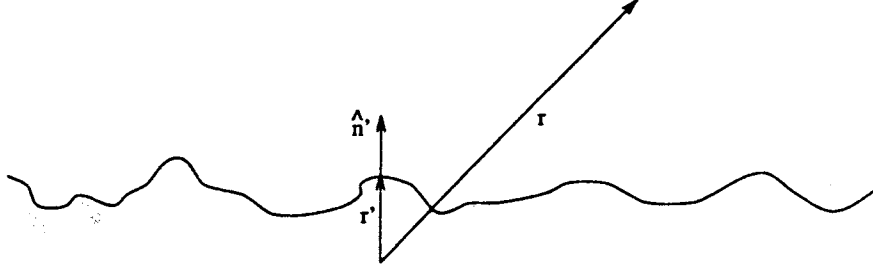


Figure 3.1: Geometry for magnetic field integral equation.

from [7]

$$H^s(r) = \left[ j \frac{k}{4} \int_S J_s(r') (\hat{\mathbf{n}}' \cdot \mathbf{r}') H_1^{(2)}(k|r - r'|) dS' \right] \Big|_{r \rightarrow \infty}, \quad (3.2)$$

where  $J_S(r')$  is the surface current density,  $r$  is the observation vector,  $r'$  is the source vector,  $\hat{\mathbf{n}}'$  is the unit vector normal to the surface at the source point as shown in Figure 3.1, and  $H_n^{(2)}$  is the  $n$ -th order Hankel function of the second type. The free-space wave number is given by  $k = \omega \sqrt{\mu_0 \epsilon_0}$ , where  $\omega$  is the radial frequency of the incident field,  $\mu_0$  is the permeability of free space, and  $\epsilon_0$  is the permittivity of free space. For horizontally polarized scattering the far-field is found using [7]

$$E^s(r) = - \left[ \frac{k \eta_0}{4} \int_S J_s(r') H_0^{(2)}(k|r - r'|) dS' \right] \Big|_{r \rightarrow \infty}, \quad (3.3)$$

where  $\eta_0$  is the free space intrinsic impedance. The Kirchhoff approximation (KA) scattering for vertical and horizontal polarizations is found by substituting the PO current of equation (3.1) for  $J_S$  in equations (3.2) and (3.3), respectively.

The backscattering coefficient measures the ratio of the scattered field power to the incident field power for cases when the illumination and observation angles are the same (monostatic scattering). It can be shown that for both horizontal (HH) and vertical (VV) polarizations, the backscattering coefficient for a surface with a Gaussian height distribution and wave number spectrum (hereafter referred to as a ‘‘Gaussian surface’’) is given as [14]

$$\sigma_{HH}(\theta_i) = \sigma_{VV}(\theta_i) = \frac{|\Gamma|^2 \exp(-\tan^2 \theta_i L^2 / 4\sigma^2)}{\cos^4 \theta_i 4\sigma^2 / L^2}, \quad (3.4)$$

where  $\sigma^2$  is the variance of the surface height,  $L$  is the surface correlation length, and  $\Gamma$  is the reflection coefficient at normal incidence. Since  $\sigma_{HH} = \sigma_{VV}$ , it is clear that the Kirchhoff approximation predicts no polarization dependence for backscatter.

When considering electromagnetic scattering from statistically rough surfaces, certain surface conditions must be satisfied for the Kirchhoff approximation to be valid. KA requires that the correlation length must be larger than the wavelength of the illuminating field  $\lambda$ , or for Gaussian spectral surfaces [15]

$$kL > 6. \tag{3.5}$$

Additionally, the vertical-scale roughness of the surface must be small enough that the average radius of curvature is much larger than the incident wavelength, or for Gaussian spectral surfaces [15]

$$L^2 > 2.76\sigma\lambda, \tag{3.6}$$

where  $\sigma$  is the standard deviation of the surface height.

## 3.2 Small Perturbation Model

The small perturbation model (SPM) of Rice [3] can be used for rough surfaces when the surface height standard deviation and slope are much smaller than the incident wavelength. SPM assumes that the scattered field quantities are functions of the surface height and can be expanded as a Taylor series about the mean surface height [2]. The zeroth order solution for the scattering field yields the specular fields reflected from a flat surface, and the first order solution includes the effect of Bragg-resonant scattering.

The Bragg-resonance phenomena can greatly enhance the backscatter of certain frequencies from a rough surface. The rough surface can be considered to be a summation of sinusoids at different amplitudes and frequencies. Under certain conditions,

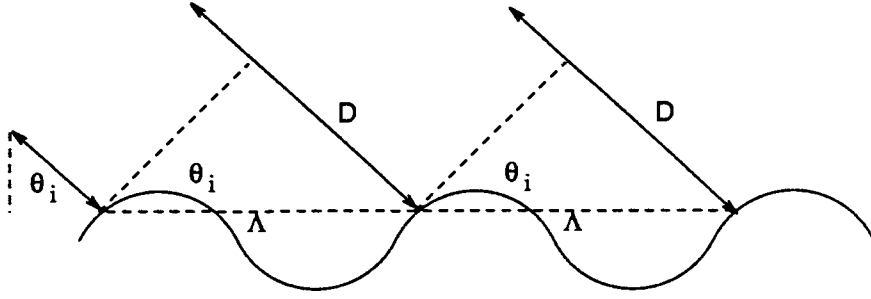


Figure 3.2: Bragg-resonant scattering.

the incident field may be reflected from the periodic components of the surface in a manner that produces constructive interference of the reflected waves at a wavelength corresponding to the surface wavelength. For the case of backscattering, the enhancement is best illustrated in Figure 3.2, adapted from [15]. When the path difference  $2D$  between reflected waves is a multiple of  $\lambda$ , the waves add coherently thus enhancing the reflected energy of that frequency. The Bragg-resonant condition can be stated as

$$D = n \frac{\lambda}{2}, \quad n = 0, 1, 2, \dots \quad (3.7)$$

or in terms of the wavelength of the surface component,  $\Lambda$ , and the incident angle (referenced to vertical)  $\theta_i$ , [15]

$$\frac{2\Lambda}{\lambda} \sin \theta_i = n, \quad n = 0, 1, 2, \dots, \quad (3.8)$$

since  $D = \Lambda \sin \theta_i$ . The Bragg scattering mechanism has been shown to be a significant contributor to the total scatter from small capillary waves that travel upon large ocean waves [15].

For a one-dimensional randomly rough surface with dielectric constant  $\epsilon_r$  and  $\mu_r = 1$ , the backscattering coefficients for horizontal (HH) and vertical (VV) polarizations are given by [15]

$$\sigma_{pq}(\theta_i) = 4k^3 \sigma^2 \cos^4 \theta_i |\alpha_{pq}|^2 W(2k \sin \theta_i), \quad (3.9)$$

where

$$\alpha_{hh} = \frac{\cos \theta_i - \sqrt{\epsilon_r - \sin^2 \theta_i}}{\cos \theta_i + \sqrt{\epsilon_r - \sin^2 \theta_i}},$$

$$\alpha_{vv} = (\epsilon_r - 1) \frac{\sin^2 \theta_i - \epsilon_r \sqrt{1 + \sin^2 \theta_i}}{\left[ \epsilon_r \cos \theta_i + \sqrt{\epsilon_r - \sin^2 \theta_i} \right]^2}, \quad (3.10)$$

and  $W(K)$  is the surface power spectral density function. The Bragg-resonant surface wave number, given by  $K = 2k \sin \theta_i$ , is included in equation (3.9).

Investigators have found differing conditions under which the small perturbation model is valid. All have agreed, however, that for Gaussian surfaces, the height standard deviation  $\sigma$  and correlation length  $L$  should be smaller than the incident field wavelength. As a guideline for applicability of SPM, Ulaby *et al.* [15] state that for Gaussian spectral surfaces

$$\begin{aligned} k\sigma &< 0.3, \\ \sqrt{2}\sigma/L &< 0.3 \end{aligned} \quad (3.11)$$

must be satisfied.

### 3.3 Two-Scale Model

Many real surfaces have two scales of roughness — a small-scale roughness superimposed upon a large-scale roughness. The sea surface approximately fits this description as small capillary waves ride upon the large-scale ocean waves [2]. For these types of surfaces, the Kirchhoff approximation fails to model the Bragg resonant interactions with the small-scale surface features. Similarly, the small perturbation model cannot be used because it does not account for the large-scale roughness tilting the surface. The two-scale model [4] [5] has been developed to combine the features of both of these models into a composite scattering model. The goal of the two-scale model is to incoherently add the scattering due to the large-scale roughness using the Kirchhoff approximation to the scattering from the first order solution in the small perturbation

method with the local angle of incidence adjusted to account for the tilt of the surface. Hence, the backscattering coefficients for the two-scale model may be written as

$$\sigma_{TSM} = \sigma_{KA} + \sigma_{SPM}, \quad (3.12)$$

where  $\sigma_{SPM}$  is calculated including the tilt of the small-scale surface by the large-scale roughness by using the local angle of incidence rather than the large-scale angle of incidence.

### 3.4 Limitations

Traditional scattering theories may fail when assumptions in the models are not satisfied or when the surface geometry causes surface self-shadowing. While the two-scale model has proven effective in predicting the scattering from rough surfaces at moderate grazing angles, at near grazing angles it performs poorly because surface shadowing is not considered in the model. For these extreme illumination and scattering angles, diffraction into the shadow regions may result in surface currents that when radiated produce significant far-field scatter.

The most straightforward shadowing corrections have used geometrical optics to identify the shadowed regions on the scattering surface and to set the current to zero in these regions. Beckmann [22] proposed a shadowing function that multiplies the scattered field strength by the fraction of the surface that is illuminated. He found that errors in the modeled backscatter from very rough lunar surfaces were significantly reduced. Subsequent investigation by Brockelman and Hagfors [23] attempted to replace the Beckmann shadowing function for backscattering calculations in favor of an empirically-derived shadowing function that considers the fraction of illuminated surface elements that are favorably aligned for specular reflection. In this treatment,



the shadow-corrected Kirchhoff approximation for the surface current becomes

$$J_{SK}(r, r_i, r_s) = S_i(r, r_i)S_s(r, r_s)J_{PO}(r) \quad (3.13)$$

where the Kirchhoff approximation for the surface current is given by equation (3.1), and  $S_i$  and  $S_s$  are shadowing functions. The incident shadowing function  $S_i(r, r_i)$  is unity if the incident field illuminates point  $r$  on the surface without first intersecting a point on the surface  $r_i$  and is zero otherwise. Likewise, the scattered shadowing function  $S_s(r, r_s)$  is unity if the field scattered from point  $r$  on the surface propagates to the far-field observation point without first striking a point  $r_s$  on the surface and is zero otherwise. Wagner [24] and Sancer [25] further advanced the Brockelman and Hagfors shadowing correction by discussing their results in a more statistical analysis. It is important to note that this correction fails to consider the effects of diffraction or multiple scattering.

Thorsos [26] numerically investigated the conditions under which the Kirchhoff approximation fails for a Gaussian surface. In this study, Thorsos compared the bistatic scattering cross section predicted by the Kirchhoff approximation and the shadowing-corrected Kirchhoff approximation with the bistatic scattering cross section predicted by the exact integral equation method (moment method) of Axline and Fung [27]. Thorsos found that the Kirchhoff approximation depended most strongly upon the ratio of the surface correlation length to the wavelength  $L/\lambda$  and the relationship between the incident and scattered angles and the root-mean-squared surface slope  $\psi$  [26]. When the ratio of  $L/\lambda > 1$ , the primary cause of the error in the Kirchhoff approximation was found to be due to shadowing. The errors are not entirely compensated when the Kirchhoff approximation is corrected for shadowing by using geometrical optics to find where the shadowing occurs and to set the surface current on these portions to zero. When  $L/\lambda < 1$ , Thorsos introduces an effective correlation length  $L'$  which, when used in place of the true correlation length  $L$  and in conjunction with a shad-

owing correction, produces accurate results for grazing angles of incidence  $\theta_g \geq 20^\circ$  and  $\psi < 20^\circ$  [26].

Thorsos and Jackson [28] investigated the conditions under which the small perturbation theory fails for a Gaussian surface. Like the previous study of the Kirchhoff approximation, this investigation compared the bistatic scattering cross section predicted by small perturbation theory with the bistatic scattering cross section predicted by the moment method approach of Axline and Fung [27]. The authors found that the first-order small perturbation approximation fails when the surface correlation length  $L$  becomes either too large or too small for fixed root-mean-squared (*rms*) surface height  $h$  [28]. Regions of validity of the first-order approximation were given, and the small slope requirement of SPM was investigated.

More recent investigations have shown that shadowing corrections based upon GO fail for vertically polarized illumination and scattering at near-grazing angles of incidence. An analytical investigation by Brown [29] concluded that surface (or creeping) waves can propagate into shadowed regions, and a numerical study by Holliday [9] found that the shadowing corrections poorly predict the shadow-region currents at vertical polarization. West [10] investigated the effects of surface self-shadowing upon the backscatter from perfectly conducting, ocean-wave-like surfaces with two-scales of roughness at small grazing angles of incidence. The results of this investigation suggested that weakly-shadowed small-scale roughness played a significant role in the total horizontal and vertical backscatter, while strongly-shadowed roughness only significantly contributed to the vertically polarized backscatter. Another study by West *et al.* [30] demonstrated that a sufficient portion of the surface must be illuminated directly in order for the Bragg resonance to be established. For small grazing angles of incidence, it is clear that shadowing corrections to traditional scattering theories are inadequate.

## Chapter 4

# REVIEW OF THE MOMENT METHOD

The hybrid MM/GTD technique that will be used for the numerical calculations of rough surface scattering is an extension of the moment method (MM) of Harrington [11]. A review of the technique following [31] is given here.

The moment method (MM) is used to convert integro-differential equations to a form easily solvable by computers [11]. Two integro-differential equations commonly solved in electromagnetic scattering problems are the electric field integral equation (EFIE) and magnetic field integral equation (MFIE). The EFIE and MFIE represent the current density on the scattering surface in terms of the electric or magnetic field, respectively, in the vicinity of the surface. The discretization of the equation produces a linear matrix equation that can be solved easily by either direct methods (matrix inversion), or by indirect methods (iterative solutions). Once the unknown surface current density is found, the far-field scatter can be calculated by evaluating radiation integrals.

## 4.1 Description

The inhomogeneous equation (EFIE or MFIE) to be solved is represented by

$$L[f(x)] = g(x), \quad (4.1)$$

where  $L$  is a linear integro-differential operator,  $f$  is the unknown function to be determined, and  $g$  is the known driving function. The moment method uses a finite set of independent basis functions to model the unknown function  $f$  as

$$f(x) \cong \sum_{n=1}^N \alpha_n f_n(x), \quad (4.2)$$

where  $f_n(x)$  are the basis functions and  $\alpha_n$  are unknown coefficients. Substituting equation (4.2) into equation (4.1) gives

$$\sum_{n=1}^N \alpha_n L[f_n(x)] = \tilde{g}(x), \quad (4.3)$$

where  $\tilde{g}(x)$  is the approximate driving function.

The residual is defined as the difference between the actual driving function and the approximate driving function obtained from the approximate solution, given by

$$R = g(x) - \tilde{g}(x) = g(x) - \sum_n \alpha_n L[f_n(x)]. \quad (4.4)$$

Since only a finite number of basis functions are used to approximate the driving function, the exact solution cannot in general be obtained, so the residual in equation (4.4) cannot be set equal to zero everywhere on the structure. Instead, the moment method determines a “best” solution by determining the  $\alpha_n$ ’s that force a set of weighted averages of the residual to be zero.

The  $N$  unknown coefficients are determined by forming an inner product between  $N$  appropriately selected weighting functions and both sides of equation (4.3). For a general one-dimensional scattering surface  $S$ , these inner products are of the form

$$\langle w, a \rangle = \int_S (w^* \cdot a) dS, \quad (4.5)$$

where  $w^*$  is the complex conjugate of the weighting function and  $a$  represents either side of equation (4.3). The effect of equation (4.5) is to evaluate equation (4.3)  $N$  times using independent properties of the functions, thus producing a system of  $N$  equations and  $N$  unknowns. The set of weighting functions  $w_m$  must be linearly independent to ensure the  $N$  equations are linearly independent. Additional constraints on the weighting functions are given in [7].

Applying the weighting functions,  $w_m$ , to equation (4.4) gives the  $N$  weighted residuals

$$R_m = \langle w_m, g \rangle - \sum_{n=1}^N \alpha_n \langle w_m, L(f_n) \rangle. \quad (4.6)$$

Setting the weighted residuals equal to zero yields the set of  $N$  linear equations and  $N$  unknowns given by

$$\sum_{n=1}^N \alpha_n \langle w_m, L(f_n) \rangle = \langle w_m, g \rangle; \quad m = 1, \dots, N. \quad (4.7)$$

The matrix form of equation (4.7) is

$$[l_{mn}][\alpha_n] = [g_m], \quad (4.8)$$

where the matrix elements are given by  $l_{mn} = \langle w_m, L(f_n) \rangle$  and the driving vector elements are given by  $g_m = \langle w_m, g \rangle$ . The unknown coefficients  $\alpha_n$  are obtained by evaluating

$$[\alpha_n] = [l_{mn}]^{-1}[g_m], \quad (4.9)$$

completing the approximate solution of the unknown function in equation (4.2). This last step may be performed using direct or iterative methods.

Choosing appropriate basis and weighting functions can greatly simplify the integrals in the inner product calculations of  $l_{mn}$  and  $g_m$  and thereby decrease the computational requirements. To simplify the evaluation of the coefficient matrix integral, subdomain basis functions may be used. These basis functions exist only over a finite portion of the scattering surface, so numerical evaluation of the linear operator in

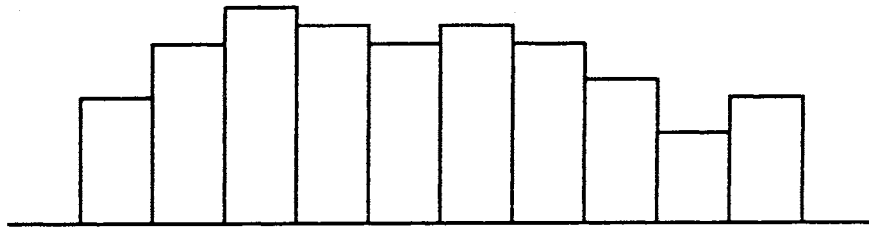


Figure 4.1: Current approximation using pulse basis functions.

equation (4.3) and in the matrix element calculation  $\langle w_m, L(f_n) \rangle$  is simplified. Sub-domain basis functions that have been used in electromagnetic scattering problems include pulse functions, triangular functions, piecewise linear functions, or sinusoidal functions [11]. A pulse function is unity in a given range and zero elsewhere, or

$$P(l - l_m) = \begin{cases} 1 & l_m - \Delta L/2 \leq x \leq l_m + \Delta L/2 \\ 0 & \text{elsewhere} \end{cases}, \quad (4.10)$$

where  $\Delta L$  is the width of the pulse (usually chosen to be  $\ll \lambda$ ),  $l$  is the arc length along the surface, and  $l_m$  is the arc length along the surface at the center of the pulse. Figure 4.1 illustrates a surface current approximation using pulse basis functions.

Dirac delta functions often are chosen for the weighting functions. This technique, called point matching or collocation, simplifies  $\langle w_m, L(f_n) \rangle$  and  $\langle w_m, g \rangle$  to evaluations of  $L(f_n)$  and  $g$  at discrete points on the surface, respectively, causing the residuals to be zero at these points. A further simplification of equation  $\langle w_m, g \rangle$  can be made by using delta functions for both the basis and weighting functions [32].

The moment method can be used to solve for the induced current density on any arbitrary rough surface that varies in only one-dimension, such as those illustrated in Figures 2.1 and 2.2. In order to model the surface current accurately, the surface model first must be divided into segments that are typically much smaller than the incident field wavelength. Axline and Fung [27] found that a sampling distance  $\Delta L < \lambda/5$  is adequate for modeling surfaces with a large scale roughness component. For surfaces with small scale roughness features and with a small correlation length ( $L < \lambda$ ), they

recommend choosing the sampling distance in accordance with the surface correlation length, or [27]

$$\Delta L < L/4, \quad (4.11)$$

in order to prevent aliasing of the surface roughness spectrum.

Once the surface model is divided into sufficiently small segments, an appropriate integral equation that represents the induced surface current density is solved using the moment method with pulse basis and delta weighting functions. The integral equations are derived using the boundary conditions on either the magnetic or electric fields at the surface. The next sections will describe the derivations of these integral equations for perfectly conducting, impedance, and low-loss dielectric surfaces.

## 4.2 Perfectly Conducting Surfaces

On the surface a perfectly conductor, the boundary condition on the magnetic field in three dimensions is given by [7]

$$\mathbf{J}_s(r = r') = \hat{\mathbf{n}} \times [\mathbf{H}^i(r = r') + \mathbf{H}^s(r = r')], \quad (4.12)$$

where  $r'$  is the position vector of the source point,  $r$  is the position vector of the observation point,  $\hat{\mathbf{n}}$  is the unit vector normal to the surface,  $\mathbf{J}_s$  is the surface electric current density, and the total magnetic field at the surface is the sum of the incident magnetic field  $\mathbf{H}^i$  and the scattered magnetic field  $\mathbf{H}^s$ . The scattered magnetic field can be written in terms of the unknown surface current as [7]

$$\mathbf{H}^s(r) = \int_S \mathbf{J}_s(r') \times \nabla' \frac{e^{-jk|r-r'|}}{4\pi|r-r'|} dS' \quad (4.13)$$

where  $S$  indicates the scattering surface, and  $\nabla'$  is the gradient with respect to the source coordinates. Substituting the scattered magnetic field into equation (4.12) and

rearranging yields the three-dimensional magnetic field integral equation (MFIE) [7]

$$\hat{\mathbf{n}} \times \mathbf{H}^i(\mathbf{r} = \mathbf{r}') = \mathbf{J}_s(\mathbf{r} = \mathbf{r}') - \lim_{r \rightarrow S} \left\{ \hat{\mathbf{n}} \times \int_S \mathbf{J}_s(\mathbf{r}') \times \nabla' \frac{e^{-jk|\mathbf{r}-\mathbf{r}'|}}{4\pi|\mathbf{r}-\mathbf{r}'|} dS' \right\}. \quad (4.14)$$

For the two-dimensional, vertically polarized (transverse electric field to  $z$  or TE <sup>$z$</sup> ) scattering from a perfect conductor, the MFIE reduces to the two-dimensional form [11]:

$$\begin{aligned} -H_z^i(l) &= 0.5J_l(l) + j\frac{k}{4} \int J_l(l') (\hat{\mathbf{n}}' \cdot \mathbf{r}') H_1^{(2)}(k|\mathbf{r}-\mathbf{r}'|) dl' \\ &= L_M[J_l(l)], \end{aligned} \quad (4.15)$$

where  $l$  is the arc length along the scattering surface,  $H_z^i(l)$  is the  $z$ -directed incident magnetic field at the scattering surface,  $J_l(l)$  is the unknown surface current,  $\hat{\mathbf{n}}'$  is the normal unit vector at the source point, and  $H_1^{(2)}$  is the first-order Hankel function of the second type. The second term on the right side of equation (4.15) gives the near-field radiation of  $J_l$ , and the other two terms match the surface boundary condition  $\frac{\partial}{\partial n}(H_z^i + H_z^s) = 0$  [7]. The dashed integral in equation (4.15) indicates the principle value integral around the singularity at  $l = l'$ . Note that the singularity contributes  $-0.5J_l(l)$ , thereby making the first term on the right hand side of equation (4.15)  $0.5J_l(l)$ .

The three-dimensional electric field integral equation (EFIE) is derived in terms of the boundary condition on the electric field [7]

$$\hat{\mathbf{n}} \times \mathbf{E}^i(\mathbf{r} = \mathbf{r}') + \hat{\mathbf{n}} \times \mathbf{E}^s(\mathbf{r} = \mathbf{r}') = 0, \quad (4.16)$$

where  $\hat{\mathbf{n}} \times \mathbf{E}^i$  and  $\hat{\mathbf{n}} \times \mathbf{E}^s$  are the tangential components of the incident and scattered electric fields, respectively. The scattered electric field can be written in terms of the unknown surface electric current density as [7]

$$\mathbf{E}^s(\mathbf{r}) = -j\frac{\eta}{k} \left[ k^2 \int_S \mathbf{J}_s(\mathbf{r}') \frac{e^{-jk|\mathbf{r}-\mathbf{r}'|}}{4\pi|\mathbf{r}-\mathbf{r}'|} dS' + \nabla \int_S \nabla' \cdot \mathbf{J}_s(\mathbf{r}') \frac{e^{-jk|\mathbf{r}-\mathbf{r}'|}}{4\pi|\mathbf{r}-\mathbf{r}'|} dS' \right], \quad (4.17)$$



where  $\eta$  is the intrinsic impedance of free space. The three-dimensional form of the EFIE is then found by substituting equation (4.17) into the boundary condition in equation (4.16), or

$$\hat{\mathbf{n}} \times \mathbf{E}^i(\mathbf{r}) = \hat{\mathbf{n}} \times j \frac{\eta}{k} \left[ k^2 \int_S \mathbf{J}_s(\mathbf{r}') \frac{e^{-jk|\mathbf{r}-\mathbf{r}'|}}{4\pi|\mathbf{r}-\mathbf{r}'|} dS' + \nabla \int_S \nabla' \cdot \mathbf{J}_s(\mathbf{r}') \frac{e^{-jk|\mathbf{r}-\mathbf{r}'|}}{4\pi|\mathbf{r}-\mathbf{r}'|} dS' \right]. \quad (4.18)$$

For two-dimensional, horizontally polarized (transverse magnetic field to  $z$  or TM<sup>z</sup>) scattering from a perfect conductor, the EFIE reduces to the two-dimensional form [11]:

$$\begin{aligned} E_z^i(l) &= \frac{k\eta_0}{4} \int J_z(l') H_0^{(2)}(k|\mathbf{r}-\mathbf{r}'|) dl' \\ &= L_E[J_z(l)], \end{aligned} \quad (4.19)$$

where  $\eta_0$  is the intrinsic wave impedance of free space, and  $E_z^i(l)$  is the  $z$ -directed incident electric field at the scattering surface. In equation (4.19), the right hand side is the near-field radiation of  $J_z(l)$  and the left hand side satisfies the surface boundary condition,  $E_z^i + E_z^s = 0$ .

As a notational convenience, the integral equations (4.15) and (4.19) may be written as

$$F_z^i = L_X[J_s(l)] \quad (4.20)$$

where  $F_z^i$  is the known field quantity ( $H_z^i$  or  $E_z^i$ ) and  $X$  is the corresponding operator symbol ( $E$  or  $M$ ). The unity magnitude far-field illumination takes the form

$$F_z^i(\mathbf{r}) = e^{-j\mathbf{k}_i \cdot \mathbf{r}}, \quad (4.21)$$

where  $F$  is  $H$  (MFIE) or  $E$  (EFIE),

$$\begin{aligned} \mathbf{k}_i &= \hat{\mathbf{a}}_k \omega \sqrt{\mu\epsilon} \\ &= \omega \sqrt{\mu\epsilon} (\hat{\mathbf{a}}_x \cos \theta_g + \hat{\mathbf{a}}_y \sin \theta_g) \end{aligned} \quad (4.22)$$

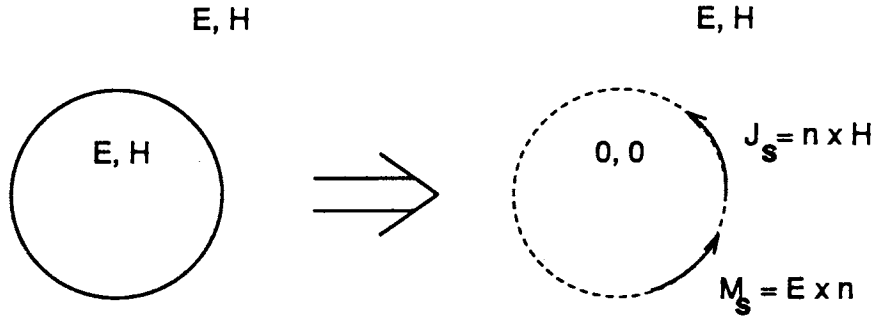


Figure 4.2: Equivalent problem to be solved with high loss dielectric scatterer.

is the vector in the direction of propagation of the illuminating field, and  $\mathbf{r} = \hat{\mathbf{a}}_x x + \hat{\mathbf{a}}_y y$  is the position vector. The far-field scatter can be found using

$$F_z^s = -L_X[J_s(l)]\Big|_{r \rightarrow \infty}. \quad (4.23)$$

### 4.3 High Dielectric-Constant, High-Loss Surfaces

When the scattering surface is perfectly conducting a true surface current exists. Thus, the moment method solves the physical scattering problem directly. When the surface is not perfectly conducting a surface current cannot be supported; the field penetrates the surface and a volume current density exists. The moment method is not well suited for direct application to volume current problems. Instead, the equivalence principle [7] is applied as shown in Figure 4.2, yielding both electric ( $J$ ) and magnetic ( $M$ ) surface current densities that radiate the desired scattered field.

The problem is further simplified by using impedance boundary conditions to relate the magnetic current density to the electric current density [33]. As illustrated in Figure 4.3, an incident plane wave is transmitted into the impedance surface at an angle of  $\theta_t$  with respect to the surface normal given by Snell's law of refraction [7]

$$\theta_t = \sin^{-1} \left( \frac{k_0}{k_1} \sin \theta_i \right). \quad (4.24)$$

Assuming that the conditions [33]

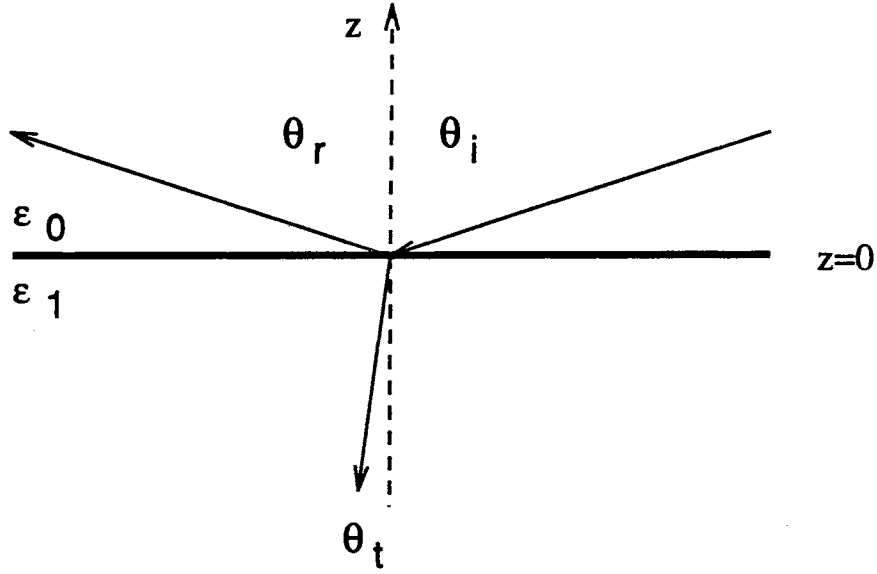


Figure 4.3: Snell's law of refraction for a dielectric surface.

$$|N| \gg 1, \quad |\text{Im}(N)k\rho_l| \gg 1 \quad (4.25)$$

where  $N = \sqrt{\epsilon_r}$  is the complex refractive index of the scattering medium and  $\rho_l$  is the radius of curvature of the surface, are met everywhere on the surface, the transmitted angle can be approximated to be zero. Hence, the field penetrating into the surface propagates as a plane wave in the negative surface normal direction.

Because the transmitted field propagates in a direction normal to the surface, approximate boundary conditions

$$\begin{aligned} E_x &= -Z_s H_y, \\ E_y &= Z_s H_x, \end{aligned} \quad (4.26)$$

where  $Z_s = \sqrt{\mu_1/\epsilon_1}$  is the surface impedance, can be used to relate the tangential  $E$  and  $H$  fields at the interface [33]. In vector form, equation (4.26) becomes [33]

$$\hat{\mathbf{n}} \times (\hat{\mathbf{n}} \times \mathbf{E}) = -Z_s \hat{\mathbf{n}} \times \mathbf{H}. \quad (4.27)$$

The two surface current components can then be related by [34]

$$\mathbf{M} = -Z_s \hat{\mathbf{n}} \times \mathbf{J}, \quad (4.28)$$

thus eliminating the need to solve for  $\mathbf{M}$  separately.

The integral equations are found by determining the near-field radiation of the electric and magnetic current densities. For vertically polarized scatter, the total scattered magnetic field is

$$H_z^s = H_z^s(J_l) + H_z^s(M_z) \quad (4.29)$$

where  $H_z^s(J_l)$  and  $H_z^s(M_z)$  are the scattered magnetic fields due to the electric and magnetic current densities, respectively. Substituting equation (4.29) into the boundary condition at the interface,

$$-H_z^i = J_l + H_z^s, \quad (4.30)$$

gives

$$-H_z^i(l) = J_l + H_z^s(J_l, l) + H_z^s(M_z, l). \quad (4.31)$$

The first two terms on the right hand side are the magnetic field integral equation  $L_M[J_l(l)]$  as defined in equation (4.15). The third term represents the near magnetic field radiation of the magnetic current density and may be found by applying duality [7] to  $L_E[J_z(l)]$  in equation (4.19). The dual is found by replacing  $E$  with  $H$ ,  $\eta_0$  with  $1/\eta_0$  and  $J$  with  $M$ , or

$$H_z^s(M_z, l) = -\frac{k}{4\eta_0} \int M_z(l') H_0^{(2)}(k|r - r'|) dl'. \quad (4.32)$$

Now substituting the impedance boundary condition of equation (4.28), equation (4.32) becomes

$$\begin{aligned} H_z^s(J_l, l) &= \frac{k}{4\eta_0} \int Z_s J_l(l') H_0^{(2)}(k|r - r'|) dl' \\ &= \frac{Z_s}{\eta_0^2} L_E[J_l(l)], \end{aligned} \quad (4.33)$$

and the two-dimensional MFIE for determining vertically polarized scattering from a lossy dielectric scatterer is then given by [35]

$$-H_z^i(l) = L_M[J_l(l)] + \frac{Z_s}{\eta_0^2} L_E[J_l(l)]. \quad (4.34)$$

The two-dimensional EFIE for finding the horizontally polarized scattering from a lossy dielectric surface is developed in a similar manner. The scattered electric field is given by

$$E_z^s = E_z^s(J_z) + E_z^s(M_l), \quad (4.35)$$

where  $E_z^s(J_z)$  and  $E_z^s(M_l)$  are the electric fields radiated by  $J$  and  $M$ , respectively. The tangential electric fields are continuous across the boundary, or

$$\begin{aligned} E_z^i &= -E_z^s \\ &= -E_z^s(J_z) - E_z^s(M_l). \end{aligned} \quad (4.36)$$

The first term on the right is given by  $L_E[J_z(l)]$  in equation (4.19), and the second term is the near-field radiation of the magnetic current density found by applying duality to  $L_M[J_l(l)]$  in equation (4.15) or

$$E_z^s(M_l, l) = 0.5M_l(l) + j\frac{k}{4} \int M_l(l')(\hat{n}' \cdot r')H_1^{(2)}(k|r - r'|) dl'. \quad (4.37)$$

Now substituting the impedance boundary condition of equation (4.28) into the dual of  $L_M[J_l(l)]$  gives

$$\begin{aligned} E_z^s(M_l, l) &= -0.5Z_s J_z(l) - j\frac{k}{4} \int Z_s J_z(l')(\hat{n}' \cdot r')H_1^{(2)}(k|r - r'|) dl' \\ &= -Z_s L_M[J_z(l)]. \end{aligned} \quad (4.38)$$

Hence, the EFIE for horizontally polarized scatter from a lossy dielectric surface is

$$E_z^i(l) = L_E[J_z(l)] + Z_s L_M[J_z(l)]. \quad (4.39)$$

Since equations (4.34) and (4.39) each include only the unknown surface current  $J$  (and not  $M$ ) they are well suited to solution using moment method techniques.

## 4.4 Low-Loss Dielectric Surfaces

For low-loss dielectric surfaces the conditions in equation (4.25) are not satisfied, and the impedance boundary condition in equation (4.28) can no longer be used to relate

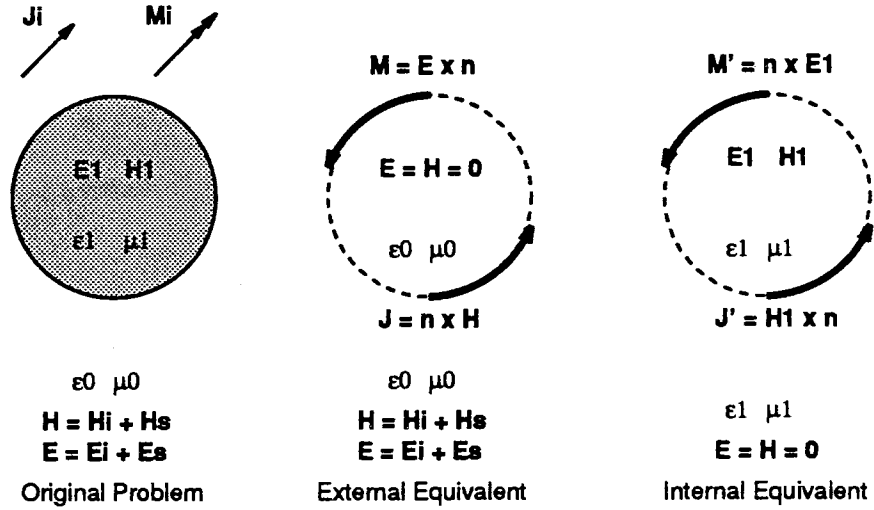


Figure 4.4: External and internal equivalent problems.

the magnetic current density to the electric current density. Instead it is necessary to solve for both currents using the moment method. The inclusion of the magnetic current density in the calculations doubles the number of unknowns in the problem. Internal and external equivalent models are used to double the number of equations so that the problem is solvable.

Following Arvas *et al.* [36], the scattering problem, shown in the left illustration of Figure 4.4, can be separated into external and internal equivalents, as shown in the middle and right illustration, respectively. External sources  $\mathbf{J}^i$  and  $\mathbf{M}^i$  in the original problem radiate in free space in the presence of an obstacle with electric parameters  $\epsilon_1$  and  $\mu_1$ . The external fields are the sum of the incident and scattered fields,

$$\begin{aligned} \mathbf{E} &= \mathbf{E}^i + \mathbf{E}^s \\ \mathbf{H} &= \mathbf{H}^i + \mathbf{H}^s, \end{aligned} \quad (4.40)$$

and the internal fields are  $\mathbf{E}^1$  and  $\mathbf{H}^1$ .

The external equivalent model is used to calculate the fields external to the dielectric boundary. Here, the obstacle is removed and replaced by surface current densities

$$\mathbf{J} = \hat{\mathbf{n}} \times \mathbf{H},$$

$$\mathbf{M} = \mathbf{E} \times \hat{\mathbf{n}}, \quad (4.41)$$

placed along the obstacle boundary. The internal electric and magnetic fields are chosen to be zero, and the total fields external to the obstacle boundary  $\mathbf{E}$  and  $\mathbf{H}$  are chosen to be the external fields of the original problem.

Likewise, the internal equivalent model is used to determine the fields transmitted into the dielectric region. In this case, the external space is replaced by the dielectric material, and surface current densities

$$\begin{aligned} \mathbf{J}' &= \mathbf{H}^1 \times \hat{\mathbf{n}}, \\ \mathbf{M}' &= \hat{\mathbf{n}} \times \mathbf{E}^1, \end{aligned} \quad (4.42)$$

are placed on the boundary of the dielectric obstacle. The exterior electric and magnetic fields are now chosen to be zero, and the interior fields are chosen to be the interior fields of the original problem,  $\mathbf{E}^1$  and  $\mathbf{H}^1$ .

The boundary conditions on the tangential electric and magnetic fields,

$$\begin{aligned} \hat{\mathbf{n}} \times \mathbf{E} - \hat{\mathbf{n}} \times \mathbf{E}^1 &= 0, \\ \hat{\mathbf{n}} \times \mathbf{H} - \hat{\mathbf{n}} \times \mathbf{H}^1 &= 0, \end{aligned} \quad (4.43)$$

must be satisfied in order to validate the external and internal equivalent models. Substituting  $-\mathbf{M} = \hat{\mathbf{n}} \times \mathbf{E}$ ,  $\mathbf{M}' = \hat{\mathbf{n}} \times \mathbf{E}^1$ ,  $\mathbf{J} = \hat{\mathbf{n}} \times \mathbf{H}$ , and  $-\mathbf{J}' = \hat{\mathbf{n}} \times \mathbf{H}^1$  into equation (4.43) leads to  $\mathbf{M}' = -\mathbf{M}$  and  $\mathbf{J}' = -\mathbf{J}$ .

The integral equations are formed using both the internal and external equivalent models. Just inside the boundary in the external equivalent model, the scattered field radiated by  $\mathbf{J}$  and  $\mathbf{M}$  must cancel out the incident field, expressed as

$$\mathbf{F}^s(\mathbf{J}, \mathbf{M})|_{tan, S^-} = -\mathbf{F}^i|_{tan}, \quad (4.44)$$

where  $F$  represents the field component (either  $E$  or  $H$ ),  $tan$  indicates the tangential components,  $S^-$  indicates a surface just inside the boundary, and  $ext$  refers to the use

of the *external* electrical parameters. In the internal equivalent model, the scattered fields radiated by  $\mathbf{J}' = -\mathbf{J}$  and  $\mathbf{M}' = -\mathbf{M}$  must be zero outside of the boundary. This relationship is represented by

$$\mathbf{F}^s(\mathbf{J}', \mathbf{M}')|_{tan, S^+}^{int} = \mathbf{F}^s(-\mathbf{J}, -\mathbf{M})|_{tan, S^+}^{int} = 0, \quad (4.45)$$

where  $S^+$  indicates a surface just outside the boundary and *int* refers to the use of the *internal* electrical parameters. Adding equations (4.44) and (4.45) gives a system of linear equations

$$\mathbf{F}^s(\mathbf{J}, \mathbf{M})|_{tan, S^-}^{ext} + \mathbf{F}^s(-\mathbf{J}, -\mathbf{M})|_{tan, S^+}^{int} = -\mathbf{F}^i|_{tan}, \quad (4.46)$$

that can be solved for  $\mathbf{J}$  and  $\mathbf{M}$  using the moment method as before.

The matrix form of equation (4.46) for horizontal polarization can be expressed as

$$\begin{bmatrix} L_E^{ext} & L_M^{ext'} \\ L_E^{int} & L_M^{int'} \end{bmatrix} \begin{bmatrix} J \\ M \end{bmatrix} = \begin{bmatrix} -E^i \\ 0 \end{bmatrix}. \quad (4.47)$$

Here  $L_E^{ext}$  is the EFIE  $L_E$  for finding the near electric field contribution by  $J$ , and  $L_M^{ext'}$  is the dual of the MFIE  $L_M$  for finding the near electric field contribution by  $M$  in the external equivalent model. Both  $L_E^{ext}$  and  $L_M^{ext'}$  use the electrical parameters  $\epsilon_0$ ,  $\mu_0$ , and  $k_0$  of the external medium. Likewise,  $L_E^{int}$  gives the near electric field contribution by  $J$ , and  $L_M^{int'}$  gives the near electric field contribution by  $M$  in the internal equivalent model. Here,  $L_E^{int}$  is the EFIE  $L_E$ , and  $L_M^{int'}$  is the dual of the MFIE  $L_M$ , both using the internal electrical parameters  $\epsilon_1$ ,  $\mu_1$ , and  $k_1$ . Evaluating the matrix equation yields

$$\begin{aligned} L_E^{ext}[J] + L_M^{ext'}[M] &= -E^i \\ L_E^{int}[J] + L_M^{int'}[M] &= 0, \end{aligned} \quad (4.48)$$

where the top equation is for the external equivalent, and the bottom equation is for the internal equivalent. The right hand side of each equation represents the incident field for the external (top) and internal (bottom) equivalent models.



The matrix equation for vertical polarization

$$\begin{bmatrix} L_E^{ext'} & L_M^{ext} \\ L_E^{int'} & L_M^{int} \end{bmatrix} \begin{bmatrix} M \\ J \end{bmatrix} = \begin{bmatrix} -H^i \\ 0 \end{bmatrix}, \quad (4.49)$$

is found by applying duality to equation (4.47). Here,  $L_E^{ext'}$  and  $L_E^{int'}$  are the duals of the EFIE  $L_E$  using external and internal electrical parameters, respectively.  $L_M^{ext}$  and  $L_M^{int}$  are the MFIE  $L_M$  also using the external and internal electrical parameters, respectively. Evaluating this matrix equation gives

$$\begin{aligned} L_E^{ext'}[M] + L_M^{ext}[J] &= -H^i \\ L_E^{int'}[M] + L_M^{int}[J] &= 0, \end{aligned} \quad (4.50)$$

again where the top equation is for the external equivalent model, and the bottom equation is for the internal equivalent model.

## 4.5 Scattering by a Circular Cylinder

As an example, the moment method is used to solve for the scattering from infinitely long, circular cylinders with complex permittivity  $\epsilon_1$ , complex permeability  $\mu_1$ , and a radius  $a = 1.0\lambda$ , as shown in Figure 4.5. The illuminating uniform plane wave is perpendicular to the axis of the cylinder, and the far-field scatter is observed at an angle  $\phi'$  as shown in the diagram.

The vertical (VV) and horizontal (HH) bistatic scattering width (scattering cross section per unit length) in the exact analytical solution are given by [37]

$$\begin{aligned} \sigma_{VV}(\phi') &= \frac{4}{k_0} |T_{VV}(\phi')|^2, \\ \sigma_{HH}(\phi') &= \frac{4}{k_0} |T_{HH}(\phi')|^2, \end{aligned} \quad (4.51)$$

respectively, where

$$T_{VV}(\phi') = \sum_{n=0}^{\infty} (-1)^n \epsilon_n A_n \cos n\phi',$$

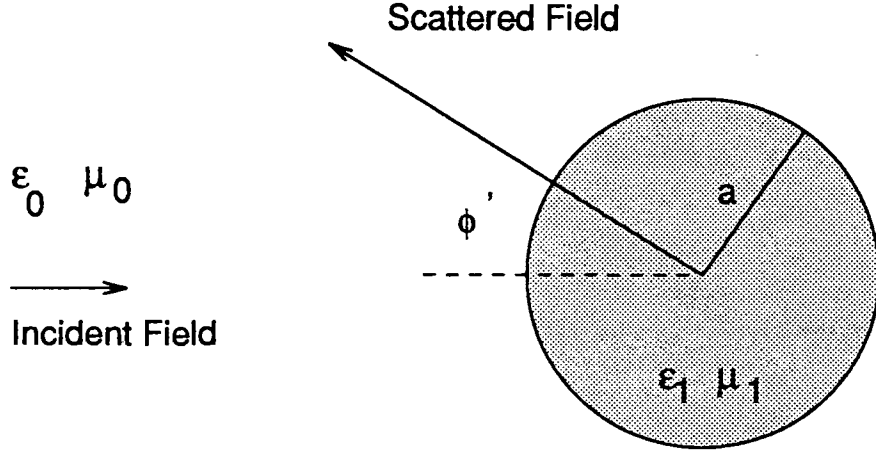


Figure 4.5: Scattering geometry for lossy dielectric cylinder.

$$T_{HH}(\phi') = \sum_{n=0}^{\infty} (-1)^n \epsilon_n B_n \cos n\phi'. \quad (4.52)$$

The coefficients  $A_n$  and  $B_n$  are given by

$$A_n = -\frac{(k_1/\mu_1)J'_n(k_1a) - (k_0/\mu_0)J'_n(k_0a)J_n(k_1a)}{(k_1/\mu_1)H_n^{(1)}(k_0a)J'_n(k_1a) - (k_0/\mu_0)H_n'^{(1)}(k_0a)J_n(k_1a)},$$

$$B_n = -\frac{(k_1/\epsilon_1)J'_n(k_1a) - (k_0/\epsilon_0)J'_n(k_0a)J_n(k_1a)}{(k_1/\epsilon_1)H_n^{(1)}(k_0a)J'_n(k_1a) - (k_0/\epsilon_0)H_n'^{(1)}(k_0a)J_n(k_1a)}, \quad (4.53)$$

where  $k_0 = \omega\sqrt{\mu_0\epsilon_0}$  and  $k_1 = \omega\sqrt{\mu_1\epsilon_1}$  are the wave numbers in free space and the complex wave number in the lossy dielectric, respectively, and

$$\epsilon_n = \begin{cases} 1 & n = 0 \\ 2 & n = 1, 2, \dots \end{cases}. \quad (4.54)$$

Note that the conductivity of the cylinder material is accounted for by the complex permittivity and permeability.

The radar scattering width was found for four cylinder configurations at both vertical and horizontal polarizations using the moment method with pulse basis function widths of  $\Delta L = 0.1\lambda$  and  $\Delta L = 0.05\lambda$ . The first configuration provided a reference for perfectly conducting cylinders, while the other three configurations represented soil cylinders at varying degrees of moisture content. At a frequency of 1.8 GHz, the

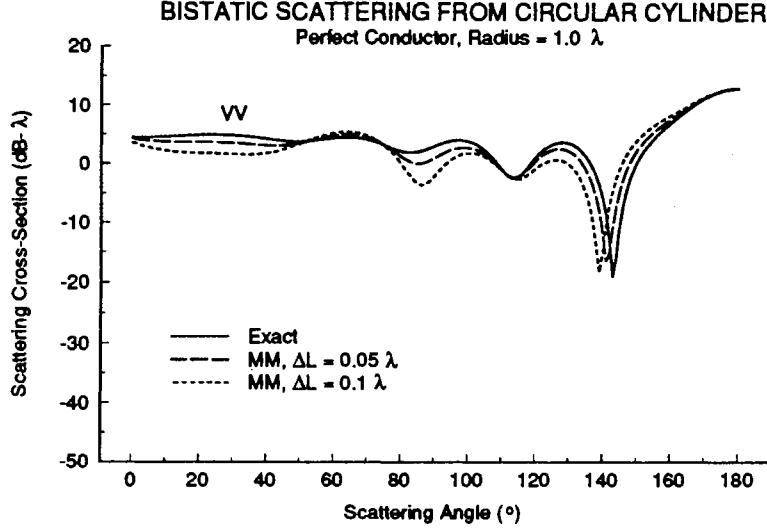


Figure 4.6: Scattering from a perfectly conducting cylinder, vertical polarization.

complex dielectric constant of soil can range from approximately  $\epsilon_r = 3 - j0$  (for dry soil and sand) to  $\epsilon_r = 35 - j5$  (for moist clay) [15]. For these tests, the dielectric constants were chosen to be  $\epsilon_r = 3 - j0$ ,  $\epsilon_r = 10 - j2$ , and  $\epsilon_r = 35 - j5$ , which correspond to volumetric moisture contents of approximately 0, 0.2, and 0.5  $g/cm^3$ , respectively [15].

The vertical polarization results for perfect conductors,  $\epsilon_r = 3 - j0$ ,  $\epsilon_r = 10j - 2$ , and  $\epsilon_r = 35 - j5$  are shown in Figures 4.6, 4.7, 4.8, and 4.9, respectively. The corresponding horizontal polarization results are given in Figures 4.10, 4.11, 4.12, and 4.13.

In each of these figures, the exact analytical solution is compared to the moment method solution using pulse basis function widths of  $\Delta L = 0.1\lambda$  and  $\Delta L = 0.05\lambda$ . The smaller basis functions model the current more accurately, thus giving better far-field scatter predictions. Figures 4.7 and 4.11 also demonstrate the inaccuracy of using the moment method with impedance boundary conditions (IBC) for the lossless dielectric

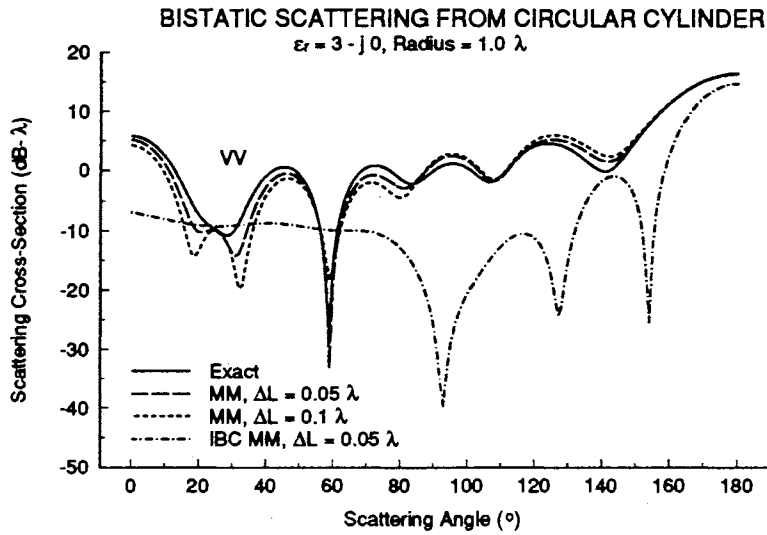


Figure 4.7: Scattering from a dielectric cylinder  $\epsilon_r = 3 - j0$ , vertical polarization.

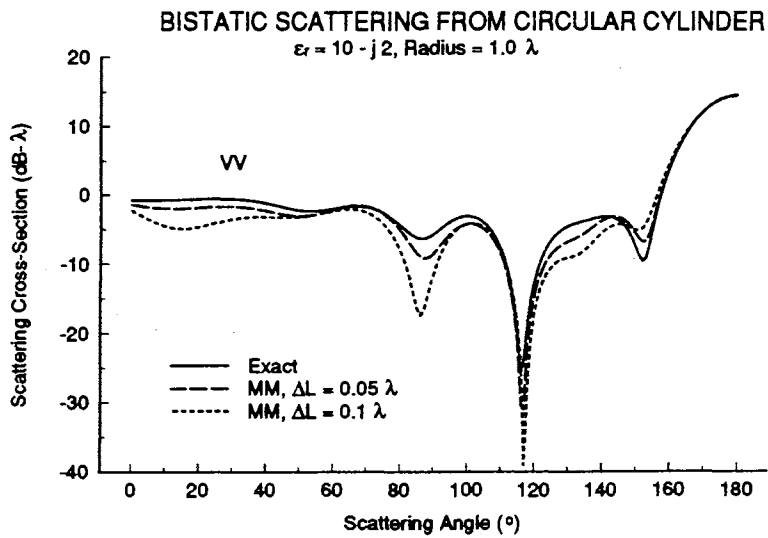


Figure 4.8: Scattering from a dielectric cylinder  $\epsilon_r = 10 - j2$ , vertical polarization.

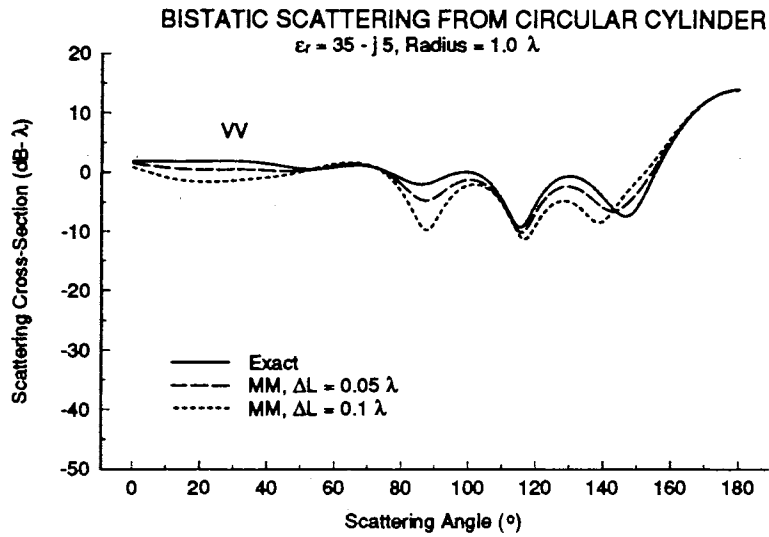


Figure 4.9: Scattering from a dielectric cylinder  $\epsilon_r = 35 - j5$ , vertical polarization.

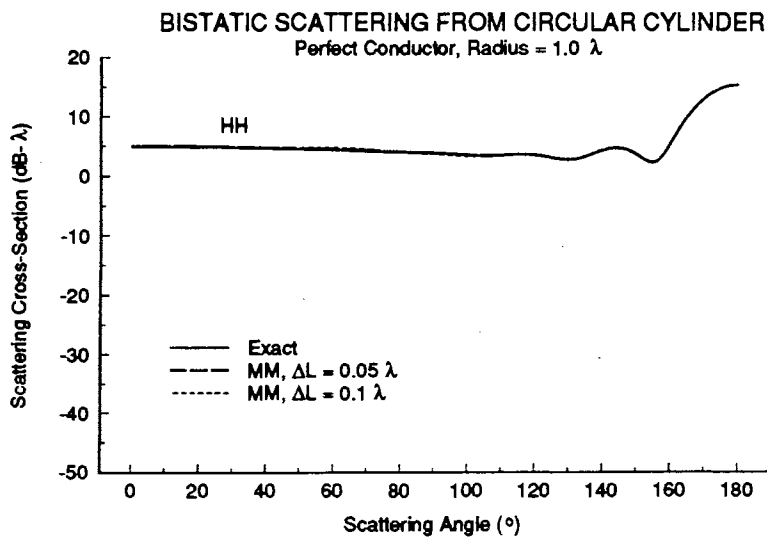


Figure 4.10: Scattering from a perfectly conducting cylinder, horizontal polarization.

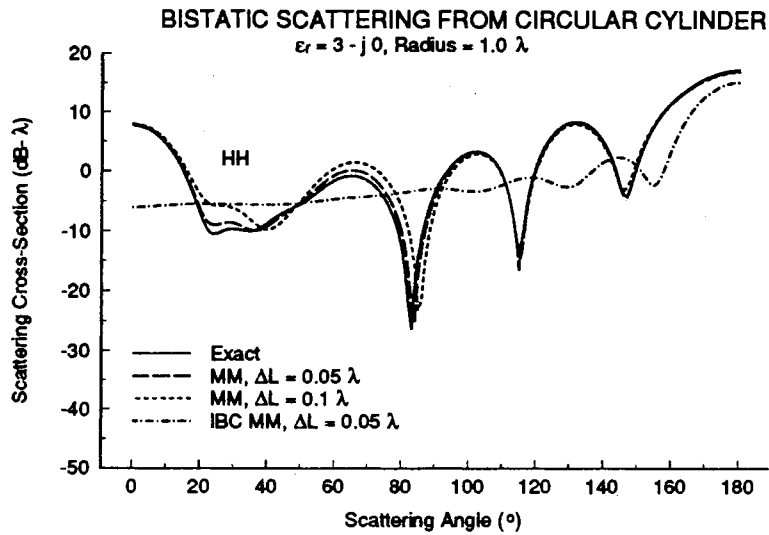


Figure 4.11: Scattering from a dielectric cylinder  $\epsilon_r = 3 - j0$ , horizontal polarization.

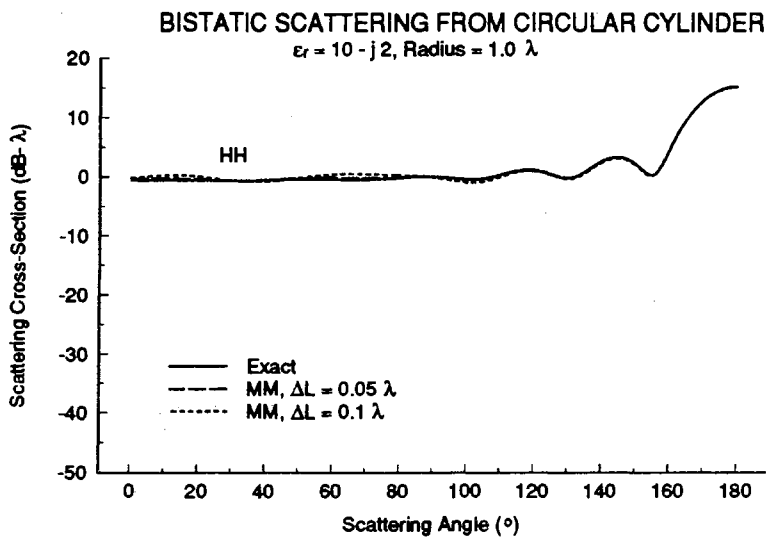


Figure 4.12: Scattering from a dielectric cylinder  $\epsilon_r = 10 - j2$ , horizontal polarization.

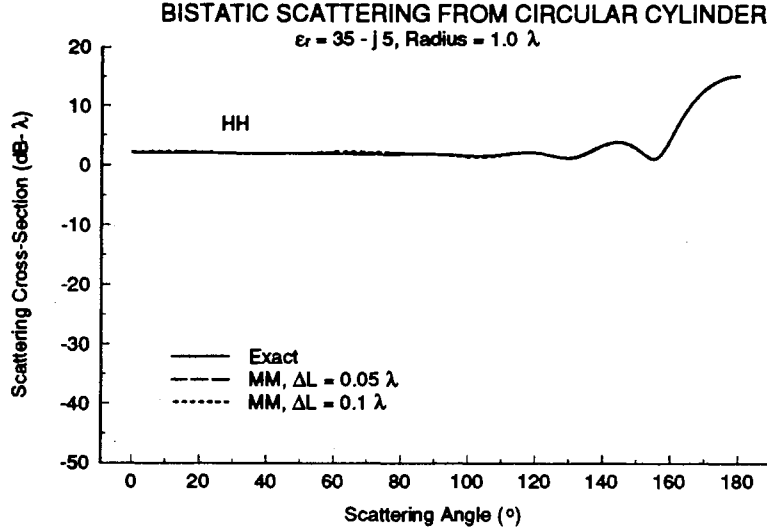


Figure 4.13: Scattering from a dielectric cylinder  $\epsilon_r = 35 - j5$ , horizontal polarization.

case  $\epsilon_r = 3 - j0$ , since the impedance boundary conditions in equation (4.28) are not satisfied for this dielectric constant.

Of most interest is the ability of the moment method solution to predict the locations and magnitudes of the relative maximums and the locations of the nulls in the scatter. Tables 4.1 and 4.2 give the average absolute magnitude errors for the scatter cross-section and the locations of the relative maximums and nulls, respectively, for horizontal and vertical polarizations. When the pulse basis function width is  $\Delta L = 0.1\lambda$ , the moment method code predicts the magnitudes of the relative maximums to within an average of 1.6 dB for VV and 0.4 dB for HH polarization. The angular locations for these relative maximums are predicted within approximately  $2^\circ$ . Using a smaller pulse basis function  $\Delta L = 0.05\lambda$  decreases the average magnitude errors to approximately 0.83 dB and 0.18 dB for vertical and horizontal polarizations, respectively, and the average relative maximum angular placement to within  $1^\circ$ . The null locations are predicted to within an average of  $2.5^\circ$  for  $\Delta L = 0.1\lambda$  and  $1.5^\circ$  for  $\Delta L = 0.05\lambda$ . Also

Table 4.1: Average Magnitude Errors (dB) for Circular Cylinder Scattering.

	$\Delta L = 0.1\lambda$	$\Delta L = 0.05\lambda$
VV Relative Maximum	1.5079	0.8298
VV 0°	1.2443	0.4651
VV 90°	4.8168	2.1944
VV 180°	0.1370	0.05418
HH Relative Maximum	0.3872	0.1843
HH 0°	0.2573	0.1481
HH 90°	0.7748	0.2326
HH 180°	0.1147	0.04717

Table 4.2: Average Angular Placement Errors (°) for Circular Cylinder Scattering.

	$\Delta L = 0.1\lambda$	$\Delta L = 0.05\lambda$
VV Relative Maximums	2.1	1.0
HH Relative Maximums	1.8	0.9
VV Nulls	2.5	1.5
HH Nulls	2.0	1.0

given in Table 4.1 are the scatter cross-section predictions for three scattering angles of interest, 0°, 90°, and 180°. The largest errors occurred at vertical polarization for 90°, where the moment method solutions were in error by an average of 4.8 dB for  $\Delta L = 0.1\lambda$  and 2.2 dB for  $\Delta L = 0.05\lambda$ .

## 4.6 Limitations

Since the induced current on the scattering surface must be divided into small segments, finite computer resources may prevent electrically large surfaces from being completely modeled using the moment method. Instead, the numerically modeled surface must be truncated on each side, causing the technique to incorrectly predict the surface current at these unrealistic edges. When the erroneous surface current density is radiated, it affects not only the far-field scatter but also changes the illumination of



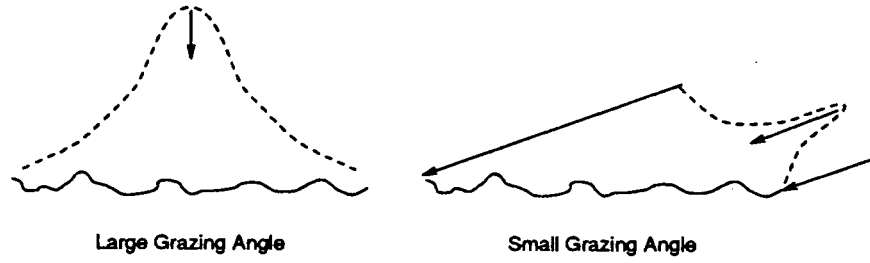


Figure 4.14: Effects of illumination angle on the Thorsos weighting function.

the modeled surface segments, which can further degrade the accuracy of the far-field scatter.

To avoid the edge effect problems, the illuminating field of equation (4.21) can be altered so that its magnitude is negligible at the edges. Thorsos [26] gives an electromagnetically valid tapered field

$$\begin{aligned}
 F^i(\mathbf{r}) &= \exp \left\{ j\mathbf{k}_i \cdot \mathbf{r} [1 + w(r)] - (x - z \cot \theta_g)^2 / g^2 \right\} \\
 |F^i| &= \exp \left[ -(x - y \cot \theta_g)^2 / g^2 \right]
 \end{aligned} \tag{4.55}$$

where  $g$  is a tapering parameter and

$$w(r) = \frac{2(x - y \cot \theta_g)^2 / g^2 - 1}{(kg \sin \theta_g)^2}. \tag{4.56}$$

Equation (4.55) satisfies the wave equation when  $k_i g \sin \theta_g \gg 1$ . Thorsos also gives another, more complicated weighting function that remains valid to a lower grazing angle.

As shown in Figure 4.14, the illumination angle can greatly affect the illumination pattern of the Thorsos weighting function. For large grazing angles, a large portion of the surface is illuminated, and the illumination tapers off slowly to an insignificant value at the surface edges. When the illumination angle approaches grazing, the tapered field becomes a narrow beam that does not resemble realistic illumination. Only a small portion of the surface receives strong illumination, and the length of the surface model must be increased accordingly.

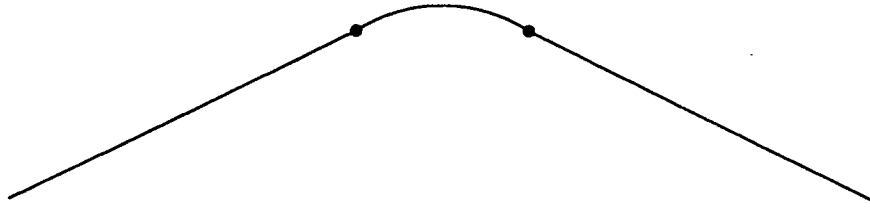


Figure 4.15: Rounded wedge scattering geometry.

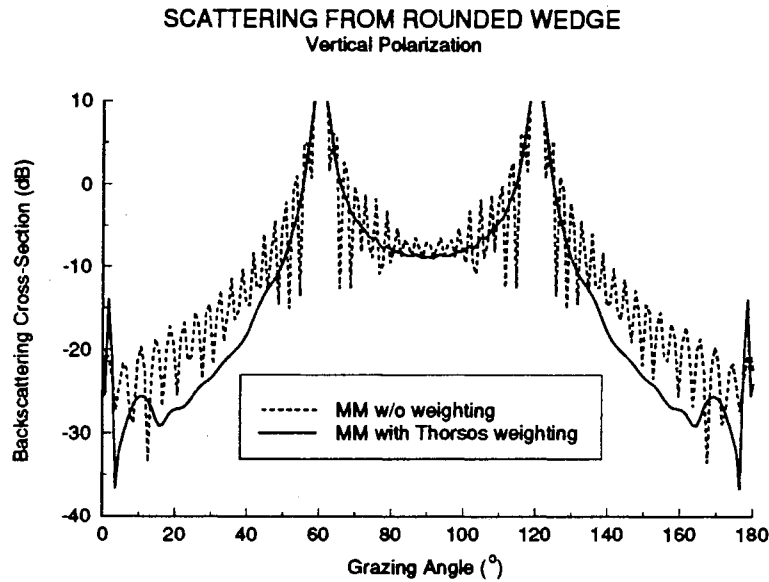


Figure 4.16: Effects of illumination weighting function, vertical polarization.

The detrimental effects of the artificial surfaces edges on the MM solution can be seen in the MM analysis of scattering from a perfectly conducting wedge with a rounded apex, as shown in Figure 4.15. The radius of curvature of the apex is  $0.5\lambda$ , the interior angle of the wedge is  $120^\circ$ , and the extensions are  $10\lambda$  long. Figures 4.16 and 4.17 compare the backscattering cross-sections predicted by the MM with and without weighting functions for vertical and horizontal polarizations, respectively. When the illuminating field is not tapered, the truncated surface causes the MM to predict edge diffraction, which incorrectly illuminates the scattering surface and propagates to the far-field region. The Thorsos weighting function significantly reduces the edge effects at moderate grazing angles, but significant edge effects are still seen for smaller

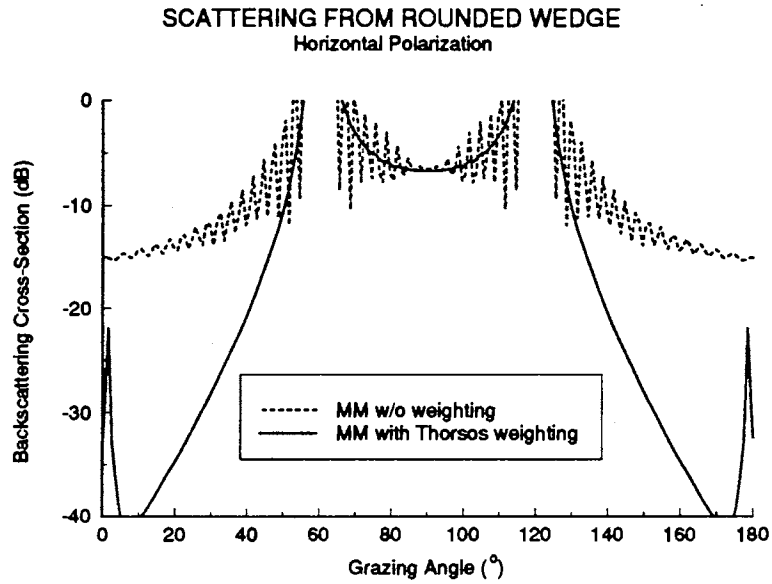


Figure 4.17: Effects of illumination weighting function, horizontal polarization.

grazing angles. The singularities at  $60^\circ$  and  $120^\circ$  in the plots are due to the specular reflections from the front and back extensions.

## Chapter 5

# HYBRID MM/GTD TECHNIQUE

The scattering calculations are performed using adaptations of Burnside's hybrid MM/GTD technique [12], which allows for certain classes of infinite surfaces to be modeled without the truncation normally associated with the standard moment method. Instead of truncating the current, the hybrid technique predicts the form of the current on infinite extensions of portions of the surface using the geometrical theory of diffraction (GTD) and calculates the rest of the current using the standard moment method. Burnside's original technique only applies to perfectly conducting surfaces. For impedance and low-loss dielectric boundaries, the equations in the hybrid technique must be adapted to account for volume current densities.

Much of the discussion in this chapter is based upon West's implementation of the hybrid technique for an arbitrary, perfectly-conducting rough surface, as shown in Figure 5.1. West's code served as the foundation for two further adaptations by West and Sturm – one for impedance (lossy dielectric) surfaces representative of moist soil and water [38] and another for low-loss dielectric surfaces representative of dry soil and sand at microwave frequencies.

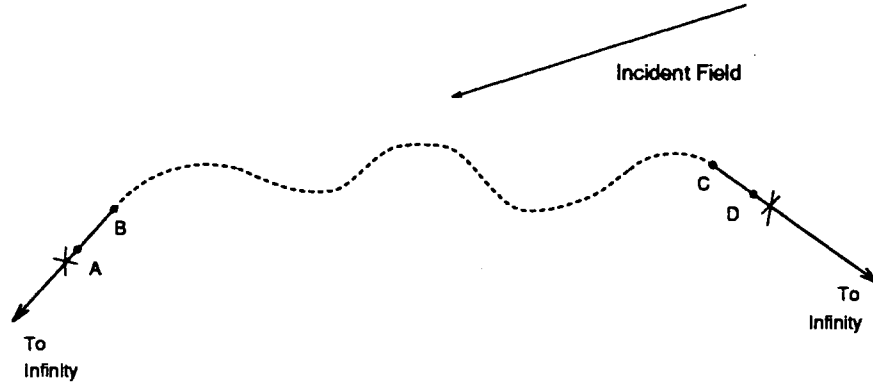


Figure 5.1: Arbitrary scattering surface.

## 5.1 Perfectly Conducting Surfaces

The dashed section of the surface in Figure 5.1 represents the actual, perfectly conducting rough surface while the solid line represents infinitely long, planar extensions. The extensions are chosen such that all points on the actual surface are shadowed from all points on the extension (except of course at the intersection points B and C). Because the surface is arbitrary, little is known initially about the current between points A and D. Thus, the current in this region is described using standard MM pulse basis functions with impulse testing functions (yielding point matching) centered on the basis functions.

Since the extensions are shadowed from the arbitrary surface points, the fields at the surface of the extensions can be entirely described as the sum of a field diffracted from point B or C plus the geometrical optical (GO) incident and reflected fields:

$$\mathbf{F}^t = \mathbf{F}^i + \mathbf{F}^s = \mathbf{F}^{\text{GO}} + \mathbf{F}^d, \quad (5.1)$$

where  $\mathbf{F}^t$  is the total field,  $\mathbf{F}^i$  is the incident field,  $\mathbf{F}^s$  is the scattered field,  $\mathbf{F}^{\text{GO}}$  is the geometrical optics incident and reflected fields, and  $\mathbf{F}^d$  is the diffracted field. The current on the extension is obtained by applying the surface boundary conditions to equation (5.1), yielding the physical optics current associated with the GO fields plus an additional current component associated with the diffracted field (the “diffraction-

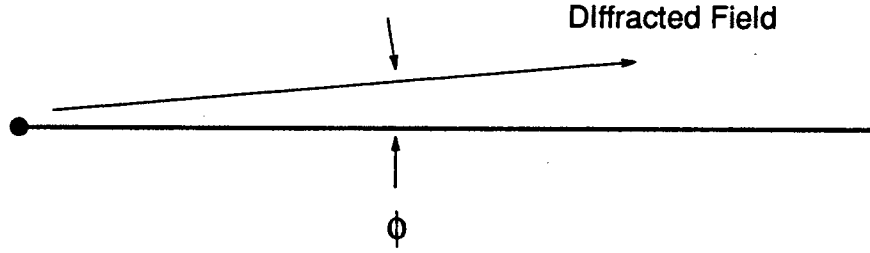


Figure 5.2: Diffracted field in the vicinity of the extensions.

field current”):

$$\mathbf{J}_s = \mathbf{J}_{PO} + \mathbf{J}_d. \quad (5.2)$$

Since the extension is flat and perfectly conducting, the PO current is known exactly *a priori*. (Note that if the extension is shadowed from the incident field the PO current is simply zero). However, the diffracted field, and therefore the diffraction-field current, is not known initially and must be determined using the moment method. Since it extends to infinity, use of ordinary sub-domain MM basis functions to describe this current would lead to an infinite order system of linear equations that cannot be solved. Instead it is recognized that at distances far enough away from the diffraction point the diffracted field is ray optical. Thus, the form of the diffracted field at the extension beyond points A or D is given by

$$\mathbf{F}^d(r) = \hat{\mathbf{a}}_z F_0 \frac{e^{-jkr}}{\sqrt{r}} f(\phi), \quad (5.3)$$

where  $r$  is the distance from the diffraction point,  $F_0$  is the magnitude of the incident field,  $\hat{\mathbf{a}}_z$  is the unit vector out of the page, and  $f(\phi)$  is an arbitrary function of the angular cylindrical coordinate with the diffraction point as the origin, as shown in Figure 5.2. Applying the surface boundary condition  $\mathbf{J}_s = \hat{\mathbf{n}} \times \mathbf{H}$  yields the diffraction currents

$$\mathbf{J}_d(r) = \begin{cases} \hat{\mathbf{a}}_1 J_0 \frac{e^{-jkr}}{\sqrt{r}} & \text{(vertical polarization)} \\ \hat{\mathbf{a}}_z J_0 \frac{e^{-jkr}}{r^{1.5}} & \text{(horizontal polarization)} \end{cases}, \quad (5.4)$$

where  $\hat{\mathbf{a}}_1$  is a unit vector in the direction tangential to the surface and  $J_0$  is an unknown weighting coefficient. We now see that a single basis function of the form of

equation (5.4) can be used to include the diffraction current from the diffraction point to infinity in the hybrid numerical technique. An additional match point is added for the diffraction current on each extension, as indicated as an X to the left of point A and to the right of point D in Figure 5.1, bringing the total number of match points to  $N + 2$ . This, combined with the known physical optics currents, entirely describes the current on the infinite extensions. Since there are no discontinuities on the modeled surface, no artificial edge effects are introduced.

It should be noted that the forms of the diffraction-field current in equation (5.4) are not valid when the shadow boundary is along the extension. However, in section 5.5 it will be shown that errors in the current when the illumination grazes the extension do not significantly affect the far-field scattering. The removal of the artificial edge diffraction appears to be the most important purpose of the GTD basis function.

The current on the entire surface may now be written as

$$\mathbf{J}_s = \mathbf{J}_{MM} + \mathbf{J}_d + \mathbf{J}_{PO}, \quad (5.5)$$

where  $\mathbf{J}_{MM}$  is the current between points A and D described by ordinary MM pulse basis functions:

$$\begin{aligned} \mathbf{J}_{MM}(l) &= \hat{\mathbf{a}}_1 \sum_{m=1}^N \alpha_m P(l - l_m), & \text{(vertical polarization)} \\ &= \hat{\mathbf{a}}_z \sum_{m=1}^N \alpha_m P(l - l_m), & \text{(horizontal polarization),} \end{aligned} \quad (5.6)$$

where  $P(l - l_m)$  is a pulse function centered at  $l_m$  and  $\alpha_m$  are unknown weighting coefficients to be found via the moment method. The diffraction current for vertical polarization is

$$\mathbf{J}_d(l) = \begin{cases} \hat{\mathbf{a}}_1 \alpha_{N+1} \frac{e^{-jkr}}{\sqrt{r}} & l < A \\ \hat{\mathbf{a}}_1 \alpha_{N+2} \frac{e^{-jkr}}{\sqrt{r}} & l > D \end{cases}, \quad (5.7)$$

and for horizontal polarization is

$$\mathbf{J}_d(l) = \begin{cases} \hat{\mathbf{a}}_z \alpha_{N+1} \frac{e^{-jkr}}{r^{1.5}} & l < A \\ \hat{\mathbf{a}}_z \alpha_{N+2} \frac{e^{-jkr}}{r^{1.5}} & l > D \end{cases}, \quad (5.8)$$

where  $l$  is the arc length along the surface as shown in Figure 5.1, and  $r$  is the distance along the extension from the diffraction point to the source point. The physical optics current  $\mathbf{J}_{PO}$  on the front and back faces is given by

$$\mathbf{J}_{PO}(l) = \begin{cases} 2\hat{\mathbf{n}} \times \mathbf{H}^i & l < A, l > D \\ 0 & \text{elsewhere} \end{cases}. \quad (5.9)$$

Substituting equation (5.5) into equation (4.20) gives

$$F^i = L_X[J_{MM} + J_d + J_{PO}]. \quad (5.10)$$

Because the  $J_{PO}$  is entirely known *a priori* and  $L_X[\ ]$  is a linear operator, the physical optics term may be moved to the left hand side, giving

$$F^i - L_X[J_{PO}] = L_X[J_{MM}] + L_X[J_d]. \quad (5.11)$$

Thus, the physical optics current simply appears as a field source term in the hybrid technique. Evaluating equation (5.11) at the centers of the basis functions (point matching or collocation), plus at two additional points on the extensions yields  $N + 2$  algebraically linear equations with  $N + 2$  unknowns. Solving this system yields the moment weighting coefficients  $\alpha_m$ , completing the MM solution of the current. The far field scatter is then determined from

$$F^s = -L_X[J_{MM} + J_d + J_{PO}] \Big|_{r \rightarrow \infty}. \quad (5.12)$$

## 5.2 High Dielectric-Constant, High-Loss Surfaces

The hybrid MM/GTD technique can be extended to apply to equations (4.34) and (4.39) to find the scattering from lossy dielectric surfaces of the type shown in Figure



5.1 with little modification. The surface current between points A and D is again divided into pulse basis functions as described in equation (5.6), and the diffraction-current basis functions are unchanged from equation (5.4) since the diffracted field is still ray optical at suitable distances from the diffraction point [39]. The physical optics current needs to be modified slightly since the surface is no longer perfectly conducting:

$$\mathbf{J}_{PO}(l) = \begin{cases} (1 - \Gamma)\hat{\mathbf{n}} \times \mathbf{H}^i & l < A, l > D \\ 0 & \text{elsewhere} \end{cases}, \quad (5.13)$$

where  $\Gamma$  is the appropriate parallel (vertical) polarized or perpendicular (horizontal) polarized reflection coefficient on the front and back extensions. (Note that equation (5.13) reduces to (5.9) with a perfectly conducting surface.) Substituting equation (5.5) (with the modified  $J_{PO}$ ) into equation (4.34) and moving the known terms to the left hand (source) side yields

$$\begin{aligned} -H^i(l) - L_M[J_{PO}(l)] - \frac{Z_s}{\eta_0^2} L_E[J_{PO}(l)] \\ = L_M[J_{MM}(l) + J_d(l)] + \frac{Z_s}{\eta_0^2} L_E[J_{MM}(l) + J_d(l)]. \end{aligned} \quad (5.14)$$

Similarly, the EFIE becomes

$$\begin{aligned} E^i(l) - L_E[J_{PO}(l)] - Z_s L_M[J_{PO}(l)] \\ = L_E[J_{MM}(l) + J_d(l)] + Z_s L_M[J_{MM}(l) + J_d(l)]. \end{aligned} \quad (5.15)$$

The GTD basis functions from equation (5.4) are used here to model the interactions between the diffraction current on the extensions and the current segments in the moment method region. Since the propagation constant  $k$  is different in each media, these GTD basis functions do not meet the boundary conditions on the impedance surface and therefore are not truly valid. However, tests show that the exact current is not needed to achieve acceptable results. Again, the main effect of the diffraction

current is to eliminate the artificial edge effects that can greatly affect the illumination and far-field backscatter.

Both equations (5.14) and (5.15) can be evaluated at the  $N+2$  matching points, and the resulting linear system algebraic equations solved to give the unknown coefficients  $\alpha_n$ , completing the numerical solution. The far-field scattering from the surface is then found by evaluating

$$E^s = -L_E[J_{MM} + J_d + J_{PO}] \Big|_{r \rightarrow \infty} - Z_s L_M[J_{MM} + J_d + J_{PO}] \Big|_{r \rightarrow \infty} \quad (5.16)$$

or

$$H^s = L_M[J_{MM} + J_d + J_{PO}] \Big|_{r \rightarrow \infty} + \frac{Z_s}{\eta_0^2} L_E[J_{MM} + J_d + J_{PO}] \Big|_{r \rightarrow \infty}. \quad (5.17)$$

### 5.3 Low-loss Dielectric Surfaces

The integral equations for the low-loss dielectric case can be applied to the hybrid MM/GTD technique by adding the contributions of the known physical optics currents and the unknown diffracted-field currents on the extensions. The physical optics electric and magnetic currents are given by

$$\mathbf{J}_{PO}(l) = \begin{cases} (1 - \Gamma) \hat{\mathbf{n}} \times \mathbf{H}^i & l < A, l > D \\ 0 & \text{elsewhere} \end{cases} \quad (5.18)$$

and

$$\mathbf{M}_{PO}(l) = \begin{cases} (1 + \Gamma) \mathbf{E}^i \times \hat{\mathbf{n}} & l < A, l > D \\ 0 & \text{elsewhere} \end{cases}, \quad (5.19)$$

where  $\Gamma$  is the appropriate parallel (vertical) polarized or perpendicular (horizontal) polarized reflection coefficient on the front and back extensions. The near-field radiation of these currents are added to the source terms in the right hand side of equations (4.48) and (4.50), as

$$L_E^{ext}[J] + L_M^{ext'}[M] = -E^i - L_E^{ext}[J_{PO}] - L_M^{ext'}[M_{PO}]$$

$$L_E^{int}[J] + L_M^{int'}[M] = -L_E^{int}[J_{PO}] - L_M^{int'}[M_{PO}]. \quad (5.20)$$

and

$$\begin{aligned} L_E^{ext'}[M] + L_M^{ext}[J] &= -H^i - L_E^{ext'}[M_{PO}] - L_M^{ext}[J_{PO}] \\ L_E^{int'}[M] + L_M^{int}[J] &= -L_E^{int'}[M_{PO}] - L_M^{int}[J_{PO}]. \end{aligned} \quad (5.21)$$

As noted in the previous section for high-loss dielectric surfaces, the GTD basis functions from equation (5.4) are used for modeling the interaction between the diffraction current on the extensions and the moment method current segments, even though it is known that these basis functions do not meet the boundary conditions because of the difference in the propagation constant  $k$  in each medium. Again, the GTD current merely eliminates the adverse effects of artificially truncating the surface current.

Once the system of equations is solved for the unknown coefficients for the electric and magnetic current densities on the moment method segments and the unknown diffraction-current coefficients on the extension, the far-field scattering from the surface is found by evaluating

$$\begin{aligned} E^s &= L_E^{ext}[J_{MM} + J_d + J_{PO}] \Big|_{r \rightarrow \infty} + L_M^{ext'}[M_{MM} + M_d + M_{PO}] \Big|_{r \rightarrow \infty}, \\ H^s &= L_E^{ext'}[M_{MM} + M_d + M_{PO}] \Big|_{r \rightarrow \infty} + L_M^{ext}[J_{MM} + J_d + J_{PO}] \Big|_{r \rightarrow \infty}. \end{aligned} \quad (5.22)$$

## 5.4 Implementation Considerations

West [10] implemented the hybrid MM/GTD technique for perfectly conducting surfaces, and West and Sturm [38] implemented adaptations for both high-loss and low-loss dielectric surfaces. The C++ code was developed and tested using Pentium-based personal computers running the Linux 1.2.13 operating system and the GNU G++/GCC compiler (version 2.7). Sixteen IBM RS/6000 320H workstations running the AIX 3.2 operating system were used extensively for the application of the code to

arbitrary scattering problems. Some of the C++ code utilizes numerical algorithms taken from the Meschach [40] and Amos [41] libraries, and the epsilon convergence-acceleration algorithm [42] [43] was implemented by O’Leary [44].

This section describes implementation details for the hybrid MM/GTD technique for each surface configuration – perfectly conducting, high-loss, and low-loss dielectric. The section’s organization follows the steps taken by the code in the solution process. First, the terms in the linear system of equations must be evaluated. This is done by calculating the source terms (the incident field and the near-field radiation of the physical optics current) and the MM interaction matrix (near-field radiation of the MM and diffraction-current basis functions). Next, the linear system is solved using LU decomposition and back substitution. Finally, the far-field radiation of the currents gives the total scattered field.

### 5.4.1 Evaluation of the Linear System

For a given incident angle, the source vector in the linear system of equations must be calculated. Each component of this vector is the summation of the incident field and near-field radiation of the known physical optics current,  $L_X[J_{PO}]$ , evaluated at the center of the corresponding surface segment. The calculation of the incident field is a simple evaluation of a complex exponential term,

$$F^i = \exp(-j\mathbf{k} \cdot \mathbf{r}) = \exp[-jk_0(x_o \cos \theta_g + y_o \sin \theta_g)], \quad (5.23)$$

where  $(x_o, y_o)$  is the observation point on the surface.

The evaluations of  $L_M[J_{PO}]$  in equation (4.15) and  $L_E[J_{PO}]$  in equation (4.19) are much more computationally expensive. These integrals find the electric and magnetic fields, respectively, at the surface segment contributed by the infinitely extending physical optics current. The infinite integrations of the rapidly oscillating and slowly decaying integrands converge quite slowly. Convergence can be dramatically increased

by evaluating the integrals as infinite series and applying the epsilon convergence-acceleration algorithm [42] [43].

The infinite integrations

$$L_M[J_{PO}(l)] = 0.5J_{PO}(l) + j\frac{k}{4} \int J_{PO}(l')(\hat{\mathbf{n}}' \cdot \mathbf{r}')H_1^{(2)}(k|r-r'|) dl', \quad (5.24)$$

and

$$L_E[J_{PO}(l)] = \frac{k\eta_0}{4} \int J_{PO}(l')H_0^{(2)}(k|r-r'|) dl', \quad (5.25)$$

are evaluated using an infinite series of the form

$$S^{PO}[\mathcal{N}(k, \eta)] = \sum_{n=1}^{\infty} \Delta \mathcal{N}_{near}^{pq}(k, \eta) \exp\{jk_0(x' \cos \theta_g + y' \sin \theta_g)\}, \quad (5.26)$$

where  $\Delta = 0.01\lambda$  is the step size,  $\mathcal{N}(k, \eta)$  represents an evaluation of the near-field operator  $\mathcal{N}$  using a propagation constant  $k$  and intrinsic impedance  $\eta$ ,

$$\begin{aligned} x' &= x_e + (n - 0.5)\Delta \cos \phi_s \\ y' &= y_e + (n - 0.5)\Delta \sin \phi_s, \end{aligned} \quad (5.27)$$

are the coordinates of the source point,  $(x_e, y_e)$  are the coordinates of the end point of the modeled surface (on the extension), and  $\theta_g$  and  $\phi_s$  are the grazing illumination angle and angle of the infinite extension, as shown in Figure 5.1.

For perfectly conducting surfaces, the infinite series then becomes

$$H_z^{PO}(l) = -2S^{PO}[\mathcal{H}_{near}^{VV}(k_0, \eta_0)], \quad (5.28)$$

for vertical polarization and

$$E_z^{PO}(l) = 2/\eta_0 \cos(\theta_i + \phi_s)S^{PO}[\mathcal{E}_{near}^{HH}(k_0, \eta_0)], \quad (5.29)$$

for horizontal polarizations. The operators  $\mathcal{H}_{near}^{VV}$  and  $\mathcal{E}_{near}^{HH}$  are given by

$$\mathcal{H}_{near}^{VV}(k, \eta) = j\frac{k}{4} \cos \psi H_1^{(2)}(kR), \quad (5.30)$$

$$\mathcal{E}_{near}^{HH}(k, \eta) = -\frac{\eta}{4} H_0^{(2)}(kR), \quad (5.31)$$

where

$$R = |\mathbf{r} - \mathbf{r}'| = \sqrt{(x - x')^2 + (y - y')^2}, \quad (5.32)$$

$$\cos \psi = \frac{1}{R} [(\mathbf{r} - \mathbf{r}') \cdot \hat{\mathbf{n}}]. \quad (5.33)$$

The large argument approximation for the Hankel function [7]

$$H_p^{(2)}(x) \simeq \sqrt{\frac{2}{\pi x}} e^{j[x - p(\pi/2) - \pi/4]}, \quad x \rightarrow \infty, \quad (5.34)$$

was used for  $x > 50\lambda$  in equations (5.30) and (5.31), thereby decreasing the amount of total execution time required for evaluation of the scattering by approximately 10%.

For impedance surfaces, the near-field radiation for vertical polarization is given by

$$H_z^{PO} = (\Gamma - 1) \left\{ S^{PO} [\mathcal{H}_{near}^{VV}(k_0, \eta_0)] - (Z_s/\eta_0^2) S^{PO} [\mathcal{E}_{near}^{HH}(k_0, \eta_0)] \right\}, \quad (5.35)$$

where the reflection coefficient  $\Gamma$  is given by

$$\Gamma = (Z_s \cos \theta_t - \eta_0 \cos \theta_i) / (Z_s \cos \theta_t + \eta_0 \cos \theta_i), \quad (5.36)$$

$\cos \theta_t = 1$ , and  $\theta_i = \pi/2 - \theta_g$  is the illumination angle referenced to vertical. For horizontal polarization, the near-field radiation is

$$E_z^{PO} = (1 - \Gamma) \cos \theta_i / \eta_0 \left\{ S^{PO} [\mathcal{E}_{near}^{HH}(k_0, \eta_0)] - Z_s S^{PO} [\mathcal{H}_{near}^{VV}(k_0, \eta_0)] \right\}. \quad (5.37)$$

For low-loss dielectric surfaces, the source terms must be found for both the external and internal equivalent models. In the external equivalent model, the near-field radiation of the physical optics current for horizontal polarization is

$$E_z^{PO} = (1 - \Gamma) \cos \theta_i / \eta_0 S^{PO} [\mathcal{E}_{near}^{HH}(k_0, \eta_0)] - (1 + \Gamma) S^{PO} [\mathcal{H}_{near}^{VV}(k_0, \eta_0)], \quad (5.38)$$

where now the cosine of the angle of the transmitted field is given by

$$\cos \theta_t = \sqrt{1 - k_0^2/k_d^2 \sin^2 \theta_i}, \quad (5.39)$$

and the reflection coefficient  $\Gamma$  is given in equation (5.36). For the internal equivalent model,

$$E_z^{PO} = (1 - \Gamma) \cos \theta_i / \eta_0 S^{PO} [\mathcal{E}_{near}^{HH}(k_d, \eta_d)] - (1 + \Gamma) S^{PO} [\mathcal{H}_{near}^{VV}(k_d, \eta_d)]. \quad (5.40)$$

For vertical polarization, equations (5.38) and (5.40) are used with the dual quantities  $1/Z_s$  and  $1/\eta_d$  replacing  $Z_s$  and  $\eta_d$ , respectively.

The interaction matrix describes the near-field radiation of each unknown current basis function at every match point. It includes both the pulse basis functions in the moment method region of the surface and the GTD basis functions that describe the infinitely extending GTD current on the extensions. Evaluations of  $L_X[J_{MM}]$  are unchanged from that given by Axline and Fung [27]. Pulse basis and impulse testing functions (yielding point matching) are used for the moment method region. Given below are the matrix elements for indices  $m = 0, 1, \dots, N-1$  and  $n = 0, 1, \dots, N-1$ . Note that for low-loss dielectric surfaces, the interaction matrix contains  $2N \times 2N$  elements.

For perfectly conducting surfaces, the vertical polarization interaction matrix elements are given by

$$Z_{m,n}^{VV} = \begin{cases} 0.5 & m = n \\ \Delta L_m \mathcal{H}_{near}^{VV}(k_0, \eta_0) & m \neq n \end{cases}, \quad (5.41)$$

where  $\Delta L_m$  is the width of the  $m$ -th surface segment. For horizontal polarization, the elements are

$$Z_{m,n}^{HH} = \begin{cases} \mathcal{A}(k_0, \eta_0) & m = n \\ \Delta L_m \mathcal{E}_{near}^{HH}(k_0, \eta_0) & m \neq n \end{cases}, \quad (5.42)$$

where

$$\mathcal{A}(k, \eta) = -\frac{\eta k}{4} \Delta L_m \left[ 1 - j \frac{2}{\pi} \ln(\gamma k \Delta L_m / 4) \right], \quad (5.43)$$

and  $\gamma = 0.6552612$  is Euler's number. For both equations (5.41) and (5.42), the source is the current on the  $n$ -th surface segment, and the observation is the center of the

$m$ -th segment.

For surfaces satisfying the impedance boundary conditions, the vertical polarization interaction matrix elements are

$$Z_{m,n}^{VV} = \begin{cases} 0.5 - (Z_s/\eta_0^2)\mathcal{A}(k_0, \eta_0) & m = n \\ \Delta L_m [\mathcal{H}_{near}^{VV}(k_0, \eta_0) - (Z_s/\eta_0^2)\mathcal{E}_{near}^{HH}(k_0, \eta_0)] & m \neq n \end{cases}, \quad (5.44)$$

and for horizontal polarization

$$Z_{m,n}^{HH} = \begin{cases} \mathcal{A}(k_0, \eta_0) - 0.5Z_s & m = n \\ \Delta L_m [\mathcal{E}_{near}^{HH}(k_0, \eta_0) - Z_s\mathcal{H}_{near}^{VV}(k_0, \eta_0)] & m \neq n \end{cases}. \quad (5.45)$$

Finally, for low-loss dielectric surfaces, both the horizontal polarization interaction matrix elements are given by

$$Z_{m,n} = \begin{cases} \mathcal{A}(k_0, \eta_0) & m = n \\ \Delta L_m \mathcal{E}_{near}^{HH}(k_0, \eta_0) & m \neq n \end{cases}, \quad (5.46)$$

$$Z_{m,n+N} = \begin{cases} -0.5 & m = n \\ -\Delta L_m \mathcal{H}_{near}^{VV}(k_0, \eta_0) & m \neq n \end{cases}, \quad (5.47)$$

$$Z_{m+N,n} = \begin{cases} \mathcal{A}(k_d, \eta_d) & m = n \\ \Delta L_m \mathcal{E}_{near}^{HH}(k_d, \eta_d) & m \neq n \end{cases}, \quad (5.48)$$

and

$$Z_{m+N,n+N} = \begin{cases} 0.5 & m = n \\ -\Delta L_m \mathcal{H}_{near}^{VV}(k_d, \eta_d) & m \neq n \end{cases}. \quad (5.49)$$

The vertical polarization matrix elements use equations (5.46) through (5.49) with the dual quantities  $1/Z_s$  and  $1/\eta_d$  replacing  $Z_s$  and  $\eta_d$ , respectively.

When the source current is the infinitely extending diffraction-current, an evaluation of  $L_X[J_d]$  is required. As with the near-field radiation of the physical optics current in the source calculations, this evaluation involves the infinite integration of



a rapidly oscillating, slowly converging integrand well suited to acceleration via the epsilon algorithm. The infinite series used to evaluate

$$L_M[J_d(l)] = 0.5J_d(l) + j\frac{k}{4} \int J_d(l') (\hat{\mathbf{n}}' \cdot \mathbf{r}') H_1^{(2)}(k|r - r'|) dl', \quad (5.50)$$

and

$$L_E[J_d(l)] = \frac{k\eta_0}{4} \int J_d(l') H_0^{(2)}(k|r - r'|) dl', \quad (5.51)$$

are of the form

$$S^{GTD} [\mathcal{N}_{near}^{pq}(k, \eta), B_n] = \sum_{n=1}^{\infty} \Delta \mathcal{N}(k, \eta) B_n^{GTD}(R_d, k), \quad (5.52)$$

where

$$R_d = \sqrt{(x' - x_d)^2 + (y' - y_d)^2}, \quad (5.53)$$

is the distance between the diffraction point  $(x_d, y_d)$  and the source point  $(x', y')$  given by

$$\begin{aligned} x' &= x_e + (n - 0.5)\Delta \cos \phi_s \\ y' &= y_e + (n - 0.5)\Delta \sin \phi_s. \end{aligned} \quad (5.54)$$

The GTD basis functions are

$$B_1^{GTD}(r, k) = \exp(-jkr)/\sqrt{r} \quad (\text{vertical polarization}) \quad (5.55)$$

$$B_2^{GTD}(r, k) = \exp(-jkr)/r^{1.5} \quad (\text{horizontal polarization}). \quad (5.56)$$

The near-field radiation of the GTD currents on a perfectly conducting surface is then

$$Z_{m,n} \Big|_{n=GTD} = S^{GTD} [\mathcal{H}_{near}^{VV}(k_0, \eta_0), B_1^{GTD}], \quad (5.57)$$

and

$$Z_{m,n} \Big|_{n=GTD} = S^{GTD} [\mathcal{E}_{near}^{HH}(k_0, \eta_0), B_2^{GTD}], \quad (5.58)$$

for vertically and horizontally polarized illumination. For impedance surfaces, the near-field radiation of the GTD currents for vertical and horizontal polarizations are given by

$$Z_{m,n}\Big|_{n=GTD} = S^{GTD} \left[ \mathcal{H}_{near}^{VV}(k_0, \eta_0), B_1^{GTD} \right] - (Z_s/\eta^2) S^{GTD} \left[ \mathcal{E}_{near}^{HH}(k_0, \eta_0), B_1^{GTD} \right], \quad (5.59)$$

and

$$Z_{m,n}\Big|_{n=GTD} = S^{GTD} \left[ \mathcal{E}_{near}^{HH}(k_0, \eta_0), B_2^{GTD} \right] - Z_s S^{GTD} \left[ \mathcal{H}_{near}^{VV}(k_0, \eta_0), B_2^{GTD} \right]. \quad (5.60)$$

For horizontal polarization in the low-loss dielectric case,

$$Z_{m,n}\Big|_{n=GTD} = S^{GTD} \left[ \mathcal{E}_{near}^{HH}(k_d, \eta_d), B_2^{GTD} \right], \quad (5.61)$$

$$Z_{m,n+N}\Big|_{n=GTD} = S^{GTD} \left[ \mathcal{H}_{near}^{VV}(k_d, \eta_d), B_1^{GTD} \right], \quad (5.62)$$

$$Z_{m+N,n}\Big|_{n=GTD} = S^{GTD} \left[ \mathcal{E}_{near}^{HH}(k_d, \eta_d), B_2^{GTD} \right], \quad (5.63)$$

$$Z_{m+N,n+N}\Big|_{n=GTD} = S^{GTD} \left[ \mathcal{H}_{near}^{VV}(k_d, \eta_d), B_1^{GTD} \right]. \quad (5.64)$$

Again, for vertical polarization the dual quantities are used in these matrix element equations.

Finally, the matrix form of the linear system of equations can be solved using the LU Decomposition algorithm.

## 5.4.2 Far-field Scattering Calculations

The radiation of  $J_{MM}$  in equations (5.16) and (5.17) is accomplished using the far-field approximations given by Axline and Fung [27]. By using these approximations and by using the large argument approximations for the Hankel functions, the integrations in  $L_X[J_d(l)]\Big|_{r \rightarrow \infty}$  can be evaluated in terms of Fresnel integrals.  $L_M[J_d(l)]\Big|_{r \rightarrow \infty}$  and

$L_E[J_d(l)]$  become

$$\begin{aligned}
L_M[B_1(k, \eta)]\Big|_{r \rightarrow \infty} &= \alpha j 2 e^{j3\pi/4} \cos \theta'_s \Phi \mathcal{F}(Ax'_e) / \sqrt{A} \\
L_M[B_2(k, \eta)]\Big|_{r \rightarrow \infty} &= \alpha j e^{j3\pi/4} \cos \theta'_s \Phi I(x'_e) \\
L_E[B_1(k, \eta)]\Big|_{r \rightarrow \infty} &= -\alpha 2 \eta e^{j\pi/4} \Phi \mathcal{F}(Ax'_e) / \sqrt{A} \\
L_E[B_2(k, \eta)]\Big|_{r \rightarrow \infty} &= -\alpha \eta e^{j\pi/4} \Phi I(xe') \tag{5.65}
\end{aligned}$$

where

$$\begin{aligned}
\Phi &= \sqrt{\frac{k_0}{8\pi}} e^{k_0(x_d \sin \theta_s + y_d \cos \theta_s)}, \\
I(x'_e) &= \frac{2e^{-jkAx'_e}}{\sqrt{x'_e}} - 4j\sqrt{A}\mathcal{F}\left(\sqrt{Ax'_e}\right), \\
A &= k_0(1 - \sin \theta'_s), \tag{5.66}
\end{aligned}$$

$\theta'_s = \theta_s + \phi_s$ ,  $\theta_s$  is the scattering angle (referenced to vertical),  $\phi_s$  is the angle the infinite extension makes with the horizontal,  $(x_d, y_d)$  is the diffraction point,  $x'_e$  is the distance between A and B (or C and D) on the surface,  $\alpha$  is the basis function weight determined by the moment method solution, and  $\mathcal{F}$  is the Fresnel integral

$$\mathcal{F}(x) = \int_x^\infty \exp[-j(\pi/2)\tau^2] d\tau. \tag{5.67}$$

The duals of these equations may be formed by making the substitutions  $1/Z_s$  for  $Z_s$  and  $1/\eta$  for  $\eta$ .

Evaluation of  $L_X[J_{PO}(l)]\Big|_{r \rightarrow \infty}$  requires more consideration. Using the approximation of Axline and Fung yields an integrand that does not decay out to infinity, and therefore technically has no solution. The integral is in the form [45]

$$I = \int_a^b \psi(x) e^{j\nu\mu(x)} dx, \tag{5.68}$$

where  $\mu(z)$  and  $\psi(z)$  are functions of the complex variable  $z$ , and  $\nu$  is a large, real multiplicative constant. Furthermore,  $\mu(z)$  is real on the real axis, and  $\psi(z)$  is slowly

varying. This type of integral can be expanded in terms of the end points using integration by parts as [45]

$$I = \frac{\psi(x)}{j\nu\mu_x(x)} e^{j\nu\mu(x)} \Big|_a^b - \frac{1}{(j\nu)^2} \left\{ \frac{d}{dx} \left( \frac{\psi}{\mu_x} \right) \frac{1}{\mu_x} e^{j\nu\mu} \right\}_a^b + (\text{higher order terms}). \quad (5.69)$$

The exact integral was evaluated at a very large (but finite) observation range. The far-field scatter for the physical optics current for horizontal polarization is then

$$\begin{aligned} & L_E[J_{PO}(l)] \Big|_{r \rightarrow \infty} \\ &= -j\eta e^{j\pi/4} \frac{1}{\sin \theta'_s + \sin \theta'_i} \frac{1}{\sqrt{8\pi k_0}} e^{jk_0[x_e(\sin \theta_s + \sin \theta_i) + y_e(\cos \theta_s + \cos \theta_i)]}, \end{aligned} \quad (5.70)$$

and for vertical polarization is

$$\begin{aligned} & L_M[J_{PO}(l)] \Big|_{r \rightarrow \infty} \\ &= -\cos \theta''_s e^{j3\pi/4} \frac{1}{\sin \theta'_s + \sin \theta'_i} \frac{1}{\sqrt{8\pi k_0}} e^{jk_0[x_e(\sin \theta_s + \sin \theta_i) + y_e(\cos \theta_s + \cos \theta_i)]}, \end{aligned} \quad (5.71)$$

where  $\theta'_s = \theta_s + \phi_s$ ,  $\theta'_i = \theta_i + \phi_s$ , and

$$\theta''_s = \begin{cases} \theta'_s & (\text{front face}) \\ \pi + \theta'_s & (\text{back face}) \end{cases}. \quad (5.72)$$

## 5.5 Evaluation of the Hybrid MM/GTD Technique

The full hybrid MM/GTD technique can be tested only for surface geometries that permit the addition of infinite extensions that are shadowed from all points of the main scattering surface (except the intersection points), as shown in Figure 5.1. A simple surface that meets the requirements of this type of surface is a wedge with a rounded apex, as shown in Figure 4.15. The geometry of this surface is identical to the perfectly conducting surface discussed in section 4.6. The apex of the wedge is rounded off with a radius of curvature of  $0.5\lambda$ , and the interior angle of the wedge is  $120^\circ$ .

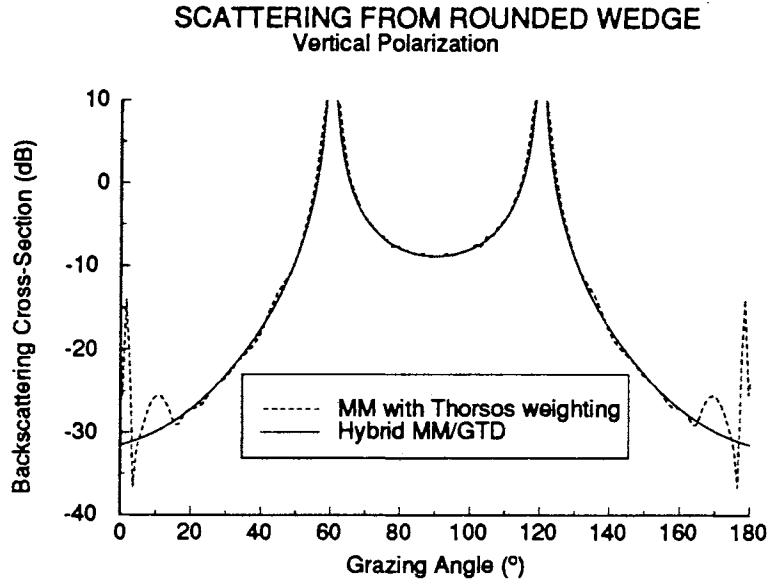


Figure 5.3: Vertical scattering from perfectly conducting rounded wedge.

The results plotted in Figures 5.3 and 5.4 compare the scattering from a perfectly conducting rounded wedge predicted by the hybrid MM/GTD technique with the scattering predicted by the moment method with a Thorsos illumination weighting function for vertical and horizontal polarizations, respectively. Artificial edge effects due to the truncation of the surface model are quite apparent in the standard moment method results. In the hybrid MM/GTD analysis, however, the extensions of the surface are infinite, and adverse edge effects are not present in the predicted scatter.

Using the hybrid MM/GTD results for a perfectly conducting wedge as a reference, the backscattering width was calculated for wedges with dielectric constants  $\epsilon_r = 3 - j0$ ,  $\epsilon_r = 10 - j2$ , and  $\epsilon_r = 35 - j5$ . These results are plotted in Figures 5.5 and 5.6 for vertical and horizontal polarizations, respectively. Most prominent are the singularities at  $60^\circ$  and  $120^\circ$  due to the specular reflections from the front and back faces of the wedge. At other scattering angles, no exact solution for the backscatter is available for dielectric surfaces, although some reduction in the backscatter

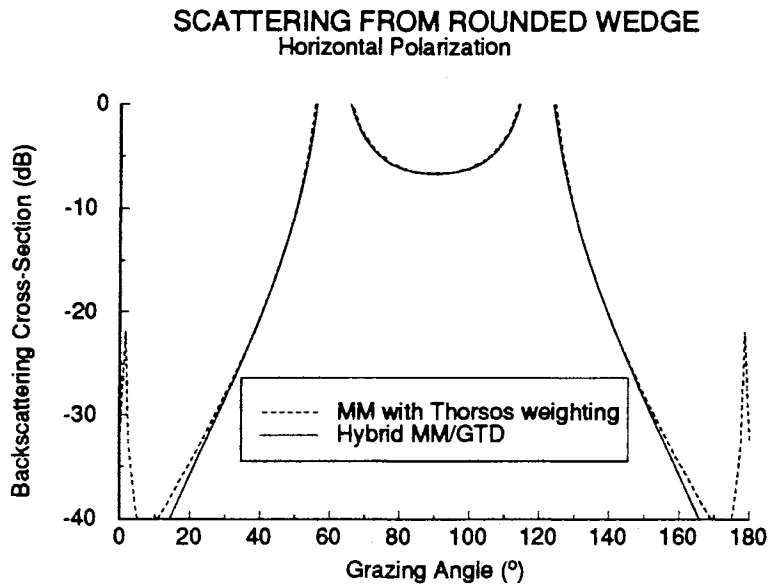


Figure 5.4: Horizontal scattering from perfectly conducting rounded wedge.

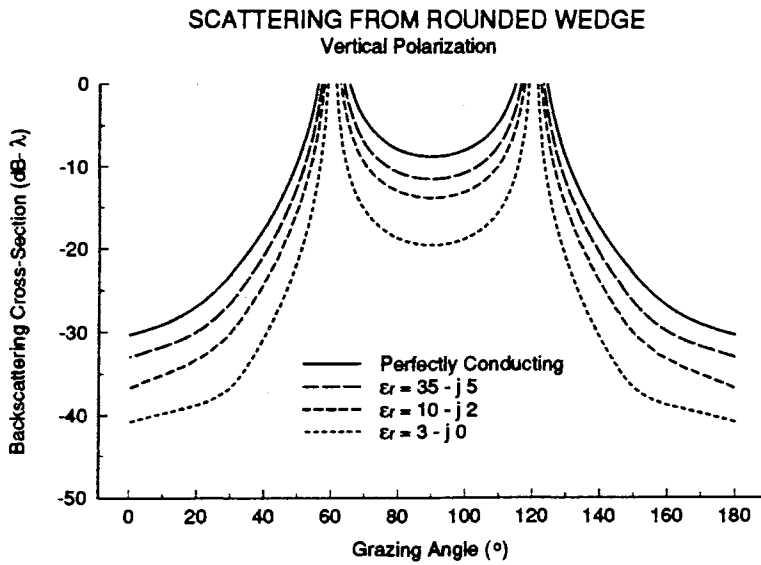


Figure 5.5: Scattering from rounded-apex wedge: vertical polarization.

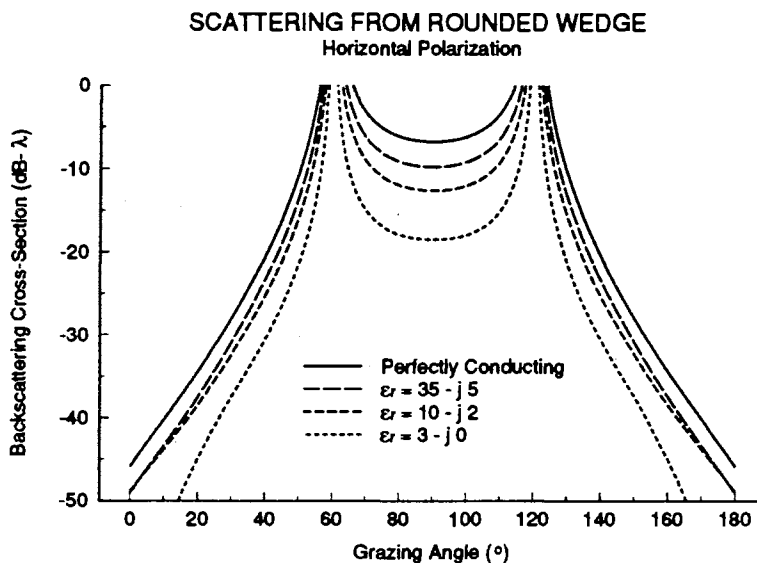


Figure 5.6: Scattering from rounded-apex wedge: horizontal polarization.

Table 5.1: Reductions in the rounded wedge backscatter, vertical polarization.

$\epsilon_r$	$ \Gamma_v $	Reduction (dB)		
		<i>Expected</i>	<i>Observed</i>	<i>Error (dB)</i>
$35 - j5$	0.7127	2.9416	2.7680	0.1736
$10 - j2$	0.5252	5.5932	5.0905	0.5027
$3 - j0$	0.2679	11.4390	10.8398	0.5992

is expected due to reductions in the magnitude of the normal-incidence flat-surface reflection coefficient. Tables 5.1 and 5.2 compare the magnitude of the reflection coefficients to the observed reduction in the backscatter at normal incidence ( $\theta_g = 90^\circ$ ), for vertical and horizontal polarizations. Note that the observed reduction is merely the difference between the backscatter for a perfect conductor and that for the dielectric surface of interest. The hybrid MM/GTD backscatter is within 0.6 dB of the backscatter that would be predicted from the normal-incidence reflection coefficient for each configuration and for both polarizations.

When the illumination grazes the extensions for  $\theta_g = 30^\circ$  and  $\theta_g = 150^\circ$ , the

Table 5.2: Reductions in the rounded wedge backscatter, horizontal polarization.

$\epsilon_r$	$ \Gamma_v $	Reduction (dB)		
		<i>Expected</i>	<i>Observed</i>	<i>Error (dB)</i>
$35 - j5$	0.7127	2.9416	3.0303	-0.0887
$10 - j2$	0.5252	5.5932	5.8867	-0.2935
$3 - j0$	0.2679	11.4390	11.7670	-0.3280

diffraction-field is not ray optical, and the currents predicted by equation 5.4 should be in error. Nevertheless, the erroneous current does not seem to matter as the far-field backscatter does not show any abnormalities or discontinuities at these illumination angles. This observation is consistent with a study by Booyesen *et al.* [46] that used a hybrid technique that didn't include the effects of GTD currents at all, but still achieved accurate results. Therefore, it appears that the most important effect of the GTD currents is to prevent artificial edge effects from contributing to the illumination and far-field scatter.



# Chapter 6

## APPLICATION

In this chapter, the hybrid MM/GTD technique is used to investigate the effects of small-scale roughness in the shadowed portions of dielectric surfaces that represent geological features. This investigation closely parallels an investigation by West [10] which concluded that shadowed roughness can significantly contribute to backscatter from perfectly conducting surfaces. When the roughness is weakly shadowed, West found that these contributions were apparent for both horizontal and vertical polarizations. For deeply shadowed roughness, however, the shadowed roughness only contributed to the vertically polarized backscatter. West's findings suggest that a binary description of the surface self-shadowing is not accurate for extremely small grazing angles, especially for vertical polarization.

### 6.1 Description

West used two types of surfaces to investigate the effects of shadowed roughness on the far-field backscatter. The first model, shown in Figure 6.1 and hereafter referred to as the “weak-shadowing surface”, resembles a near-breaking ocean wave. The surface between the crests is described by

$$y' = \ln(\sec x'), \quad |x'| \leq \pi/6, \quad (6.1)$$

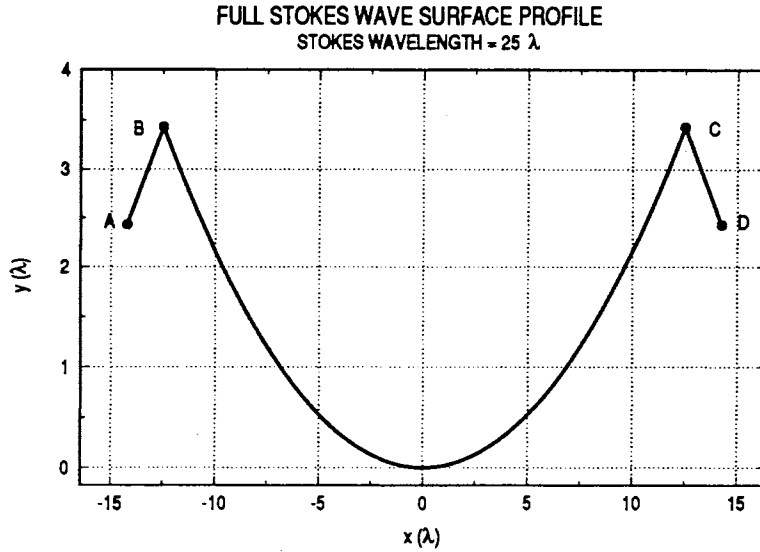


Figure 6.1: Large-scale displacement for full Stokes wave with sharp crests.

where  $x'$  and  $y'$  are normalized coordinates of a single-cycle of a Longuet-Higgins Stokes wave with a wavelength of  $25\lambda$ , where  $\lambda$  is the illumination wavelength [47]. Planar extensions are extended beyond points  $A$  and  $D$  to infinity at an angle  $30^\circ$  from horizontal. This configuration yields crests with internal angles equal to that of an ideal Stokes wave ( $120^\circ$ ). In Figure 6.2, the sharp crests have been rounded off with an adjustable radius-of-curvature (here  $2\lambda$ ) to prevent strong edge diffraction from overwhelming the scatter from the distributed surface. As the illumination strikes the weak-shadowing surface from the right, the front crest (on the right) casts a shadow onto the surface in the Stokes wave trough. When the illumination grazing angle reaches  $0^\circ$ , however, the entire back portion of the surface is in the shadow of the front crest. However, this shadowing is considered “weak” because the shadow boundary is very close to the roughness on the back crest. A second type of scattering surface, the “deep-shadowing surface”, is formed by setting the back half of the Stokes wave trough displacement to zero, as shown in Figure 6.3. The right crest of this surface casts

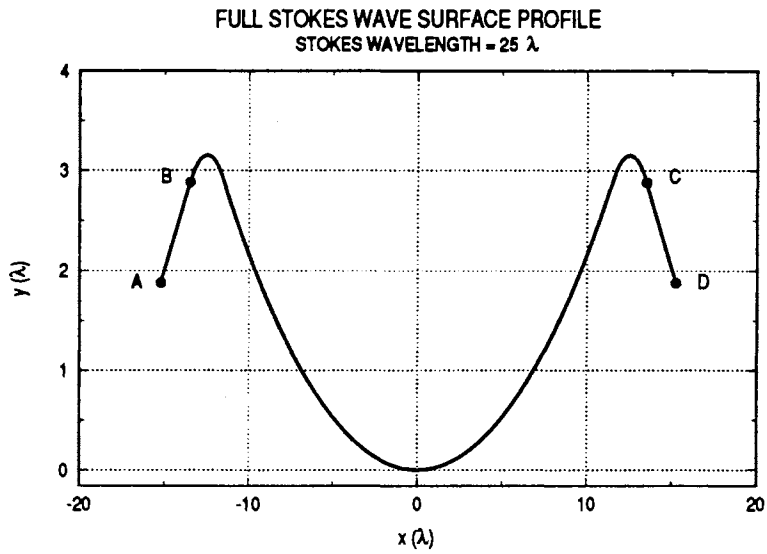


Figure 6.2: Large-scale displacement for full Stokes wave with rounded crests.

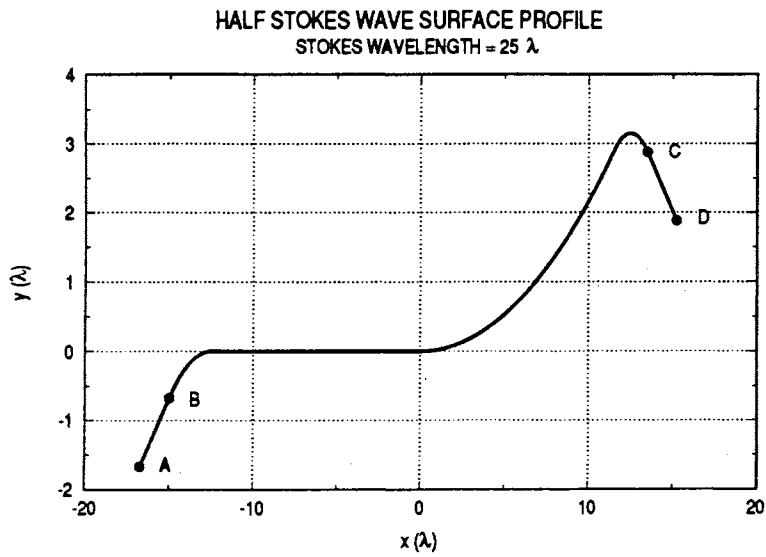


Figure 6.3: Large-scale displacement for half Stokes wave with rounded crests.

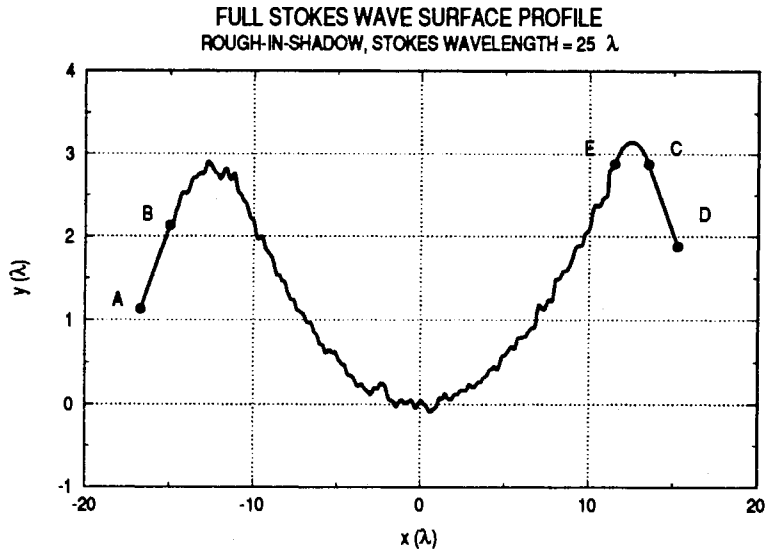


Figure 6.4: “Rough-in-shadow” geometry for weak-shadowing surface.

a deep shadow over the Stokes wave trough when the grazing angle is very small. For this reason, West used this type of surface to investigate the effects of deeply shadowed roughness features on the backscatter.

A Gaussian small-scale roughness is added to each type of surface using either the “rough-in-shadow” or “smooth-in-shadow” roughness configurations. As the name suggests, the rough-in-shadow configuration includes roughness in the shadowed portions of the surface, as would be expected for a true scattering surface. Figures 6.4 and 6.5 show a typical rough-in-shadow surface configuration for the weak-shadowing and deep-shadowing surfaces, respectively. Here, the roughness is added to the surface between points *B* and *E* only. Roughness is not extended to point *C* on the front face of the surface because it would be unrealistically directly illuminated at small grazing angles. The spectrum of the roughness is given by equation (2.8) with  $\sigma_h = 0.045\lambda$  and  $L = 0.2\lambda$ . For the smooth-in-shadow configuration, roughness is included only in the directly illuminated portions of the surface, from point *E* to point *F* where the

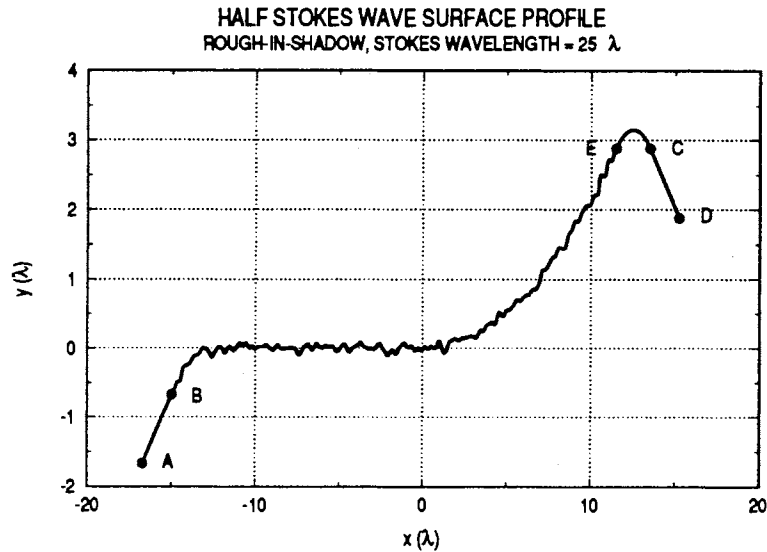


Figure 6.5: “Rough-in-shadow” geometry for deep-shadowing surface.

incident shadow boundary intersects the surface, as shown in Figures 6.6 and 6.7 for the weak-shadowing and deep shadowing surfaces with a grazing illumination angle of  $\theta_g = 10^\circ$ .

By comparing the backscatter from the rough-in-shadow and smooth-in-shadow surfaces, the relative contributions of the shadowed roughness features can be determined, and the applicability of shadowing corrections to the two-scale model can be investigated. West [10] found that deeply shadowed roughness can significantly contribute to the backscatter from perfectly conducting surfaces for vertical polarization. For horizontal polarization, however, deeply shadowed roughness did not significantly contribute to the backscatter. These conclusions confirmed analytical studies by Barrick [8] and Holliday [9] that concluded strong surface currents are induced into shadowed regions for vertical polarization.

Unlike West’s study, which used a perfectly conducting surface model for ocean-wave surfaces, the investigation in this report examines backscattering from the weak-

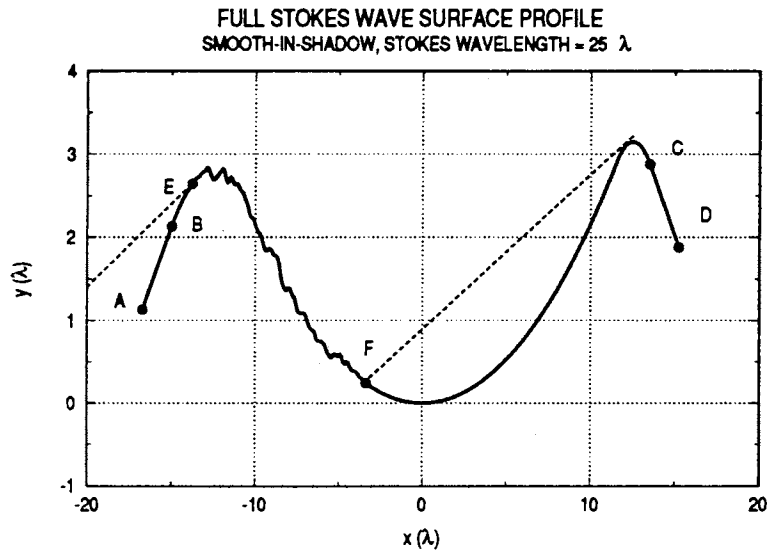


Figure 6.6: “Smooth-in-shadow” geometry for weak-shadowing surface,  $\theta_g = 10^\circ$ .

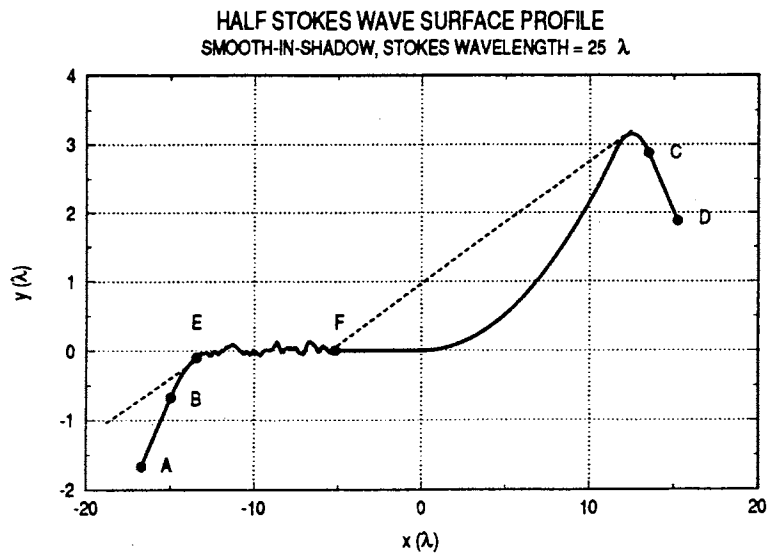


Figure 6.7: “Smooth-in-shadow” geometry for deep-shadowing surface,  $\theta_g = 10^\circ$ .

shadowing and deep-shadowing surfaces using dielectric constants typical of soil. Three dielectric constants were chosen to represent a variety of surface conditions,  $\epsilon_r = 3 - j0$  for dry sand,  $\epsilon_r = 10 - j2$  for “typical soil”, and  $\epsilon_r = 35 - j5$  for very moist soils. It should be noted that the Stokes-wave representation of the surface geometry used here does not accurately model the large-scale displacements of geological surfaces. Instead, these surfaces provide a way to control the shadowing and allow for the results to be compared directly to the results in West’s investigation.

Each modeled surface is divided into  $0.05\lambda$  wide moment-method segments, and the front and back crests are rounded off with radii-of-curvature  $2.0\lambda$  and  $5.0\lambda$ , respectively. The Gaussian roughness with a correlation length  $L = 0.2\lambda$  and a height standard deviation  $\sigma = 0.045\lambda$  is added to the large scale surface displacement for each of the two roughness configurations – rough-in-shadow and smooth-in-shadow. West’s results for a perfectly conducting surface are reproduced and compared with results for surfaces with dielectric constants  $\epsilon_r = 3 - j0$ ,  $\epsilon_r = 10 - j2$ , and  $\epsilon_r = 35 - j5$ . The results are discussed the final section of this chapter.

## 6.2 Backscattering Calculations

In this section, the backscattering results are presented for the weak-shadowing and deep-shadowing surfaces of Figures 6.2 and 6.3, respectively. The backscatter cross-section for each polarization is shown along with the two-scale model predictions, found by integrating the appropriate small-perturbation model backscattering coefficient in equation (3.9) along the illuminated portion of the surface with the incident angle adjusted to account for the local surface tilt. The two-scale model calculations do not include the predictions by the Kirchhoff approximation because this model is known to fail in the presence of surface self-shadowing [9].

The numerical investigation is designed to reveal the importance of shadowed

roughness for a variety of scattering surfaces representative of geological features. The results are presented separately for each surface, and the discussion will focus upon three aspects of the results. First, the two-scale model predictions are compared to the numerical backscatter for each polarization. A threshold of 2 dB is used to define “agreement” between the two-scale predictions and the observed numerical backscatter. The two-scale model predictions are not expected to agree with the numerical backscatter for very small grazing angles where surface self-shadowing occurs. Second, the rough-in-shadow backscatter is compared to the smooth-in-shadow backscatter using the same 2 dB threshold for agreement. A large difference in the backscattering for these roughness configurations indicates that shadowed roughness features are contributing significantly to the backscatter. Finally, the ratio of the rough-in-shadow backscatter at  $30^\circ$  to the rough-in-shadow backscatter at  $0^\circ$  is used to give a rough-estimate of the strength of the shadowing. A large ratio suggests that the backscatter is greatly reduced when the surface is shadowed.

The results represent the ensemble average backscattering cross-section for 40 independent surfaces and over 2800 hours of computational time. For the rough-in-shadow configuration, a rough surface was generated, and the backscatter was found for grazing angles of incidence ranging from  $30^\circ$  to  $0^\circ$  in  $0.5^\circ$  increments. The smooth-in-shadow configuration requires an independent surface to be generated for each incident angle, greatly increasing the amount of computational work. Due to finite computer resources, the backscatter was found only for grazing angles of incidence ranging from  $20^\circ$  to  $0^\circ$  in  $1^\circ$  increments.

### 6.2.1 Perfectly Conducting Reference Surfaces

The backscattering results for perfectly conducting surfaces are shown in Figure 6.8 for the weak-shadowing surface and Figure 6.9 for the deep-shadowing surface. These



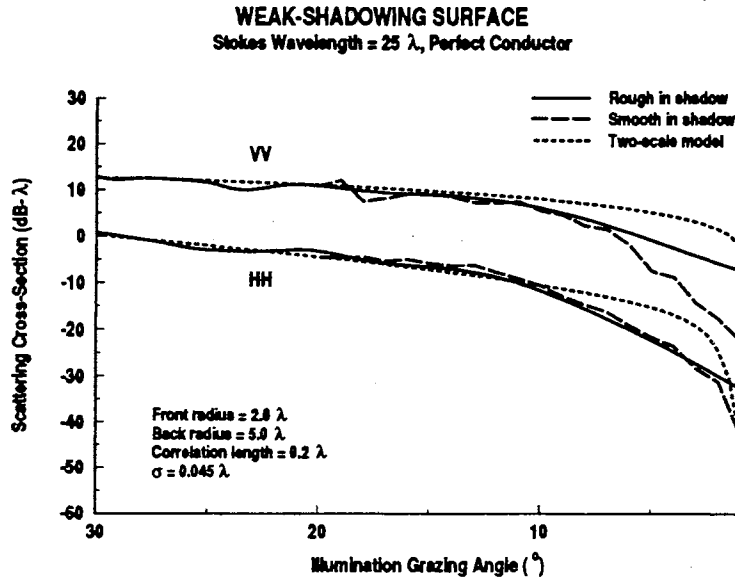


Figure 6.8: Backscattering for perfectly conducting weak-shadowing surface.

results are presented as benchmarks against which the backscattering from impedance and dielectric surfaces can be compared. Most notable on these plots are the angles at which the back side of the surface is entirely shadowed by the front crest, thus causing the smooth-in-shadow configuration to be entirely smooth. Complete shadowing occurs at  $0.5^{\circ}$  for the weak-shadowing surface and  $7^{\circ}$  for the deep-shadowing surface.

The shadow-corrected two-scale model predictions are within 2 dB of the numerical backscatter for the weak-shadowing surface down to approximately  $10^{\circ}$  for both vertical and horizontal polarizations. The two-scale model predictions for the deep-shadowing surface, however, were within 2 dB of the numerical backscatter only down to  $24.5^{\circ}$  for vertical polarization and  $16^{\circ}$  for horizontal polarization. At smaller grazing angles for either surface, the two-scale model over-predicts the backscatter by as much as 8 dB. The two-scale model backscatter drops to zero at  $0.5^{\circ}$  for the weak-shadowing surface and  $7^{\circ}$  for the deep-shadowing surface. The entire back side of the surface is shadowed by the front crest at these angles, and no surface roughness is

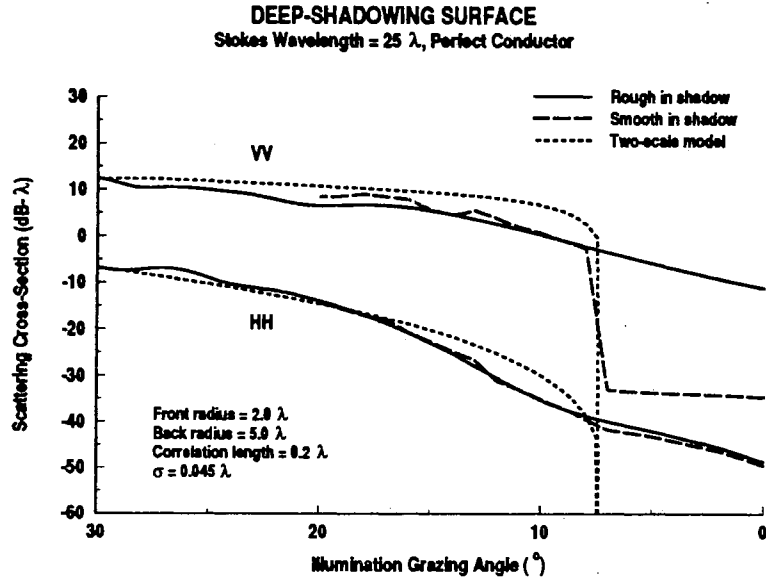


Figure 6.9: Backscattering for perfectly conducting deep-shadowing surface.

directly illuminated.

For the weak-shadowing surface, the rough-in-shadow and smooth-in-shadow backscattering calculations agree to within 2 dB down to  $7^{\circ}$  for vertical polarization and  $2^{\circ}$  for horizontal polarization. The vertically polarized smooth-in-shadow backscatter decreases more rapidly than the corresponding rough-in-shadow backscatter for grazing angles less than  $7^{\circ}$ , and by  $0^{\circ}$  the smooth-in-shadow backscatter is approximately 25 dB less than the rough-in-shadow backscatter. Likewise, the horizontally polarized smooth-in-shadow backscatter drops at approximately  $2^{\circ}$  and by  $0^{\circ}$  is about 14 dB less than the horizontally polarized rough-in-shadow backscatter. These results suggest that weakly shadowed roughness features near the back crest contribute significantly to the backscatter for either polarization.

The rough-in-shadow and smooth-in-shadow calculations for the deep-shadowing surface suggest that deeply shadowed roughness features contribute only to the vertically polarized backscatter. The vertically polarized scatter in the rough-in-shadow

and smooth-in-shadow configurations agree to within 2 dB down to a grazing angle of  $8^\circ$ . The smooth-in-shadow backscatter then drops from -2.5 dB at  $8^\circ$  to -33 dB at  $7^\circ$  (as the surface roughness disappears). At these same angles the rough-in-shadow results do not show a sudden drop as the grazing angle decreases, and it is impossible to tell that the surface is entirely shadowed by the front crest from the scattering alone. However, unlike the vertical polarization results, the horizontally polarized scatter from the rough-in-shadow and smooth-in-shadow surfaces agrees to within 2 dB for all grazing angles.

It is interesting to compare the ratio of the backscatter at  $30^\circ$  to the backscatter at  $0^\circ$  for both polarizations. For the weak-shadowing surface, the vertical backscatter at  $30^\circ$  is 21.6 dB more than the vertical backscatter at  $0^\circ$ , and the horizontal backscatter ratio is 35.9 dB. The vertical and horizontal backscattering ratios are 23.5 dB and 42.0 dB, respectively, for the deep-shadowing surface. These relatively low  $30^\circ/0^\circ$  ratios for both polarizations in the weak-shadowing surface and for vertical polarization in the deep-shadowing surface further support the conclusion that weakly shadowed roughness is important and that deeply shadowed roughness is important only for vertical polarization.

### 6.2.2 Moist Clay Surface ( $\epsilon_r = 35 - j5$ )

The backscattering results plotted in Figure 6.10 and 6.11 are for weak-shadowing and deep-shadowing surfaces that have a dielectric constant  $\epsilon_r = 35 - j5$ , which is representative of moist clay surfaces [15]. Here, the impedance boundary conditions of equation (4.25) are satisfied, and the integral equations for this type of surface are used in the hybrid MM/GTD technique. The plots are similar to those for perfectly conducting surfaces, although the backscattering cross-sections at  $30^\circ$  grazing are reduced in magnitude by about 6.5 dB for vertical polarization and 2.8 dB for

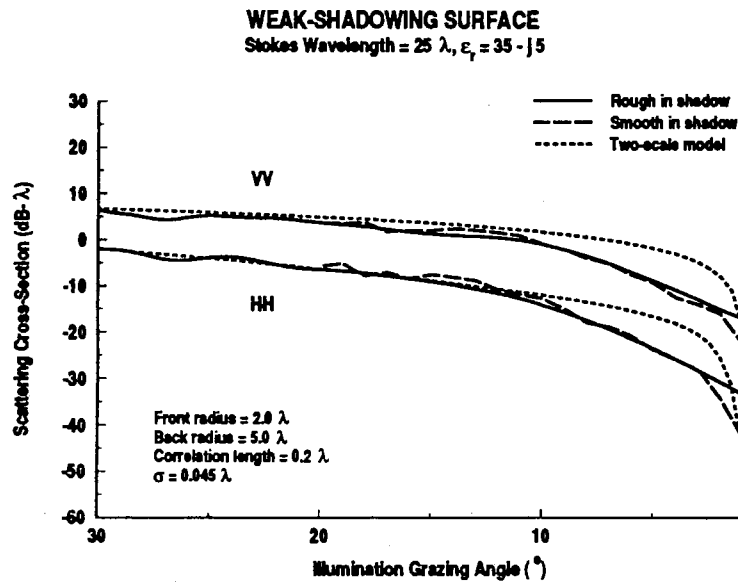


Figure 6.10: Backscattering for “moist-clay” weak-shadowing surface.

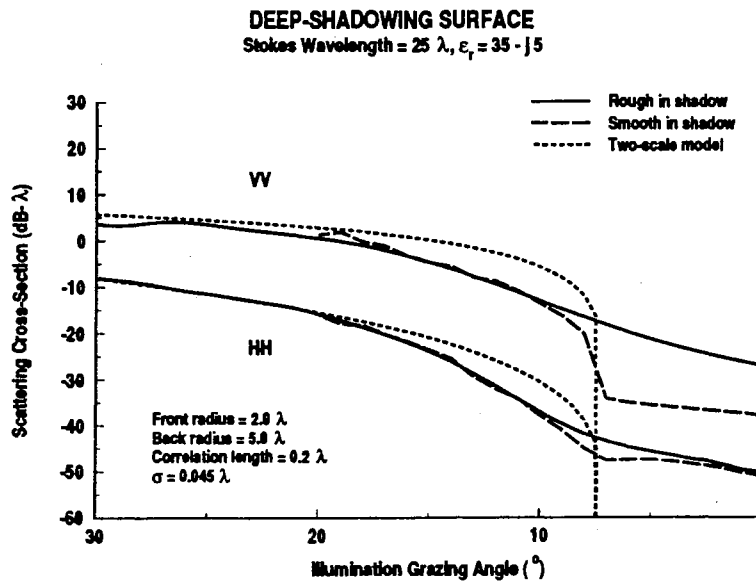


Figure 6.11: Backscattering for “moist-clay” deep-shadowing surface.

horizontal polarization.

The two-scale model predictions agree with the calculated backscatter to within 2 dB down to approximately  $17^\circ$  (VV) and  $10.5^\circ$  (HH) for the weak-shadowing surface and  $21.5^\circ$  (VV) and  $16.5^\circ$  (HH) for the deep-shadowing surface. The backscatter is over-predicted by the two-scale model for smaller grazing angles where some of the roughness is directly illuminated. The two-scale model predictions drop to zero when the entire surface roughness is in the shadow of the front crest, at  $0.5^\circ$  for the weak-shadowing surface and at  $7^\circ$  for the deep-shadowing surface.

The smooth-in-shadow and rough-in-shadow numerical calculations for the weak-shadowing surface agree to within 2 dB for grazing angles down to approximately  $2^\circ$  for vertical polarization and  $3^\circ$  for horizontal polarization. At lower grazing angles of incidence the smooth-in-shadow results drop off significantly as the amount of roughness on the surface decreases. When the illumination grazes the surface at  $0^\circ$ , the difference between the smooth-in-shadow and rough-in-shadow results is 22 dB for vertical and 14 dB for horizontal. It is clear that weakly shadowed roughness continue to contribute to the backscatter, even for imperfectly conducting surfaces that resemble moist clay.

The deep-shadowing surface backscatter indicates that deeply-shadowed roughness contributes to the vertically polarized backscatter for surfaces with this dielectric constant. The vertically polarized backscattering cross-section for the smooth-in-shadow configuration agrees with the rough-in-shadow backscatter to within 2 dB down to  $9^\circ$  grazing. Between  $9^\circ$  and  $6^\circ$  the smooth-in-shadow backscatter drops by approximately 20 dB, and by  $0^\circ$  is nearly 11 dB less than the rough-in-shadow backscatter. The horizontal smooth-in-shadow backscatter is within 2 dB of the horizontal rough-in-shadow backscatter for all grazing angles of incidence except for near  $7^\circ$  grazing, where it is some 4.2 dB less than the rough-in-shadow backscatter. It is at this angle that the

incident shadow boundary grazes the roughness on the back of the surface. Below  $7^\circ$ , the roughness in the smooth-in-shadow configuration disappears.

The rough-in-shadow backscattering ratios ( $30^\circ/0^\circ$ ) provide further insight into the effectiveness of shadowing for these surface types. For the weak-shadowing surface, the ratio is 25.6 dB for vertical polarization and 33.8 dB for horizontal polarization. The backscattering ratios for the deep-shadowing surface are 30.6 dB and 42.4 dB for vertical and horizontal polarizations respectively. The weak-shadowing ratios support the conclusion that weakly shadowed roughness is important for backscattering in both polarizations. Likewise, it appears from the deep-shadowing ratios that shadowing is slightly more effective for vertical polarization than it is for a perfect conductor. However, deeply shadowed roughness on an impedance surface may still contribute to the vertically polarized, but not horizontally polarized backscatter.

### 6.2.3 Average Soil Surface ( $\epsilon_r = 10 - j2$ )

Using the hybrid MM/GTD technique for low-loss dielectric surfaces, the backscatter was calculated for weak-shadowing and deep-shadowing surfaces with a dielectric constant of  $\epsilon_r = 10 - j2$ , a value chosen to represent a “typical” value for soil. The results are shown in Figures 6.12 and 6.13. Here, the backscattering is again reduced from the perfectly conducting case. At  $30^\circ$  grazing, the vertically polarized backscatter is reduced by about 10.8 dB from the perfectly conducting case, and the reduction is approximately 3.3 dB for horizontal polarization.

For this dielectric constant, the two-scale model predictions agree with the calculated backscatter down to approximately  $14.5^\circ$  (VV) and  $9.5^\circ$  (HH) for the weak-shadowing surface and  $17.5^\circ$  (VV) and  $14.5^\circ$  (HH) for the deep-shadowing surface. The hybrid MM/GTD calculations drop more quickly than the two-scale predictions for smaller grazing angles of incidence.

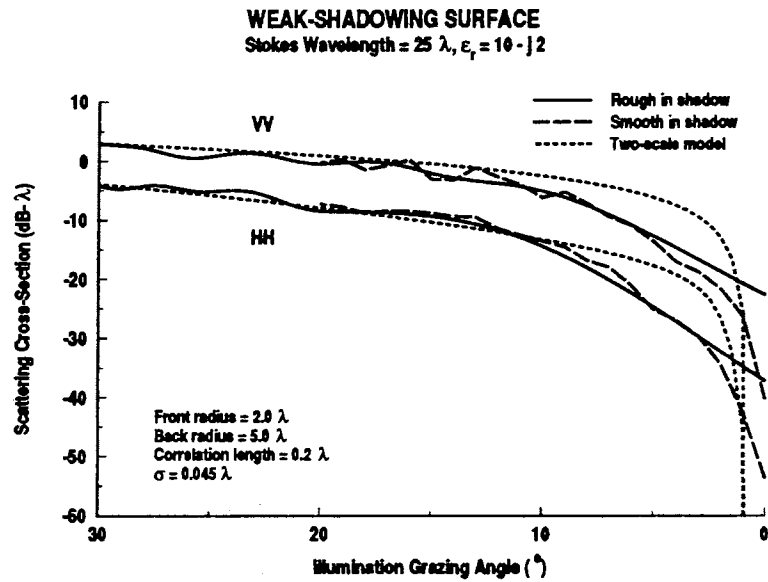


Figure 6.12: Backscattering for a “typical-soil” weak-shadowing surface.

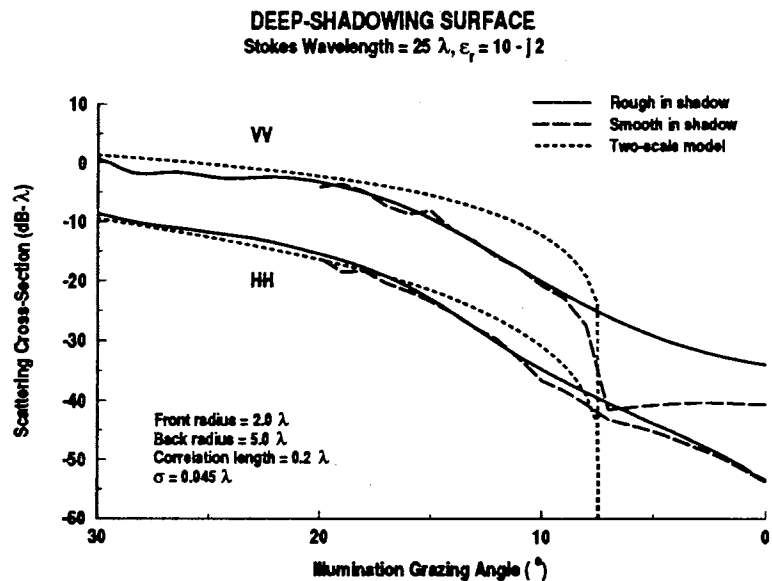


Figure 6.13: Backscattering for a “typical-soil” deep-shadowing surface.

The vertically polarized smooth-in-shadow and rough-in-shadow scatter for the weak-shadowing surface follow each other closely down to approximately  $4^\circ$ , where the smooth-in-shadow scatter drops in magnitude until it is almost 17.5 dB less than the rough-in-shadow scattering at  $0^\circ$ . The horizontal smooth-in-shadow scatter also drops much like the vertical scatter. At  $2^\circ$  the horizontal smooth-in-shadow scatter begins to drop compared to the rough-in-shadow scatter, and by  $0^\circ$  is about 16.4 dB less. The contributions by the weakly shadowed roughness appear to be less for this dielectric constant than for the previous two cases.

The vertically polarized backscatter from the smooth-in-shadow configuration in the deep-shadowing case drops off by about 16 dB between  $8^\circ$  and  $7^\circ$ , at which point the roughness disappears. The backscattering cross-section then rises back to within 6.7 dB of the rough-in-shadow vertical backscatter at a grazing illumination angle of  $0^\circ$ . The cause of this rise is most likely numerical error. The horizontally polarized scatter is not affected significantly by the presence or absence of roughness in the shadowed region. The smooth-in-shadow backscatter is within 2 dB of the rough-in-shadow backscatter for all grazing angles except  $7^\circ$ , where it is 2.7 dB less than the rough-in-shadow backscattering cross-section. These results indicate that although deeply shadowed roughness still contributes to the vertically polarized backscatter, the contributions are less significant than the contributions to the backscatter from perfect conducting or the "moist-clay" surfaces.

The  $30^\circ/0^\circ$  backscattering ratios for the weak-shadowing surface are 25.8 dB and 33.1 dB for vertical and horizontal polarizations, respectively. The deep-shadowing surface backscattering ratios are 34.8 dB for vertical polarization and 44.8 dB for horizontal polarization. The relatively low ratios in the weak-shadowing case again suggest that weakly shadowed roughness contributes to the backscatter for both polarizations, although shadowing is more effective for this dielectric constant. The deep-shadowing



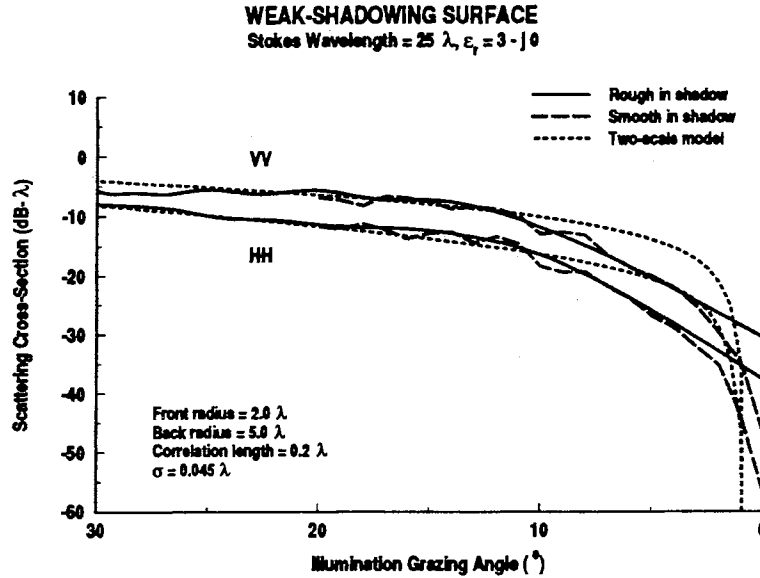


Figure 6.14: Backscattering for a “dry-sand” weak-shadowing surface.

ratios also reflect the contribution of the shadowed roughness for vertical polarization.

#### 6.2.4 Dry Sand Surface ( $\epsilon_r = 3 - j0$ )

Figure 6.14 shows the backscattering from a weak-shadowing, low-loss dielectric surface with dielectric constant  $\epsilon_r = 3 - j0$ , and Figure 6.15 shows the same for the deep-shadowing configuration. The backscatter at  $30^{\circ}$  is reduced by approximately 18.7 dB at vertical and about 6.8 dB at horizontal polarization from the perfectly conducting case. Again, good agreement is shown between the two-scale model and the numerical backscatter down to approximately  $10^{\circ}$  (VV) and  $8.5^{\circ}$  (HH) for the weak-shadowing surface and  $17^{\circ}$  (VV) and  $15^{\circ}$  (HH) for the deep-shadowing surface. The two-scale model over-predicts the backscatter for small grazing angles of incidence.

In the weak-shadowing results, the smooth-in-shadow backscatter follows the rough-in-shadow scatter down to  $3^{\circ}$  grazing for vertical and  $2^{\circ}$  grazing for horizontal polarization. As with the previous surfaces, the vertical smooth-in-shadow backscatter falls

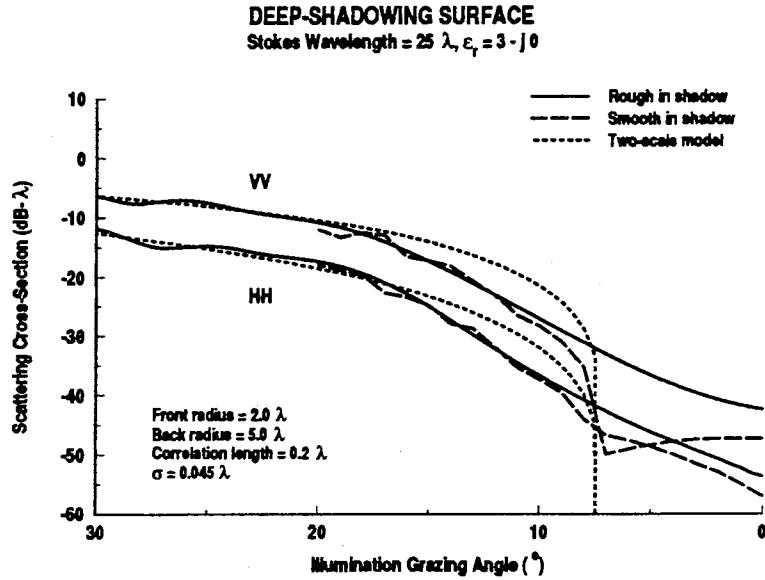


Figure 6.15: Backscattering for a “dry-sand” deep-shadowing surface.

severely from the rough-in-shadow scatter at lower grazing angles as the amount of roughness on the smooth-in-shadow surface decreases. The difference is about 16 dB at  $0^{\circ}$ . The horizontal smooth-in-shadow drops at  $2^{\circ}$ , and the difference between the rough-in-shadow and smooth-in-shadow scatter is about 19 dB at  $0^{\circ}$  grazing. Still, some contribution is seen from the weakly shadowed roughness at both polarizations.

The deep-shadowing results show a continued contribution by deeply shadowed roughness for vertical polarization. The smooth-in-shadow backscatter is within 2 dB of the rough-in-shadow backscatter down to  $10^{\circ}$  and  $9^{\circ}$  for vertical and horizontal polarizations, respectively. As with the “typical soil” deep-shadowing surface, the vertically polarized smooth-in-shadow backscatter drops at  $7^{\circ}$  where the back portion of the surface is entirely shadowed. Again, the smooth-in-shadow vertical backscatter rises at smaller grazing angles until it is only about 5 dB less than the rough-in-shadow backscatter at  $0^{\circ}$ . Numerical errors are thought to be the reason for the rise. The slight decrease in the horizontal smooth-in-shadow backscatter at small grazing angles

is probably too small to be significant, especially since the backscatter is already considerably reduced from the perfectly conducting case.

The backscattering ratios for the weak-shadowing surface are 24.9 dB for vertical and 30.0 dB for horizontal, while the deep-shadowing surface backscattering ratios are 36.2 dB and 41.8 dB for vertical and horizontal polarizations, respectively. These ratios support the conclusion that shadowing is more effective for this dielectric constant than for the perfectly conducting case. Weakly shadowed roughness contributes to the backscatter for both polarizations, and deeply shadowed roughness contributes to the vertically polarized backscatter.

### 6.3 Surface Current Magnitudes

To investigate the currents in the shadowed regions that might be induced by either diffraction or multiple scattering, the current magnitude along the deep-shadowing surface from the moment method solution is normalized to the current magnitude on the illuminated front face far from the diffraction point and plotted in Figure 6.16 for a perfectly conducting surface with an illumination angle of  $10^\circ$  grazing. At this angle, the front crest shadows much of the surface, but from between approximately  $x = -13.5$  and  $x = -5$  the rough surface features are directly illuminated. The locations of the shadows have been indicated on the figure.

It is clear that strong surface currents are induced onto the roughness for vertical polarization, even when the surface is deeply shadowed. The surface current for vertical polarization drops to an average of about 30% of the maximum just left of the front wave crest but rises to an average of about 50% just right of the illuminated roughness. The current for horizontal polarization is much weaker, falling to about 5% of the maximum to the left of the front crest and rising to less than 20% to the right of the illuminated roughness. The shadowed currents for this illumination angle

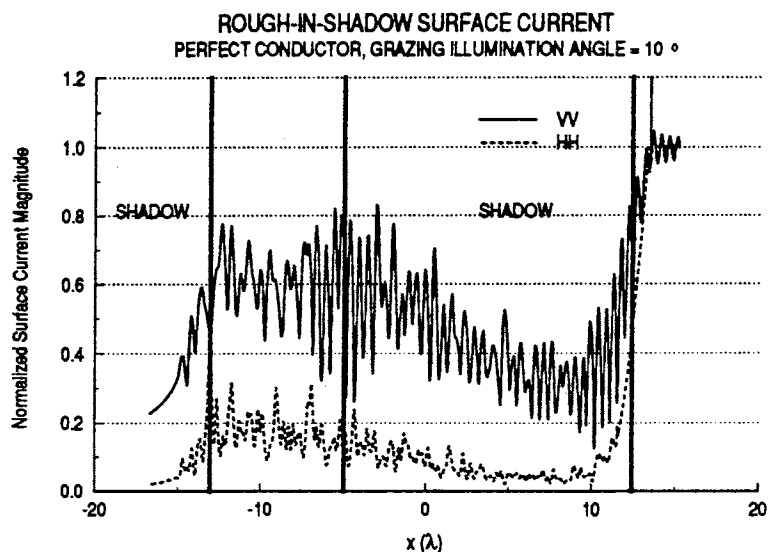


Figure 6.16: Current magnitudes for  $\theta_g = 10^\circ$ , perfect conductor, deep-shadowing surface.

may be explained by diffraction and multipath scatter into the shadowed region.

In the cases of impedance and dielectric surfaces, the moment method solution yields equivalent surface currents, not the true induced currents. However, these equivalent currents are responsible for the radiated fields and give insight into the scattering mechanisms involved. Figures 6.17, 6.18, and 6.19 show the normalized surface currents for an impedance surface  $\epsilon_r = 35 - j5$  and dielectric surfaces with  $\epsilon_r = 10 - j2$  and  $\epsilon_r = 3 - j0$  for a grazing illumination angle of  $10^\circ$ .

The relative shadow-region current magnitudes are reduced considerably from the perfectly conducting case. For the impedance surface  $\epsilon_r = 35 - j5$ , the normalized current magnitude for vertical polarization drops to approximately 12% of maximum in the shadow. The current for horizontal polarization drops even lower, to about 4% of maximum just left of the crest but rises to about 12% near the illuminated roughness. The currents are relatively small for the dielectric surfaces as well. For  $\epsilon_r = 10 - j2$ , the vertical current magnitude is observed to drop to about 12% and

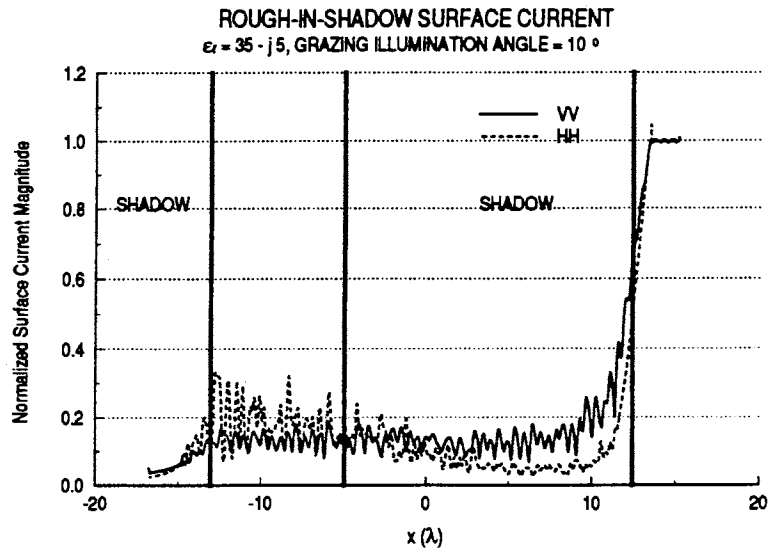


Figure 6.17: Current magnitudes for  $\theta_g = 10^\circ$ ,  $\epsilon_r = 35 - j5$ , deep-shadowing surface.

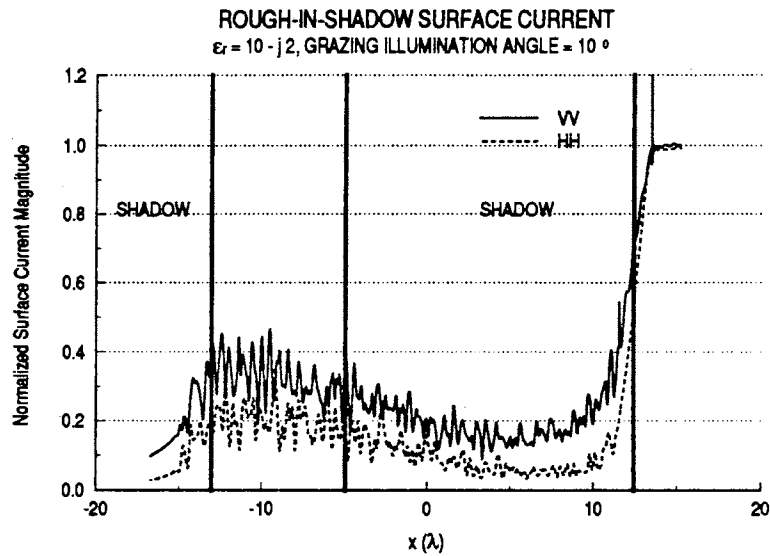


Figure 6.18: Current magnitudes for  $\theta_g = 10^\circ$ ,  $\epsilon_r = 10 - j2$ , deep-shadowing surface.

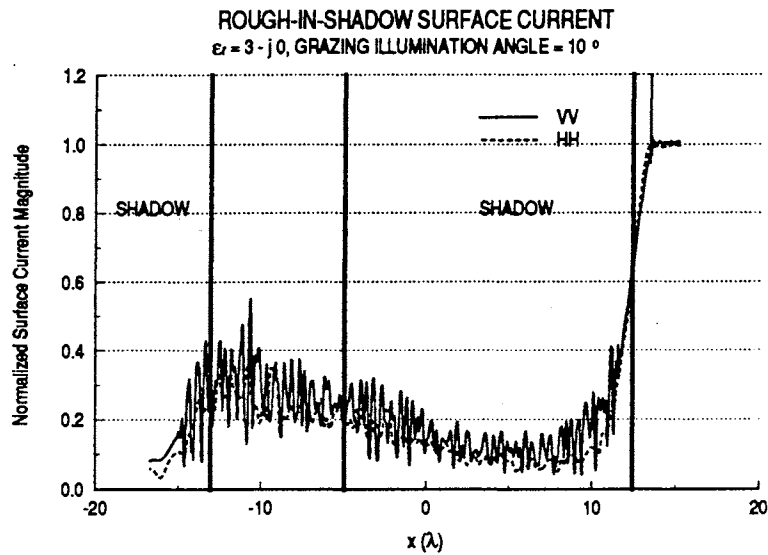


Figure 6.19: Current magnitudes for  $\theta_g = 10^\circ$ ,  $\epsilon_r = 3 - j0$ , deep-shadowing surface.

rise to about 20% of maximum near the illuminated roughness. For  $\epsilon_r = 3 - j0$  the magnitude of the current for both polarizations drops to about 6% left of the crest and rises to near 15% near the illuminated roughness. Note that for the dielectric surfaces, only the magnitude of the magnetic current ( $M$ ) is included in the plots, although the results appear quite similar when plotting  $J$ .

For a grazing illumination angle of  $0^\circ$ , all of the induced current in the shadowed region must be attributed to diffraction around the front wave crest, as the front crest entirely shadows the surface and none of the half Stokes wave trough is directly illuminated. In Figure 6.20, the shadow-region current magnitudes for a perfect conductor are reduced considerably from the  $10^\circ$  case but are still relatively strong for vertical polarization. The average current magnitudes for vertical and horizontal polarizations are 25% and 4% of the maximum, respectively. Figures 6.21, 6.22, and 6.23 show the normalized current magnitudes for  $0^\circ$  grazing illumination using  $\epsilon_r = 35 - j5$ ,  $\epsilon_r = 10 - j2$  and  $\epsilon_r = 3 - j0$ .

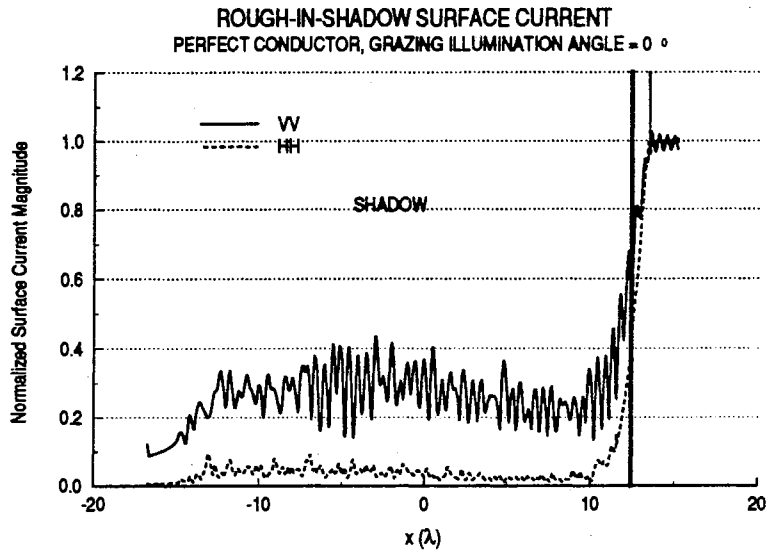


Figure 6.20: Current magnitudes for  $\theta_g = 0^\circ$ , perfect conductor, deep-shadowing surface.

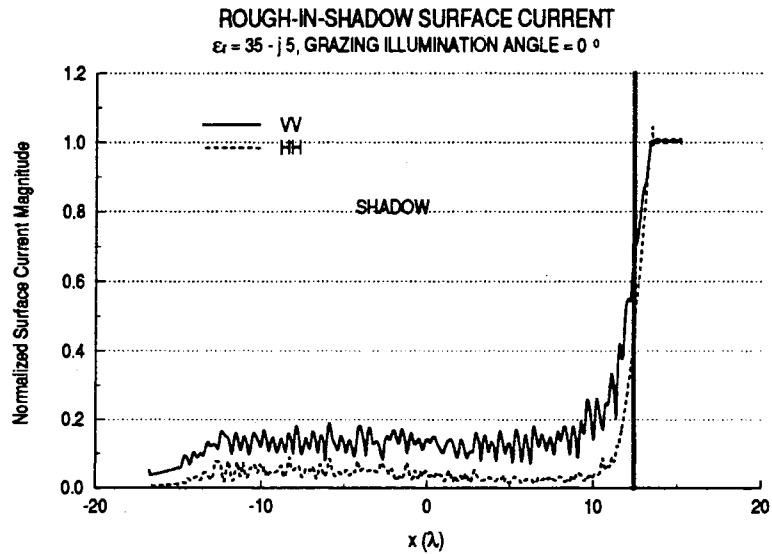


Figure 6.21: Current magnitudes for  $\theta_g = 0^\circ$ ,  $\epsilon_r = 35 - j5$ , deep-shadowing surface.

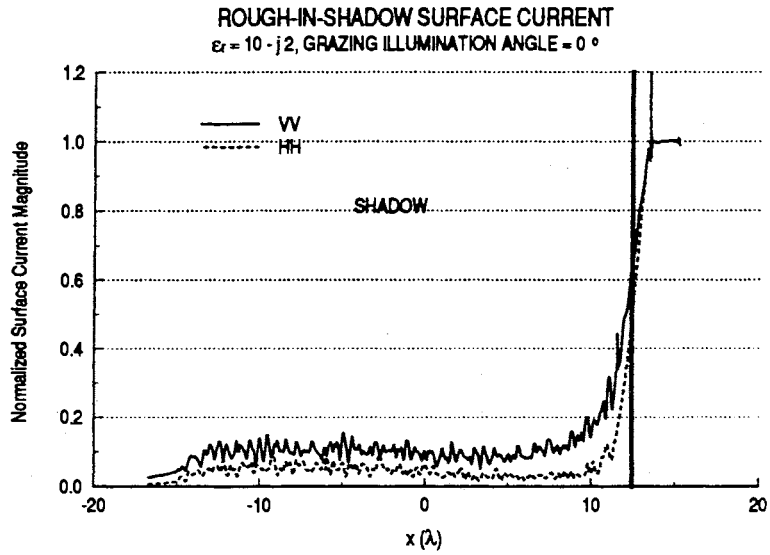


Figure 6.22: Current magnitudes for  $\theta_g = 0^\circ$ ,  $\epsilon_r = 10 - j2$ , deep-shadowing surface.

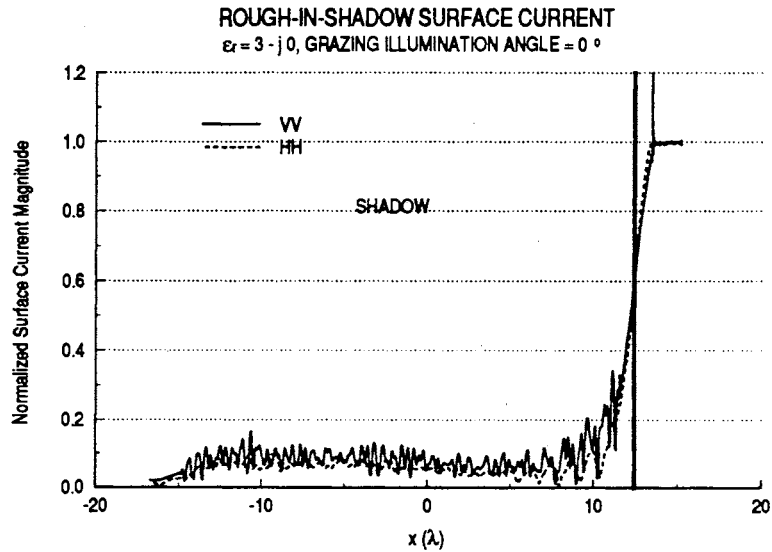


Figure 6.23: Current magnitudes for  $\theta_g = 0^\circ$ ,  $\epsilon_r = 3 - j0$ , deep-shadowing surface.



Weak shadow-region currents are observed on all three dielectric surfaces. The magnitude of the vertical polarization current drops to approximately 12%, 8%, and 5% of the maximum for surfaces with dielectric constants  $\epsilon_r = 35 - j5$ ,  $\epsilon_r = 10 - j2$ , and  $\epsilon_r = 3 - j0$ , respectively. The currents in the shadowed region for horizontal polarization are about 3% of the maximum for  $\epsilon_r = 35 - j5$  and  $\epsilon_r = 10 - j2$  but are slightly higher (approximately 6% of maximum) for  $\epsilon_r = 3 - j0$ . The increase in the current magnitude for horizontal polarization agrees with the slight difference between the observed rough-in-shadow and smooth-in-shadow results for  $\epsilon_r = 3 - j0$ , but again this current is not likely to be very significant as the backscatter is very low for this dielectric constant.

## 6.4 Discussion

Diffraction into the shadowed region and multiple scattering are thought to be the primary scattering mechanisms to explain the enhanced vertically polarized backscatter for perfect conductors. Barrick [8] used an exact modal formulation to study near-grazing scattering from perfectly conducting and finite conductivity sea surface models resembling near-braking Stokes waves. The investigation concluded that simple on/off shadowing descriptions are very inaccurate for vertical polarization. In a similar study, Holliday *et al.* used an analytical approximation to find the current in the shadowed region of a perfectly conducting scattering surface. This study also found that significant currents are induced on the shadowed portions of the surface for vertical polarization. The results in an investigation by West [10] support the Barrick and Holliday *et al.* findings.

In the case of imperfectly conducting surfaces like those investigated in this study, the effects of surface self-shadowing have not been extensively investigated. However, in the ideal case of diffraction by a dielectric wedge, a decreasing dielectric constant

is known to affect the strength of the diffracted field. Tiberio *et al.* [48] developed a form of the uniform geometrical theory of diffraction for a wedge with impedance faces based upon an exact solution given by Maliuzhinets [49]. In these studies, as the dielectric constant of the wedge faces decreases the strength of the field in the shadow region decreases for vertical polarization and increases for horizontal polarization. Hence, a decreasing dielectric constant for rough surface scattering problems is expected to increase the effectiveness of shadowing for vertical polarization and to decrease the effectiveness of shadowing for horizontal polarization.

From the plots of the backscattering and the current magnitudes for the various surfaces in this investigation, it can be concluded that weakly-shadowed roughness may contribute to both vertically and horizontally polarized backscatter. Deeply-shadowed roughness only appears to contribute to the vertically polarized backscatter. As expected, the strength of the shadowing is observed to increase for vertical polarization. The expected decrease in the strength of the shadowing for horizontal polarization is not observed, although a slight difference is noted between the rough-in-shadow and smooth-in-shadow backscatter for  $\epsilon_r = 3 - j0$ .

The shadowing-corrected two-scale model accurately predicts the backscatter from the test surfaces down to approximately  $20^\circ$ . For smaller grazing angles of incidence, only a portion of the roughness is directly illuminated, and the portion that is illuminated is not enough to establish a Bragg-resonance effect [30]. Therefore, two-scale model predictions are higher than the observed numerical backscatter (until the entire surface is in the shadow of the front crest). A two-scale model uncorrected for shadowing would be expected to over-predict the scattering even more severely. However, a recent experiment found the opposite to be true. In the Mountain Top Experiment, Mockapetris [50] compared the bistatic scattering from land surfaces near White Sands Missile Range to the scattering predicted by the two-scale model. The model assumed

the surface to be perfectly conducting and included a small-scale roughness superimposed upon the known large-scale characteristics of the land surface. Surprisingly, the experimental measurements of the horizontally polarized scattering agreed with the numerically predicted scatter rather well in spite of the fact that the two-scale model did not include a correction for shadowing.

Although the conclusions in this report do not support the Mockapetris findings, it should be noted that the scale of the surfaces used here are much smaller than actual land surfaces used in the Mockapetris study. A direct comparison between the studies, therefore, is not entirely meaningful. However, the effects of shadowing should be the same regardless of the scale of the surface. Even if it were possible to model extremely large surfaces using the hybrid MM/GTD technique, it would be very difficult to duplicate numerically the experimental results found in the Mockapetris study due to the various inhomogeneities in the surface dielectric constant and vegetation effects. Further investigation is warranted.

# Chapter 7

## SUMMARY AND CONCLUSIONS

The hybrid MM/GTD numerical technique has been extended to allow the calculation of scattering from lossy and low-loss dielectric media. This approach overcomes some of the shortcomings of the traditional MM technique by modeling large portions of the scattering surface using basis functions in the form of the GTD current on these sections. By modeling the entire surface in this way, truncation of the modeled surface is avoided, thus preventing the non-physical edge effects that are apparent in the far-field scatter of the current in the traditional MM solution. Tests of the new technique on canonical and practical scattering problems validate the derivation and implementation of the two-dimensional integral equations.

The hybrid technique was used to investigate the effects of small-scale roughness in the shadowed portions of dielectric surfaces that crudely represent geological features. A weak-shadowing surface model was generated using a near-breaking Stokes wave with rounded crests. When the illumination grazes the front crest of this surface at a very small angle, the front crest casts a shadow over the entire Stokes wave trough and back crest. The illumination shadow boundary is near the shadowed roughness on the back crest. Hence, scattering results from this model indicate the contributions of weakly shadowed roughness features on the back crest. A deep-shadowing surface model was generated by setting the large-scale displacement of the back Stokes wave crest to zero. For small grazing angles in this configuration, the illumination shadow

boundary is several wavelengths from the roughness on the back side of the surface. The contributions of the deeply-shadowed roughness features were investigated in this way.

The ensemble average backscattering cross-sections were found for 40 independent rough surface realizations for each of two roughness configurations. The rough-in-shadow configuration included a Gaussian roughness with a correlation length of  $L = 0.2\lambda$  and a height standard deviation of  $\sigma = 0.045\lambda$  along the entire Stokes wave trough. The smooth-in-shadow configuration included this roughness only on portions of the Stokes wave that are not shadowed from the incident field by the front wave crest. The dielectric constant of the scattering surface was chosen to represent a wide range of surface conditions ranging from perfectly conducting to moist clay ( $\epsilon_r = 35 - j5$ ), typical soil ( $\epsilon_r = 10 - j2$ ), and dry sand ( $\epsilon_r = 3 - j0$ ). The backscattering cross-sections were found for grazing angles of incidence ranging from  $30^\circ$  down to  $0^\circ$ .

The numerical results indicate that weakly shadowed roughness features significantly contribute to the horizontally and vertically polarized backscatter. This contribution is most pronounced for perfectly conducting surfaces, but the effect is also observed for each of the other three dielectric constants tested. Deeply shadowed roughness features contribute significantly to the backscatter for vertical polarization only, although a slight contribution to the horizontally polarized backscatter is observed at low grazing angles for the lossless dielectric surface,  $\epsilon_r = 3 - j0$ . An examination of the ratio of the rough-in-shadow backscattering cross-sections at  $30^\circ$  to the smooth-in-shadow backscattering cross-sections at  $0^\circ$  confirm the contributions by the roughness features in the shadow region. The backscatter from the shadowed roughness can be explained by currents induced into the shadow by diffraction from the front crest and by multiple scattering effects. The normalized surface current magnitudes were plotted along the deep-shadowing surface, and it was found that currents

with magnitudes between 10% and 40% of the maximum were found in the shadowed region for vertical polarization.

The results indicate that optically-derived shadowing descriptions are not sufficient to describe the illumination of rough two-scale surfaces at low grazing angles. The shadowing is best characterized by a combination of weak and deep shadowing conditions. Weakly shadowed roughness has been shown to contribute significantly to the backscatter for either polarization, while deeply shadowed roughness only contributes to the vertically polarized backscatter. The two-scale model predictions are accurate down to approximately  $20^\circ$  grazing, below which the two-scale model over-predicts the backscatter.

# BIBLIOGRAPHY

- [1] P. Beckmann and A. Spizzichino, *The Scattering of Electromagnetic Waves from Rough Surfaces*, Pergamon, New York, 1963.
- [2] Y. Jin, *Electromagnetic Scattering Modeling for Quantitative Remote Sensing*, World Scientific, Singapore, 1993.
- [3] S. O. Rice, "Reflection of electromagnetic wave from slightly rough surfaces", *Communications in Pure and Applied Mathematics*, vol. 4, no. 2, pp. 351–378, Aug. 1951.
- [4] G. R. Valenzuela, "Scattering of electromagnetic waves from a tilted, slightly rough surface", *Radio Science*, vol. 3, no. 11, pp. 1057–1066, Nov. 1968.
- [5] J. W. Wright, "A new model for sea clutter", *IEEE Transactions on Antennas and Propagation*, vol. AP-16, no. 2, pp. 217–223, Mar. 1968.
- [6] D. A. McNamara, C. W. I. Pistorius, and J. A. G. Malherbe, *Introduction to the Uniform Geometrical Theory of Diffraction*, Artech House, Boston, 1990.
- [7] C. A. Balanis, *Advanced Engineering Electromagnetics*, Wiley, New York, 1989.
- [8] D. E. Barrick, "Near-grazing illumination and shadowing of rough surfaces", *Radio Science*, vol. 30, no. 3, pp. 563–580, May 1995.
- [9] D. Holliday, L. L. DeRaad, and G. J. St. Cyr, "Volterra approximation for low grazing angle shadowing on smooth ocean-like surfaces", *IEEE Transactions on Antennas and Propagation*, vol. 43, no. 9, pp. 1199–1206, Sept. 1995.
- [10] J. C. West, "Effect of shadowing on electromagnetic scattering from rough ocean-wave-like surface at small grazing angles", *IEEE Transactions on Geoscience and Remote Sensing*, 1996, In press.
- [11] R. Harrington, *Field Computation by Method of Moments*, Macmillan, New York, 1968.
- [12] W. D. Burnside, C. L. Yu, and R. J. Marhefka, "A technique to combine the geometrical theory of diffraction and the moment method", *IEEE Transactions on Antennas and Propagation*, vol. AP-23, no. 4, pp. 551–558, July 1975.

- [13] C. A. Balanis, *Antenna Theory: Analysis and Design*, Wiley, New York, 1982.
- [14] R. Chen, *Numerical Investigation of Electromagnetic Scattering from the Ocean Surface at Extreme Grazing Angles*, PhD thesis, Oklahoma State University, School of Electrical and Computer Engineering, Stillwater, Oklahoma 74078, 1993.
- [15] F. T. Ulaby, R. K. Moore, and A. K. Fung, *Microwave Remote Sensing: Active and Passive*, vol. 2, Artech House, Norwood, Massachusetts, 1986.
- [16] J. S. Bendat and A. G. Piersol, *Random Data: Analysis and Measurement Procedures*, Wiley-Interscience, New York, 1986.
- [17] Y. Kim, E. Rodriguez, and S. Durden, "A numerical assessment of rough surface scattering theories: Vertical polarization", *Radio Science*, vol. 27, no. 4, pp. 515-527, July 1992.
- [18] Jr. W. J. Pierson and L. Moskowitz, "A proposed spectral form for fully developed wind seas based on the similarity theory of S. A. Kitaigorodskii", *Journal of Geophysical Research*, vol. 69, no. 24, pp. 5181-5190, 1964.
- [19] E. I. Thorsos, "Acoustic scattering from a 'Pierson-Moskowitz' sea surface", *Journal of the Acoustical Society of America*, vol. 88, no. 1, pp. 335-349, July 1990.
- [20] E. Rodriguez, Y. Kim, and S. Durden, "A numerical assessment of rough surface scattering theories: Horizontal polarization", *Radio Science*, vol. 27, no. 4, pp. 497-513, July 1992.
- [21] A. K. Fung and M. F. Chen, "Numerical simulation of scattering from simple and composite random surfaces", *Journal of the Optical Society of America, Series A*, vol. 2, no. 12, pp. 2274-2284, Dec. 1985.
- [22] P. Beckmann, "Shadowing of random rough surfaces", *IEEE Transactions on Antennas and Propagation*, vol. AP-13, no. 3, pp. 384-388, May 1965.
- [23] R. A. Brockelman and T. Hagfors, "Note on the effect of shadowing on the backscattering of waves from a random rough surface", *IEEE Transactions on Antennas and Propagation*, vol. AP-14, no. 5, pp. 621-629, Sept. 1966.
- [24] R. J. Wagner, "Shadowing of randomly rough surfaces", *Journal of the Acoustical Society of America*, vol. 41, no. 1, pp. 138-147, Jan. 1967.
- [25] M. L. Sancer, "Shadow-corrected electromagnetic scattering from a randomly rough surface", *IEEE Transactions on Antennas and Propagation*, vol. AP-17, no. 5, pp. 577-585, Sept. 1969.
- [26] E. I. Thorsos, "The validity of the Kirchhoff approximation for rough surface scattering using a Gaussian roughness spectrum", *Journal of the Acoustical Society of America*, vol. 83, no. 1, pp. 78-82, Jan. 1988.



- [27] R. M. Axline and A. K. Fung, "Numerical computation of scattering from a perfectly conducting slightly rough surface", *IEEE Transactions on Antennas and Propagation*, vol. AP-26, no. 3, pp. 482-488, May 1978.
- [28] E. I. Thorsos and D. R. Jackson, "The validity of the perturbation approximation for rough surface scattering using a Gaussian roughness spectrum", *Journal of the Acoustical Society of America*, vol. 86, no. 1, pp. 261-277, July 1989.
- [29] G. S. Brown, "Some asymptotic considerations in low grazing angle scattering from rough surfaces", in *Proceedings of the 1994 URSI Radio Science Meeting*, University of Washington, Seattle, Washington, June 19-24 1994, p. 153.
- [30] J. C. West, R. K. Moore, and J. C. Holtzman, "The slightly-rough facet model in radar imaging of the ocean surface", *International Journal of Remote Sensing*, vol. 11, no. 4, pp. 617-637, Apr. 1990.
- [31] J. M. Sturm, "Iterative methods for solving large linear systems in the moment method analysis of electromagnetic scattering", Master's thesis, Oklahoma State University, School of Electrical and Computer Engineering, Stillwater, Oklahoma 74078, 1993.
- [32] R. Mittra, Ed., *Integral Equation Solutions of Three-dimensional Scattering Problems*, Pergamon Press, New York, 1973.
- [33] T. B. A. Senior and J. L. Volakis, "Generalized impedance boundary conditions in scattering", *Proceedings of the IEEE*, vol. 79, no. 10, pp. 1413-1420, Oct. 1991.
- [34] A. W. Glisson, "Electromagnetic scattering by arbitrarily shaped surfaces with impedance boundary conditions", *Radio Science*, vol. 27, no. 6, pp. 935-943, Nov. 1992.
- [35] W. V. T. Rusch and R. P. Pogorzelski, "A mixed-field solution for scattering from composite bodies", *IEEE Transactions on Antennas and Propagation*, vol. AP-34, no. 7, July 1986.
- [36] E. Arvas, S. M. Rao, and T. K. Sarkar, "E-field solution of TM-scattering from multiple perfectly conducting and lossy dielectric cylinders of arbitrary cross-section", *IEE Proceedings*, vol. 133, Pt. H, no. 2, pp. 115-121, Apr. 1986.
- [37] G. T. Ruck, *Radar Cross Section Handbook*, Plenum Press, New York, 1970.
- [38] J. C. West and J. M. Sturm, "A hybrid MM/GTD numerical technique for lossy dielectric rough surface scattering calculations", Final Report for AFOSR Summer Faculty and Graduate Student Research Programs, Rome Laboratory, Hanscom AFB, 1995.

- [39] R. Tiberio, G. Pelosi, G. Manara, and P. H. Pathak, "High-frequency scattering from a wedge with impedance faces illuminated by a line source, Part I: Diffraction", *IEEE Transactions on Antennas and Propagation*, vol. 37, no. 2, Feb. 1989.
- [40] D. E. Stewart and Z. Leyk, "Meschach: Matrix computations in C", in *Proceedings of the Centre for Mathematics and its Applications*, The Australian National University, 1994, vol. 32.
- [41] D. E. Amos, "Algorithm 644: A portable package for Bessel functions of a complex argument and nonnegative order", *ACM Transactions on Mathematical Software*, vol. 12, no. 3, pp. 265–273, Sept. 1986.
- [42] H. T. Thacher, Jr., "Algorithm 215: SHANKS", *Communications of the ACM*, vol. 6, no. 11, pp. 662, Nov. 1963.
- [43] C. Brezinski and M. Redivo Zaglia, *Extrapolation Methods: Theory and Practice*, Elsevier Science Publishing Company, New York, 1991.
- [44] B. O'Leary, "A comparison of scattering results obtained with the periodic surface moment method and several approximate scattering theories using wave tank data", Master's thesis, Oklahoma State University, School of Electrical and Computer Engineering, Stillwater, Oklahoma 74078, 1996.
- [45] C. A. Siller, Jr., "Evaluation of the radiation integral in terms of end-point contributions", *IEEE Transactions on Antennas and Propagation*, vol. AP-23, no. 9, Sept. 1975.
- [46] A. J. Booyesen and C. W. I. Pistorius, "Electromagnetic scattering by a two-dimensional wedge composed of conductor and lossless dielectric", *IEEE Transactions on Antennas and Propagation*, vol. AP-40, no. 4, pp. 383–390, Apr. 1992.
- [47] M. S. Longuet-Higgins, "On the form of the highest progressive and standing waves in deep water", *Proceedings of the Royal Society of London, Series A*, vol. 331, no. 1587, pp. 445–456, 1973.
- [48] R. Tiberio, G. Pelosi, and G. Manara, "A uniform GTD formulation for the diffraction by a wedge with impedance faces", *IEEE Transactions on Antennas and Propagation*, vol. 33, no. 8, Aug. 1985.
- [49] G. D. Maliuzhinets, "Excitation, reflection, and emission of surface waves from a wedge with given face impedances", *Sov. Phys. Dokl.*, vol. 3, pp. 752–755, 1979.
- [50] L. M. Mockapetris, "Effect of surface and scattering parameters on two scales of roughness models", in *Proceedings of the Progress in Electromagnetic Research Symposium*, July 24–28, Seattle, Washington, 1995, p. 224.

2  
VITA

James Michael Sturm

Candidate for the Degree of

Doctor of Philosophy

Thesis: NUMERICAL INVESTIGATION OF RADAR SCATTERING FROM  
ROUGH LAND SURFACES

Major Field: Electrical Engineering

Biographical:

Personal Data: Born in Austin, Texas, on February 15, 1969, the son of  
Gene P. Sturm, Jr. and Phyllis Ann Sturm.

Education: Received Bachelor of Science and Master of Science degrees in Elec-  
trical Engineering from Oklahoma State University, Stillwater, Oklahoma  
in December 1991 and December 1993, respectively. Completed the re-  
quirements for the Doctor of Philosophy degree in Electrical Engineering  
at Oklahoma State University in December 1996.

Professional Experience: Undergraduate research fellow at the National Insti-  
tute for Petroleum and Energy Research during the summers of 1988,  
1989, and 1991. Research Assistant at Oklahoma State University De-  
partment of Electrical and Computer Engineering from January 1992 to  
December 1994 and January 1996 to present. Teaching Assistant at Ok-  
lahoma State University Department of Electrical and Computer Engin-  
eering from January 1995 to December 1995. Air Force Office of Scientific  
Research Graduate Research Fellow at Rome Laboratory from May 1995  
to July 1995.

Professional Memberships: Eta Kappa Nu, Tau Beta Pi, Institute for Electrical  
and Electronics Engineers.